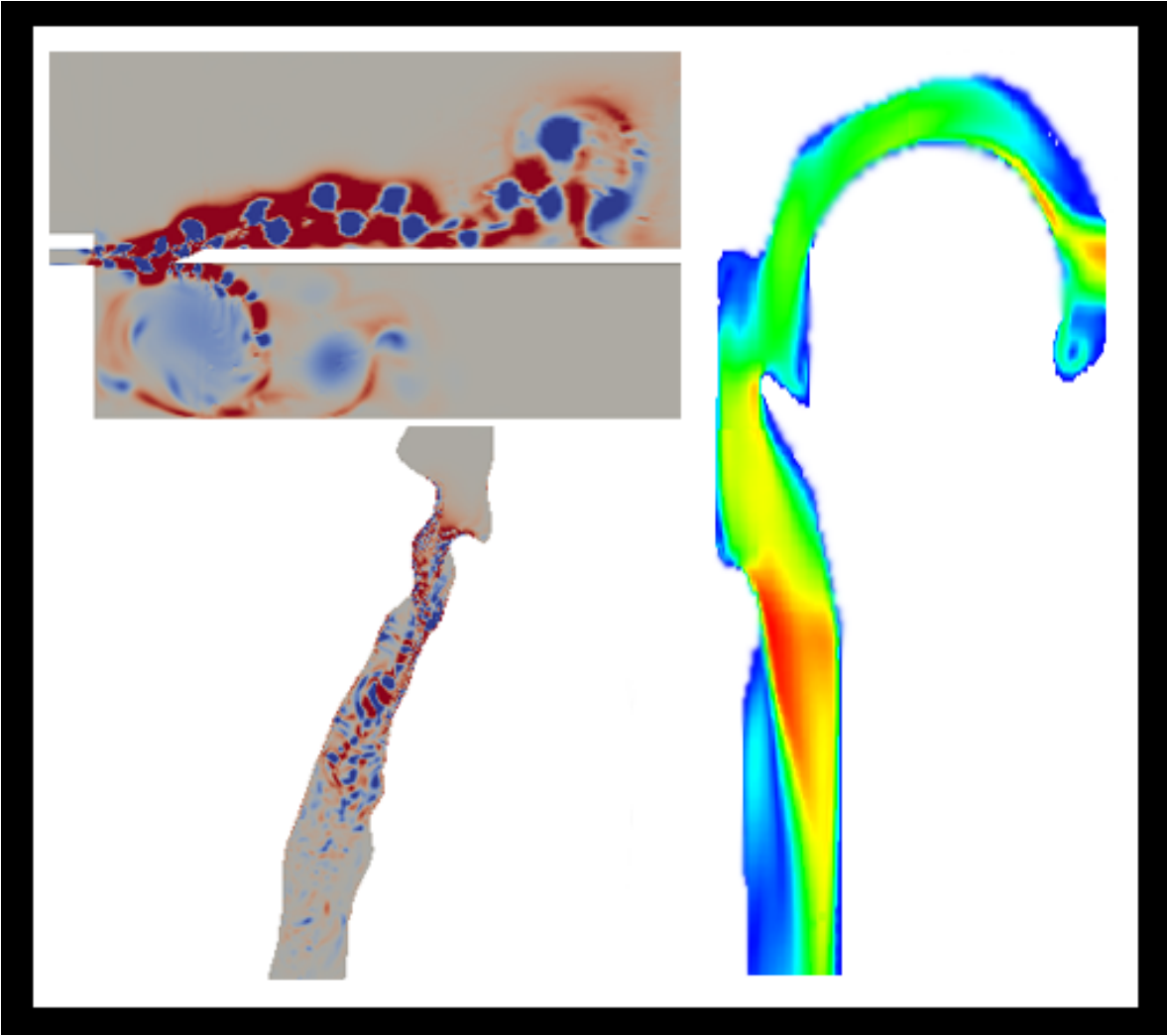


---

The numerical acoustic and fluid flow analysis on a CT-scan derived upper airway model of a stridor patient

---

C.T. Lynch





Title: The numerical acoustic and fluid flow analysis on a CT-scan derived upper airway model of a stridor patient

Date: March 8, 2012

Author: Christopher T. Lynch

Supervisors: Hester Bijl, Hans Hoeve and Sander van Zuijlen

Version: 3.0

#### Abstract:

In this report the acoustic numerical analysis of a stridor patient is discussed. Stridor is an abnormal, noisy or toned/voiced breathing sound which is caused by obstruction or malformation of pharynx, larynx, trachea or the bronchia; whereby the turbulence of air and vibration of surrounding tissue are the source of the observed sound. There is a need for uninvase diagnostics because of risks involved using anaesthetics, especially on young children. To find the obstruction from a sound signal, first one needs to know what kind of sound is produced by what kind of geometry. Doing this numerically has the advantage of allowing one to change only one parameter at the time. Using a hybrid approach, combining LES and the Lighthill equation, the airflow acoustics for internal flows can be predicted. The acoustics are validated on a reed instrument and diaphragm. The sound pressure level is of the right magnitude and also good agreement is found for the distribution of power. The lower frequencies are however over predicted. The fluid part is validated using PIV measurements on a simplified upper airway model. Good agreement was found. The fluid and acoustic analysis on the different upper airway models showed that probably for increasing constriction the sound production mechanism shifts from turbulent sound production to tissue vibration. Therefore a rigid wall approach is not good enough to predict the sounds generated by obstructions in stridor patients.

# Acknowledgements

One year and a couple of days ago I started my research on the numerical analysis on a stridor patient. In a short time I figured out that the CFD analysis on human airways was just starting to develop and the research I was getting myself into was something special not many have tried before. Being one of the first to try something is always a bit hard, since you do not have many shoulders to lean on. Luckily I found many related topics that could be combined into something new: the numerical acoustic analysis on a CT-scan derived obstructed human airway.

When all information was gathered I started to work, and tried to implement everything into OpenFOAM. During this period I often forgot to sleep desperately trying to get my solver to work. Making incremental steps I was finally able to calculate sound produced by airflows! This was an euphoric moment. However, it did not last.. What followed was a long struggle to get a complete model to work. Even the smallest mistakes in the mesh or boundary conditions gave wrong results. After fine tuning the solver, the boundary conditions, the meshing procedure, the model layout and the post processing matlab routines I was finally able to come close to experimental en numerical reference data. Happily showing the results to others, a date for the first part of my thesis was set. This was around the Christmas holiday. It was also the time where I found one last mistake in the model set-up.. Frantically fixing up all models in hight speed, while still trying to enjoy new years eve celebrations, I soon took over a large part of the TU's computational cluster to still get my results in time. This period I have probably worked harder than ever before, which means something as an honours track student.. Luckily the results could be analysed on time. And although they were different than expected -¿ stridor patients show similar sound pressure levels near the inlet compared with a healthy person?? what?!? ¿- I was luckily still able to find a logical physical interpretation yielding a solid conclusion.

In the end the most difficult part, mostly from a mental point of view, was to get all information from my head into a good looking and well structured report. I largely underestimated the amount of time that was necessary to get everything right. Luckily the large amount of feedback that I received from my supervisors guided me towards a properly written thesis report.

I would like to take this opportunity to acknowledge all people that have contributed to the successful completion of this master thesis. My thanks goes out to especially my supervisors Alexander van Zuijlen and Hester Bijl for supporting me and guiding me in the right direction, for being critical, and having a high expectation. Also I want to thank Hans Hoeve for helping me make sense of the medical parts of the research, for providing patient data and for giving me the opportunity to see the diagnostic procedure up close. Further I would like show my appreciation for the work performed by Wim Vos, who has created the 3D model from a CT-scan, that I used for the analysis of a stridor patient. Also I would like

to thank Chris Lacour for providing the simplified upper airway model.

Tiuri Abu-Kias, Sebastiaan Lemmens and Liora Monas thank you for the awesome 5 years of studying!!! Thank you for helping me to get the most out of my days at the TU Delft. Lukas Kuijken, thank you for being my best friend and for drinking nice cold beers with me. Sarai Buitelaar, thank you for always being there for me. And last but not least I like to thank all my other friends and family(!) who kept me happy during hard days of work.

*Christopher Terence Lynch, March 2012*

# Contents

List of abbreviations	v
List of symbols	vii
Summary	xiii
<b>1 Properties of the respiratory track and stridor</b>	<b>5</b>
1.1 Respiratory System . . . . .	5
1.1.1 Nasal cavity . . . . .	5
1.1.2 Oral cavity . . . . .	5
1.1.3 Pharynx . . . . .	7
1.1.4 Larynx . . . . .	7
1.1.5 Lower respiratory tract . . . . .	7
1.1.6 Geometric parameters . . . . .	9
1.2 Typical airflow . . . . .	9
1.3 Stridor . . . . .	12
1.3.1 Causes of stridor . . . . .	12
1.3.2 Studies on stridor sounds . . . . .	13
1.4 Acoustic and mechanical properties . . . . .	16
<b>2 The computational model</b>	<b>19</b>
2.1 Aerodynamic formulation . . . . .	19
2.2 Acoustic modeling . . . . .	20
2.3 Boundary conditions . . . . .	21
2.3.1 Inlets and outlets . . . . .	22
2.3.2 Walls . . . . .	22
<b>3 Acoustic validation</b>	<b>25</b>
3.1 Reed instrument . . . . .	25
3.1.1 Boundary conditions . . . . .	26
3.1.2 CFD results . . . . .	26
3.1.3 Acoustic analysis . . . . .	27
3.2 Diaphragm . . . . .	29
3.2.1 The geometry . . . . .	31
3.2.2 Boundary conditions . . . . .	31
3.2.3 CFD results . . . . .	32
3.2.4 Acoustic results . . . . .	35

---

3.3	Conclusion . . . . .	38
<b>4</b>	<b>Analysis of a simplified upper airway model</b>	<b>41</b>
4.1	The geometry . . . . .	41
4.2	The boundary conditions . . . . .	42
4.3	Comparing LES models . . . . .	44
4.4	Fluid flow validation . . . . .	44
4.5	Acoustic analysis . . . . .	50
<b>5</b>	<b>Analysis of a realistic CT-scan derived airway model</b>	<b>59</b>
5.1	The geometry . . . . .	59
5.2	Boundary conditions . . . . .	60
5.3	Fluid flow analysis . . . . .	62
5.4	Acoustic analysis . . . . .	70
<b>6</b>	<b>Conclusions</b>	<b>75</b>
<b>7</b>	<b>Future development and recommendations</b>	<b>77</b>
7.1	Further analysis using developed model . . . . .	77
7.2	Patient data . . . . .	77
7.3	Model improvements . . . . .	78
<b>A</b>	<b>Model geometries</b>	<b>85</b>
A.1	Reed . . . . .	85
A.2	Diaphragm . . . . .	86
A.3	SUAM . . . . .	87
A.4	RUAM . . . . .	88

# List of abbreviations

CFD	Computation fluid dynamics
CT	Computed tomography
DES	Detached eddy simulation
LES	Large eddy simulation
PIV	Particle image velocimetry
RANS	Reynold-averaged Navier-Stokes
RUAM	Realistic upper airway model
SGS	Subgrid scale
SUAM	Simplified upper airway model
URANS	Unsteady RANS



# List of symbols

---

<b>Greek Symbols</b>	
$\delta_i$	incoming wave front angle
$\delta_t$	transmissive wave front angle
$\rho$	Density
$\rho'$	Density perturbation
$\theta$	Parameter used to determine three dimensionality
$\theta_0$	Threshold value of $\theta$
$\mu$	Dynamic viscosity
$\nu$	Edge tone frequency $\sigma$ Damping coefficient
$\omega$	Fundamental resonator frequency

---

<b>Roman Symbols</b>	
$A$	Incoming wave amplitude
$B$	Transmissive wave amplitude
$c$	Speed of sound
$C$	Reflective wave amplitude
$j$	Number that gives fundamental frequencies and overtones
$h$	Height
$l$	Length scale
$L$	Length scale
$M$	Mach number
$p$	Pressure
$p'$	Pressure perturbation
$Q$	Parameter on which damping is applied
$S_{ij}$	Strain rate
$t$	Time
$T_{ij}$	Lighthill stress tensor
$u$	Velocity
$V$	Velocity
$x$	Spatial coordinate
$y^+$	Wall unit
$Z$	impedance



# List of Figures

1.1	General overview respiratory system . . . . .	6
1.2	Nasal cavity layout . . . . .	6
1.3	Oral cavity layout . . . . .	7
1.4	Larynx layout . . . . .	8
1.5	Lower respiratory tract (left),Alveoli and bronchiole (right) . . . . .	8
1.6	Comparison of nasal cross-sectional area, perimeter and hydraulic diameter between a 5-year-old boy and an adult male as a function of the distance from the nose tip. The nasal valve is marked with a solid arrow for the child and a hollow arrow for the adult. The vertical dashed line denotes the start of the nasopharynx (NP).(a) The cross-sectional area (A) and (b) perimeter (P) are the summation of right and left passages.(c) The hydraulic diameter is calculated from the relation $d_h = 4A/P$ . [21] . . . . .	10
1.7	Velocity fields in the nasal passages at an inhalation flow rate of $0.33L/s$ in (a) 3-D, (b) sagittal, and (c) cross-sectional (coronal) views. The filled arrow marks the location of flow separation and recirculation in the nasopharynx. [41]	11
1.8	Turbulent kinetic energy, reference [41] . . . . .	12
1.9	Laryngomalacia, arytenoid tissue collapses . . . . .	13
1.10	Laryngitis (left), resolved laryngitis (right) . . . . .	14
1.11	Subglottic stenosis . . . . .	14
1.12	Spectrogram laryngomalacia [44] . . . . .	15
3.1	Reed model, dimensions [30] . . . . .	25
3.2	Reed velocity field [m/s], reference [30] (left) and thesis research (right) . . . . .	27
3.3	Reed vorticity field [ $s^{-1}$ ], reference [30] (left) and thesis research (right) . . . . .	27
3.4	Reed source term field [ $kg/m^3/s^2$ ], reference [30] (left) and thesis research (right) . . . . .	28
3.5	Reed density field [ $kg/m^3$ ], reference [30] (left) and thesis research (right) . . . . .	28
3.6	Reed, density field [ $kg/m^3$ ]. Overall look of the density field with the axis scaled properly . . . . .	28
3.7	Reed, acoustic point data: left raw density output, right detrended converted output . . . . .	30
3.8	Reed, sound pressure [30] . . . . .	30
3.9	Diaphragm 3D Model, dimensions [15] . . . . .	31
3.10	Diaphragm 3D Model $V = 6m/s$ , Velocity field: Top fine, middle coarse, bottom from [15] . . . . .	32
3.11	Diaphragm 3D Model $V = 6m/s$ , Vorticity (magnitude) field: Top fine, middle coarse, bottom from [15] . . . . .	33

3.12	Diaphragm 3D Model $V = 6m/s$ , Source term field: Top fine, bottom coarse .	33
3.13	Diaphragm 3D Model $V = 14m/s$ , Top velocity field, middle vorticity (magnitude) field, bottom source term field . . . . .	34
3.14	Diaphragm 2D Model $V = 6m/s$ , velocity field . . . . .	34
3.15	Diaphragm coarse 3D Model $V = 6m/s$ , left raw density signal and right resulting pressure pertubations . . . . .	35
3.16	Diaphragm coarse 3D Model $V = 6m/s$ , left overall sound pressure and right zoomed sound pressure . . . . .	36
3.17	Diaphragm coarse 3D Model $V = 14m/s$ , left raw density signal and right resulting pressure perturbations . . . . .	37
3.18	Diaphragm coarse 3D Model $V = 14m/s$ , left overall sound intensity distribution and right zoomed sound intensity . . . . .	37
3.19	Diaphragm coarse 3D Model $V = 6m/s$ and $V = 14m/s$ , left unaltered sound pressure distribution and right shifted sound pressure distribution . . . . .	37
3.20	Diaphragm 2D Model $V = 6m/s$ , Sound pressure: set a: impedance boundary condition, set b: zero gradient boundary condition . . . . .	38
4.1	SUAM dimensions[20] . . . . .	43
4.2	Lineplots $(U_x^2 + U_z^2)^{0.5}/U_{in}[-]$ , Letters indicate cross sections in figure 4.1, — <i>One Equation model</i> , — <i>Smagorinsky</i> and — <i>Selective Smagorinsky</i> . Reference[20] .	45
4.3	Simplified upper airway model, streamlines: side view upper part(left), side view bottom part(middle) and top view(right) . . . . .	45
4.4	Simplified upper airway model, streamlines: original(left), 50% constriction (middle) and 75% constriction(right) . . . . .	46
4.5	Simplified upper airway model, $U_z[m/s]$ : original(left), 50% constriction (middle) and 75% constriction(right) . . . . .	47
4.6	Simplified upper airway model, $ U [m/s]$ : original(left), 50% constriction (middle) and 75% constriction(right) . . . . .	48
4.7	Simplified upper airway model, vorticity $[s^{-1}]$ : original(left), 50% constriction (middle) and 75% constriction(right) . . . . .	49
4.8	Simplified upper airway model, source term $[kg/m^3/s^2]$ : original(left), 50% constriction (middle) and 75% constriction(right) . . . . .	49
4.9	Simplified upper airway model, pressure $[Nm/kg]$ : original(left), 50% constriction (middle) and 75% constriction(right) . . . . .	50
4.10	Comparison of different meshes with experimental data, $(U_x^2 + U_z^2)^{0.5}/U_{in}[-]$ , Letters indicate cross sections in figure 4.1, — <i>Coarse model</i> ( $8.89 \cdot 10^5$ cells), — <i>Fine model</i> ( $2.52 \cdot 10^6$ cells) and — <i>Super fine model</i> ( $4.59 \cdot 10^6$ cells). Reference[20]	51
4.11	Simplified upper airway model, left $U_z[m/s]$ and right $ U [m/s]$ . . . . .	52
4.12	Simplified upper airway model, left vorticity $[s^{-1}]$ and right source term $kg/m^3/s^2$	52
4.13	Averaged Fourier spectrum on experimentally obtained stridor sound[44], left: 15-month-old boy with subglottic stenosis, right: 1-week-old boy with a little subglottic stenosis and much supraglottic mucus . . . . .	53
4.14	Averaged Fourier spectrum on experimentally obtained stridor sound[44], left: 16-month-old girl with subglottic stenosis, right: 11-month-old boy with a glottic and subglottic stenosis . . . . .	54

4.15	Simplified upper airway model, pressure[Pa] over time: Left original model and right 50% constricted model. Probenumber 1 is placed near the inlet and probenumber 12 near the outlet. . . . .	54
4.16	Simplified upper airway model, pressure[Pa] over time: 75% constricted model. Probenumber 1 is placed near the inlet and probenumber 12 near the outlet . . . . .	55
4.17	Simplified upper airway model, pressure[Pa] over time: Left all models inlet probe right all models for outlet probe . . . . .	55
4.18	Simplified upper airway model, sound pressure inlet [dB]: Left overall view right zoomed view . . . . .	56
4.19	Simplified upper airway model, sound pressure outlet [dB]: Left overall view right zoomed view . . . . .	57
4.20	Simplified upper airway model, pressure[Pa] over time: Left 75% constricted model Right zoomed plot . . . . .	57
5.1	RUAM layout. Original (left) and adapted(right) . . . . .	61
5.2	Realistic upper airway model, streamlines: left - stridor patient and right - healthy person The figure shows part of the RUAM starting at the top on the left side and finishing on the right side of the figure at the bottom of the RUAM . . . . .	62
5.3	Realistic upper airway model, velocity magnitude[m/s]: left - stridor patient and right - healthy person . . . . .	63
5.4	Realistic upper airway model, velocity z-direction[m/s]: left - stridor patient and right - healthy person . . . . .	64
5.5	Realistic upper airway model, selection function[-]: left - stridor patient and right - healthy person . . . . .	65
5.6	Realistic upper airway model, vorticity magnitude field[s <sup>-1</sup> ]: left - stridor patient and right - healthy person . . . . .	66
5.7	Realistic upper airway model, source term[kg/m <sup>3</sup> /s <sup>2</sup> ]: left - stridor patient and right - healthy person . . . . .	67
5.8	Realistic upper airway model, pressure[Nm/kg]: left - stridor patient and right - healthy person . . . . .	68
5.9	Realistic upper airway models, velocity magnitude[m/s] from left right: stridor patient(coarse), healthy person(coarse), stridor patient(fine) and healthy person(fine) . . . . .	69
5.10	Realistic upper airway models, vorticity magnitude[s <sup>-1</sup> ] from left right: stridor patient(coarse), healthy person(coarse), stridor patient(fine) and healthy person(fine) . . . . .	70
5.11	Realistic upper airway models, source term[kg/m <sup>3</sup> /s <sup>2</sup> ] from left right: stridor patient(coarse), healthy person(coarse), stridor patient(fine) and healthy person(fine) . . . . .	71
5.12	Realistic upper airway model, pressure[Pa]: left stridor patient and right healthy patient . . . . .	72
5.13	Realistic upper airway model, pressure[Pa]: left inlet and right outlet . . . . .	72
5.14	Realistic upper airway model,inlet sound pressure[dB]: left overall spectrum and right zoomed spectrum . . . . .	73
5.15	Realistic upper airway model,outlet sound pressure[dB]: left overall spectrum and right zoomed spectrum . . . . .	74
5.16	Frequency spectrum from experimental stridor sample from reference [44] . . . . .	74

---

A.1	Reed mesh, zoomed (left) and global (right) . . . . .	85
A.2	Diaphragm computational model . . . . .	86
A.3	Mesh diaphragm, course(left) and fine (right) . . . . .	86
A.4	SUAM constrictions, from left to right: 0%, 50% and 75% of tracheal area . .	87
A.5	Mesh SUAM, course(left) fine(middle) and extra-fine(right) . . . . .	87
A.6	Mesh RUAM, original(left)and edited(right) . . . . .	88
A.7	RUAM original, zoom on stenosis . . . . .	89
A.8	RUAM edited, zoom on resolved stenosis . . . . .	89
A.9	Mesh RUAM, coarse(left) and fine(right) . . . . .	89
A.10	Cutplane used for front view, original(left) and edited(right) . . . . .	90

# Summary

In this report the acoustic numerical analysis of a stridor patient is discussed. Stridor is an abnormal, noisy or toned/voiced breathing sound which is caused by obstruction or malformation of pharynx, larynx, trachea or the bronchia; whereby the turbulence of air and vibration of surrounding tissue are the source of the observed sound. There is a need for uninvasive diagnostics because of risks involved using anaesthetics on young children. To find the obstruction from sound, first one needs to know what kind of sound is produced by what kind of geometry. Doing this numerically has the advantage of allowing one to change only one parameter at the time (geometric wise but also boundary condition wise).

Since this is a pilot study first a computational method needs to be developed and validated. From a literature study it could be determined what type of flow is encountered and how the problem can be tackled. A large eddy simulation is chosen as the method for simulating the flow because of its high accuracy compared to for example RANS or DES while not being too computationally expensive. A selective Smagorinsky model is chosen as subgrid scale model for its performance on transitional, wall bounded flow. For the acoustics a hybrid approach is used, because of the computational efficiency of this kinds of approaches. From the different hybrid methods available, Lighthill's analogy was found to be the most appropriate. This method allows the calculation of the near field acoustics in wall bounded flows.

After implementing the code into OpenFOAM, it is tested on a total of 4 different problems. The computational code is first used for the analysis of a reed instrument. This is mostly an external flow problem. It was found that the decoupling of acoustics and fluid flow can give errors in the solution. The influence of the acoustics on oscillation of the jet was missing leading to a different fundamental frequency. However the overall resemblance was good. The strength overlapped very good. Also the peaks in the spectrum could be explained (but did not fully overlap).

Next an internal flow problem is analysed; namely a diaphragm model. Both numerical and experimental data is available. This data is for two different flow velocities. For both models the spectra overlapped at least partially with the reference data. Better agreement was found with the experimental results than with the numerical reference. Further the  $U^4$  law, an empirical relation describing the noise increase with increasing flow velocity, could be retrieved from the results.

The previously described two models show that the Lighthill equation can be used to get good results for acoustic simulations in the range that is also seen for the upper airway models. It is expected that the coupling between flow and acoustics is less of a problem for the upper airway models. The kind of coupling seen in a reed instrument is of a different nature than the kind of coupling that could be seen in an airway model. Further it is expected that the results will give close to realistic power distribution, good enough to see the most

important features. It should be noted that the lower frequencies are slightly over predicted.

Next a simplified upper airway model is analysed. The fluid results are close to experimental values for the original model. Also it is shown that the implemented LES SGS model performs better than a One equation SGS model and the pure Smagorinsky model. Further an acoustic analysis is performed on the geometry. Two constrictions are applied just below the glottis: one of 50% and one of 75%. The models clearly showed an increase in acoustic sources for the constricted cases as is expected intuitively. However the propagation of the sound towards the inlet is shown to be blocked by the constriction. This resulted in lower than expected values, especially for the highly constricted case. However a very large pressure drop is seen for the 75% compared to the other cases, therefore this model is more prone to tissue into vibration (if flexible walls would be taken into account). It might be the case that for increasing constriction the sound production mechanism shifts from turbulent sound production to tissue vibration. Near the outlet the sound pressure level is higher than the healthy case for the frequency range

The realistic upper airway model that is derived from a CT-scan is altered to also get a healthy patient. These two models are analysed and show similar results as seen for the simplified upper airway. Also for this case it is seen that part of the signal is blocked by the constriction. At the outlet the stridor patient shows a clear increase in sound pressure level. However at the inlet the signal not as strong, and the spectrum is even below the healthy patient at some parts.

When looking at all results presented in the thesis it can be concluded that the Lighthill equation can be used for flow regimes encountered in upper airways. The flow results looked good and are accurate enough to perform an acoustic simulation. When looking at the spectra generated by the upper airway models the overall distribution could be possible, if compared to actual stridor sounds, however peaks are missing in the spectrum and the lower frequencies seem over predicted. Probably the peaks can only be captured by using flexible walls. Therefore it is needed to incorporate more physics into the computational model. A rigid wall approach is not sufficient to predict stridor sounds numerically.

# Introduction

Stridor is an abnormal, noisy or toned/voiced breathing sound which is caused by obstruction or malformation of pharynx, larynx, trachea or the bronchia; whereby the turbulence of air and vibration of surrounding tissue are the source of the observed sound. Especially with children stridor is an indicator for possible severe obstruction and requires careful examination; a narrowing by 1mm can increase airway resistance 16-fold while decreasing the cross-sectional area by 75%. To examine a stridor patient, he/she is anesthetized and using an endoscope (a camera on rigid/flexible tube) the upper airways can be investigated. For young children, in particular, this is an unwanted procedure since the use of anesthetics can be a burden for the health of the patient. Therefore less invasive diagnostic possibilities are favourable and need to be investigated.

It might be possible to judge the obstruction that is causing the stridor, at least to some extent, by listening to the sound that is produced. However, before one can do this first more information is needed about the relation between obstruction and sound production. Different parameters like, obstruction size, flexibility, location, and shape influence the sound that is generated. To investigate this influence experimentally is difficult since every patient has slightly different upper airways and obstruction shape. Therefore it is difficult to vary one parameter while keeping others constant. Numerically this is less of a problem; the model can be adapted using a computer to change a single parameters at the time. Also this research can be performed for different patients to see whether the influence of a particular parameter is universal (i.e. holds for every patient), such that generalizations can be made. If all goes well this could help doctors in the future to assess the cause of stridor by using a database of acoustic results to get a first diagnosis of the problem. The first step that needs to be performed however is to see whether or not it is even possible, using contemporary technology, to predict the stridor sound numerically for a given geometry, before the reversed problem can be solved.

This report will cover a pilot study on the feasibility of acoustic analysis on stridor patients using a numerical approach. The report is meant to be a stepping stone for future research in the subject. Because of the nature of this study, validation of the different parts of the computational model that is developed is very important. Simply put, the computational model consists of an acoustic part and a fluid dynamics part. The performance of both these parts will be checked using examples from literature that are (closely) related to the subject. When both parts are validated, the computational model will be applied on a realistic model to see its applicability for research in stridor.

First the goals and project set-up are discussed in the upcoming two sections. This is followed by a chapter covering background information for the project consisting of a short description of the human airways and a summary of relevant work that has already been performed

on stridor and numerical analysis of the upper airways. This will give better insight in the problem and a better feel for what kind of results can be expected. Next the computational model is described in chapter 2. Different options for modelling techniques exists to tackle the fluid and acoustic part of the problem. The choices are given and argumentation to why these choices are made is given in this chapter. These choices are validated to give some insight into the accuracy that can be expected by using the final computational model. The acoustic part of the validation, using a reed instrument and diaphragm model as a testcase, is discussed in chapter 3. The validation of the fluid part, on a simplified upper airway model, is done in chapter 4. The experience that is gained during the validation can now be used to analyse a realistic upper airway model, for which no fluid nor acoustic data is available. This is discussed in chapter 5. From the results of the thesis some conclusions are drawn. Further the results are used to figure out what next steps can be taken to pave the way toward a world where the obstructions in the airways can be determined by analysing acoustic data. This future development is covered in chapter 7, together with the recommendations.

## Goals

The main goal of this thesis is to show the feasibility of performing an acoustic analysis of a stridor patient using a numerical approach. It is good to have some concrete points that are to be investigated. This research aims to answer the following questions:

1. Are the acoustic waves generated by the acoustic sources propagated through an internal domain accurately?
2. Can the difference between a healthy and stridor patient be seen based on the noise sources/ sound propagation?
3. Can similar results be obtained for simplified and realistic models?
4. Is it possible to obtain a realistic sound spectrum using rigid walls?

Please note that since this is a pilot study, it is not expected that the sound that a stridor patients produces can be calculated accurately immediately. The complete problem consists of many different phenomena (i.e. tissue vibration and possibly large scale deformation, turbulent sound production, sound convection/reflection/transmission/refraction/absorption, unsteady cyclic in and outflow), which makes it difficult to solve the problem numerically in one go. Probably an iterative approach is needed to find out which phenomena are most dominant and must be taken into account. Hence for this study only a basic model is developed and tested, which allows for further improvements in future research.

## Project set up

In order to come up with a proper computational model the following steps are followed.

- (a) A literature study is performed to investigate possible options for the build up of the fluid and acoustic computational model. Also research is done in alternative methods(experimental approaches for example) and into work that has already been performed by others in similar or comparable subjects.

- (b) The options found during this literature study are implemented (computational code development), tested and, where needed, changed.
- (c) The acoustic part is tested to see if the results are sound, by validating with published result of test cases.
- (d) The performance of the fluid part of the code is checked on an airway model of which good reference data is available.
- (e) Finally the developed tool can be applied on something new, to investigate acoustic properties of airway models.

The first step is documented in a report by Lynch C.T. (2011)[26]. For the third step two different (geometric) models found in the literature study are recreated using the same layout and parameters and are analysed using the custom created code. The acoustics of a reed instrument and a diaphragm flow are analysed, this is documented in chapter 3. The reed instrument is a (partly) external flow problem, the noise sources and frequency spectrum can be compared. Because this problem is mostly external, reflections are of lesser importance hinting that this problem is probably simpler than most internal flow problems. The diaphragm is a fully internal flow and might show behaviour that is more similar to what is seen in an airway model. Also for this model a frequency spectrum is available. Both of these models show velocities that could also exist in a real human airway. Also the Reynolds numbers do not deviate much. For the reed instrument the Reynolds number based on jet velocity and jet length is approximately 4.100, for the diaphragm based on jet velocity and aperture height the Reynolds number is approximately 52.700, for the simplified upper airway Reynolds numbers are seen of 10.000 and 5500 and for the realistic upper airway Reynolds numbers of 8.600 and 4.300 are seen (Using jet velocity and trachea mean diameter). Therefore it is expected that a similar accuracy will be found when applied to an upper airway model.

The validation of the computational fluid dynamics (CFD) part of the code is tested on a Simplified Upper Airway Model (SUAM) of which experimental data is available (covered in chapter 4). The model is a simplified form of a computed tomography-scan (CT-scan) derived model and should show flow structures that are similar to a realist human airway model. If the fluid flow in this model can be calculated accurately, a similar approach should yield approximately equal accurate results for a fully realistic model. This model is also used to investigate acoustic properties of the airways by altering the cross sectional area below the vocal cords (artificial constriction).

Finally the code is applied on a Realist Upper Airway Model (RUAM), which is derived from a CT-scan (see chapter 4). This model is adapted to a more healthy person in a meshing program. Although it is rather subjective whether the edited model is fully healthy it should resemble a healthy person more closely than the original model and allow for comparison.

The different models that are introduced shortly in this section should allow to find the answers posed in the goals section. A more elaborate description of each model is found in the chapter corresponding to that model.



# Chapter 1

## Properties of the respiratory track and stridor

This chapter will cover the most important background information concerning the respiratory track and stridor. This knowledge is fundamental for building up a realistic computational model, which is discussed in the next chapter. First the geometric layout of the respiratory track is discussed in section 1.1, followed by a section covering the aerodynamic properties of this system. Then the stridor phenomenon is discussed in section 1.3. Finally relevant acoustic and mechanical (for the sake of completeness) properties are discussed in the last section.

### 1.1 Respiratory System

The respiratory system consists of the airways, lungs and the respiratory muscles. This system makes sure humans are able to passively exchange oxygen and carbon dioxide. Air flows in from mouth or nostrils and are guided into the lungs to the alveoli where the exchange of gasses occurs. The system can be separated into the upper respiratory tract and the lower respiratory tract. The upper tract consists of the nasal cavity, oral cavity, pharynx and larynx. The lower tract can be divided into the trachea bronchial tubes, bronchioles and alveoli. This general overview can be seen in figure 1.1; all afore mentioned parts of the respiratory system are briefly elaborated on in the upcoming sections.

#### 1.1.1 Nasal cavity

The nasal cavity of humans is very complex in morphology as can be seen in figure 1.2. The flow in the left and right nostrils remain separated by the septum and only come together near the nasopharynx (NP) which is at the end of the nasal cavity. In slice 2-2 one gets a better view of the geometry; The main flow goes through the medial passage (MP) (highest velocity)[21], while in the thinnest parts of the meatus the air slows down (edges of MM,SM,IM). Notice how the flow needs to bend 180° from nostril to nasopharynx.

#### 1.1.2 Oral cavity

The oral cavity has a somewhat easier comprehensible geometry. The most important features can be seen in figure 1.3. Aerodynamically the uvula is the most interesting, since it looks

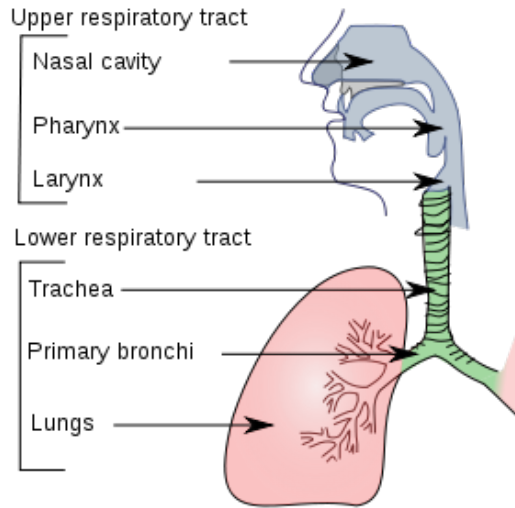


Figure 1.1: General overview respiratory system

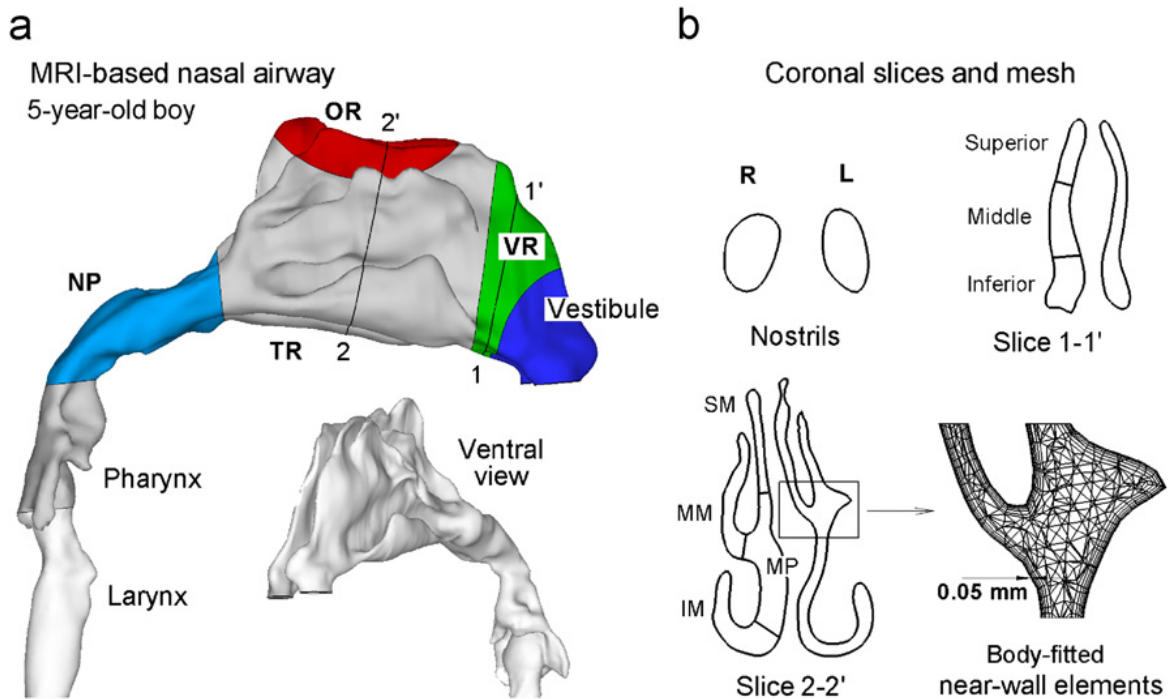
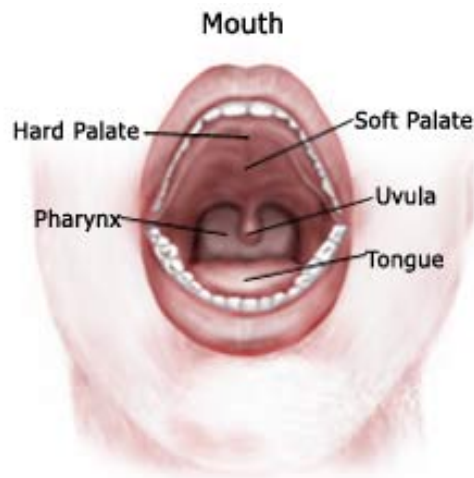


Figure 1.2: Nasal cavity layout

like an obstruction in an otherwise relatively smooth section.



**Figure 1.3:** Oral cavity layout

### 1.1.3 Pharynx

The human pharynx is situated between the oral and nasal cavity and the larynx. It is part of both the digestive and respiratory system. The pharynx is divided into three parts: nasopharynx, oropharynx and laryngopharynx. This is also the place where the oral and nasal cavity come together.

### 1.1.4 Larynx

The upper part of the larynx is connected to the epiglottis which makes sure no food is directed to the trachea. The larynx also holds the vocal folds or vocal cords making it an important organ for communication. When breathing the folds are opened where as for sound production the folds are closed. In figure 1.4 a top view can be seen of the larynx.

### 1.1.5 Lower respiratory tract

The trachea serves as the connection between the larynx and the lungs. It has cartilages or tracheal (c shaped) rings, which make sure that the trachea keeps its shape. On the inferior side the 'pipe' splits up at the first bifurcation, becoming the primary bronchi. One side goes to the right three lobes, and the other to the left two lung lobes (The right side is bigger; the left side needs to make room for the heart). The bronchi keep splitting up, until finally the alveoli are reached where the actual gas exchange takes place. See figure 1.5 for an overview of this.

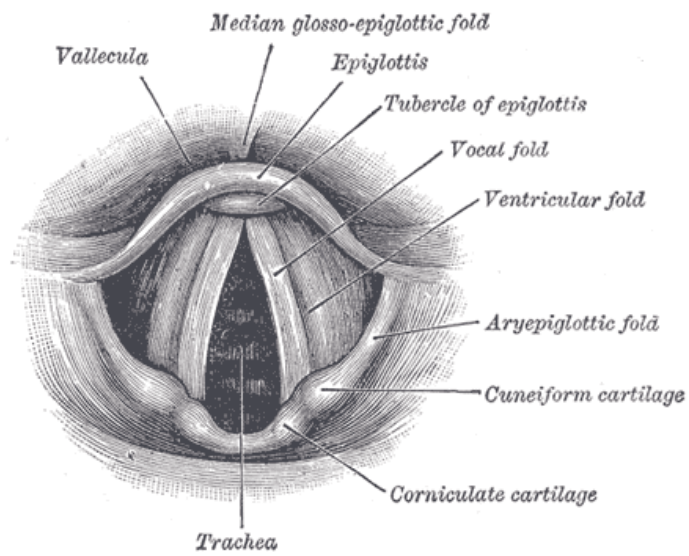


Figure 1.4: Larynx layout

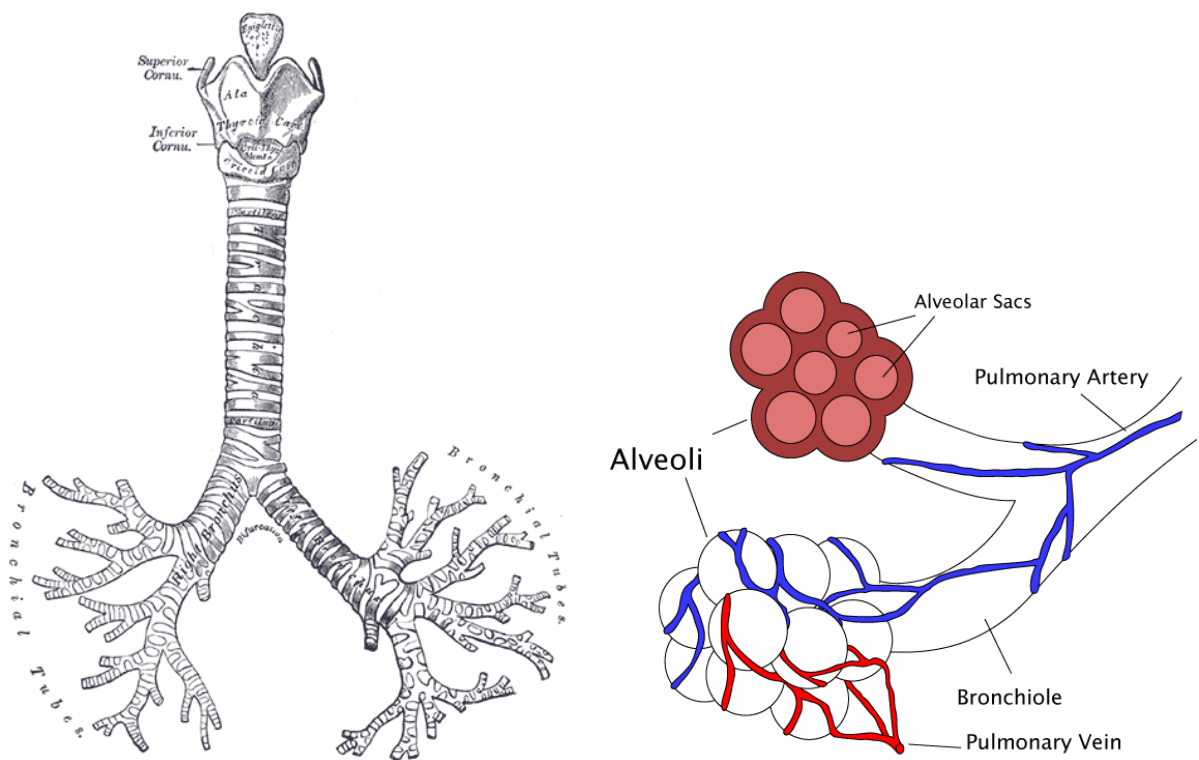


Figure 1.5: Lower respiratory tract (left), Alveoli and bronchiole (right)

### 1.1.6 Geometric parameters

Much of the literature concerning simulations of airway sections are focused on adult respiratory systems. Therefore it is important to note some geometry wise differences between infants and adults. In figure 1.6 the cross-sectional area, perimeter and hydraulic diameter are plotted for a healthy 53-year-old male who is non-smoking, and a 5-year-old boy. In table 1.1 the volume, surface area and effective diameter are given. The data given in this section is extracted from reference [21]. For this research, a model of an adult stridor patient is used. This model is discussed in chapter 5. An adult model is used simply because it is the best, most complete, model that was available of a stridor patient at the time of this study. Future research might however be focused more on infants since this is more of a problem group as is explained the introduction of this thesis.

**Table 1.1:**

<sup>a</sup>V&V (vestibule and valve region), TR (turbinate region), NP (nasopharynx).  
<sup>b</sup>Effective diameter  $d_e = 4V/A$ .  
 from [21]

Anatomical sections <sup>a</sup>	Volume, $V$ ( $cm^3$ )		Surface area, $A$ ( $cm^2$ )		Effective diameter, $d_e^b$ ( $cm$ )	
	5-year-old	Adult	5-year-old	Adult	5-year-old	Adult
V&V	3.37	5.50	23.74	35.58	0.568	0.619
TR	11.03	12.63	107.34	112.59	0.411	0.449
NP	3.95	16.33	15.27	40.93	1.034	1.595
Pharynx	2.64	13.89	14.59	45.10	0.724	1.232
Larynx	1.22	6.70	7.20	21.81	0.676	1.228
Total	22.21	55.05	168.14	256.01	0.528	0.860

## 1.2 Typical airflow

The human airways are very complex in shape as can be seen from the previous figures. When one inspires, the airflow mostly flows in from the nose and travels through the airways finally ending in the alveoli. In between, the flow needs to bend  $180^\circ$ , it encounters ducts and also cavities are passed. These features in combination with the airflow velocity allow for very interesting flow structures and phenomena like: flow separation, recirculation, highly curved stream lines, acceleration and deceleration, transition from laminar to turbulent flow and vice versa.

In figure 1.7 one can see the velocity distribution of a realistic upper airway model of a healthy 53-year-old man. Some geometric features of the airway of this man are given in section 1.1.6. Clearly the main flow in the nasal cavity flows through the main passage while at the outer parts, it slows down. Further if we look at the turbulent kinetic energy  $k$  (figure 1.8) we see laminar flow in the edges (where the slower velocity exists), while turbulent flow is found in the main passage and nasopharynx. Therefore it is clear that flow in the airways is laminar, transitional and fully turbulent[41].

To make it even more interesting flow is not only possible in one direction, neither is it steady. Nonetheless for quiet breathing (approximately  $0.2L/s$ , at  $0.25Hz$ ), the Strouhal

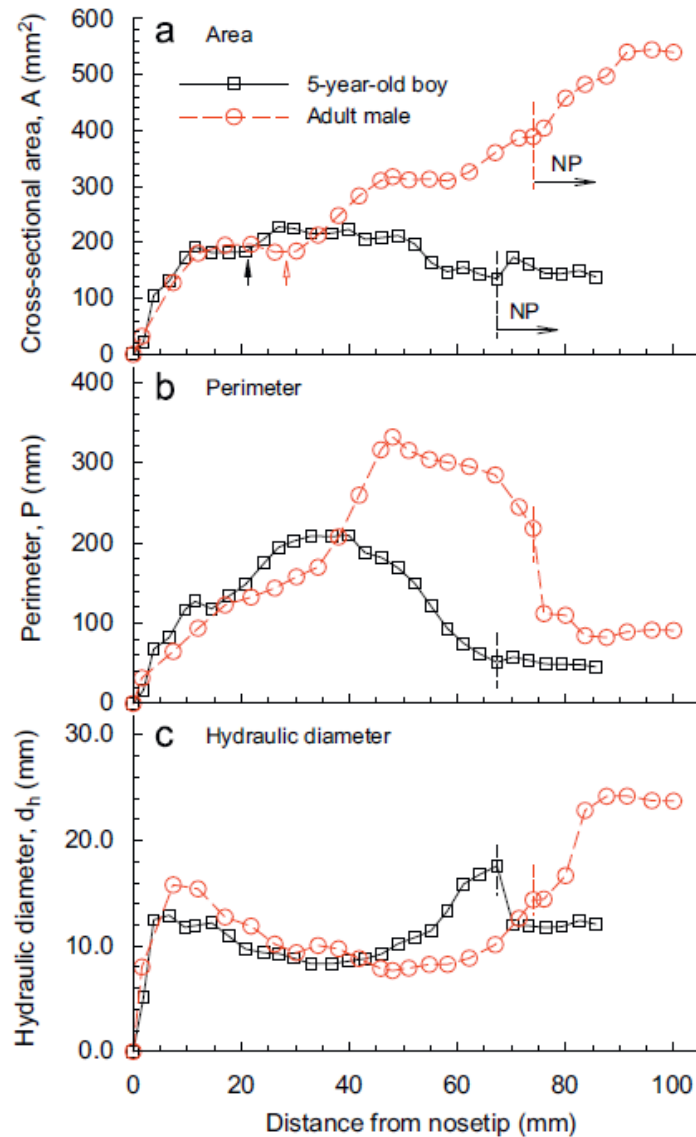


**Figure 1.6:** Comparison of nasal cross-sectional area, perimeter and hydraulic diameter between a 5-year-old boy and an adult male as a function of the distance from the nose tip. The nasal valve is marked with a solid arrow for the child and a hollow arrow for the adult. The vertical dashed line denotes the start of the nasopharynx (NP). (a) The cross-sectional area ( $A$ ) and (b) perimeter ( $P$ ) are the summation of right and left passages. (c) The hydraulic diameter is calculated from the relation  $d_h = 4A/P$ . [21]

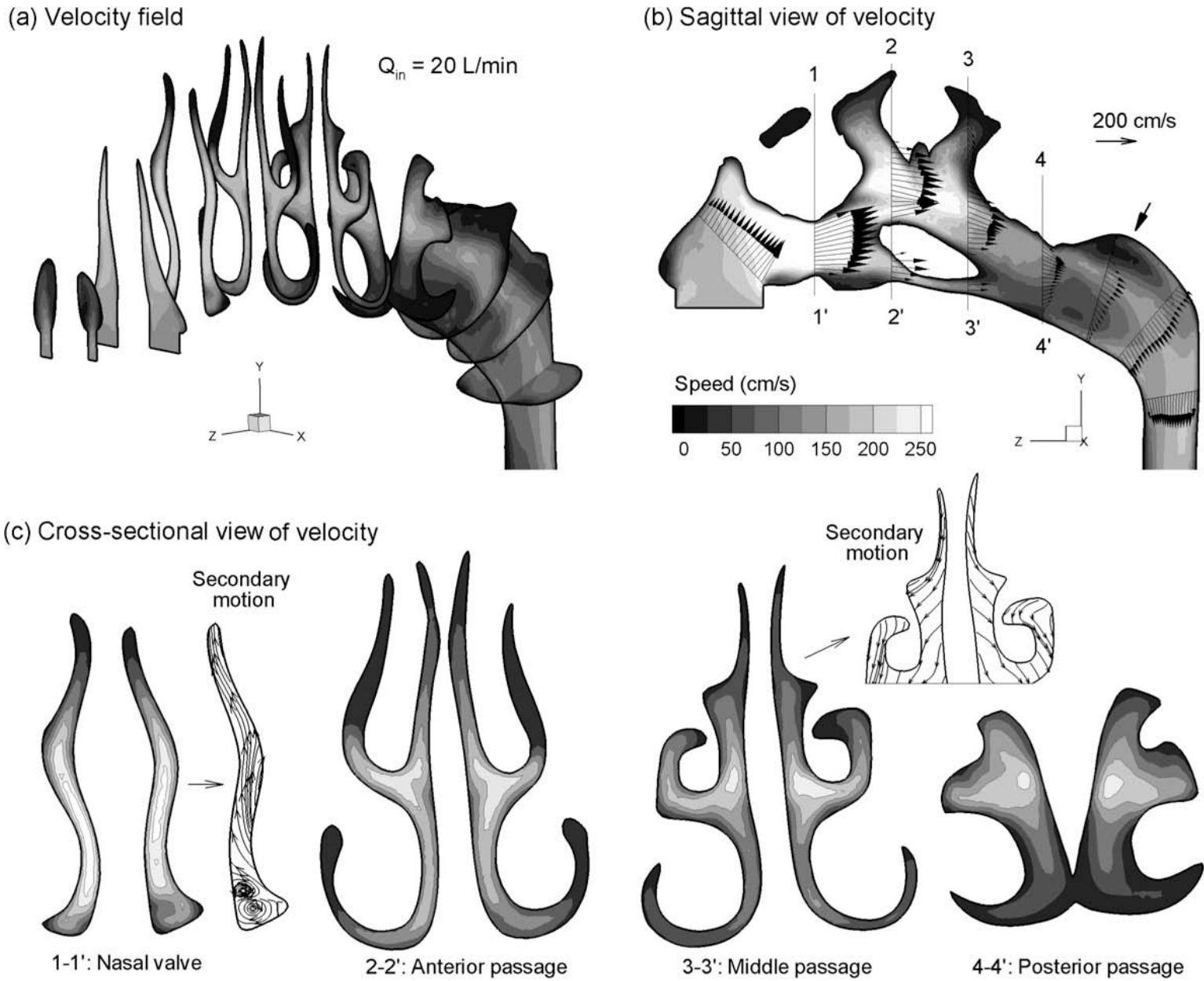


**Figure 1.7:** Velocity fields in the nasal passages at an inhalation flow rate of  $0.33 \text{ L/s}$  in (a) 3-D, (b) sagittal, and (c) cross-sectional (coronal) views. The filled arrow marks the location of flow separation and recirculation in the nasopharynx.[41]

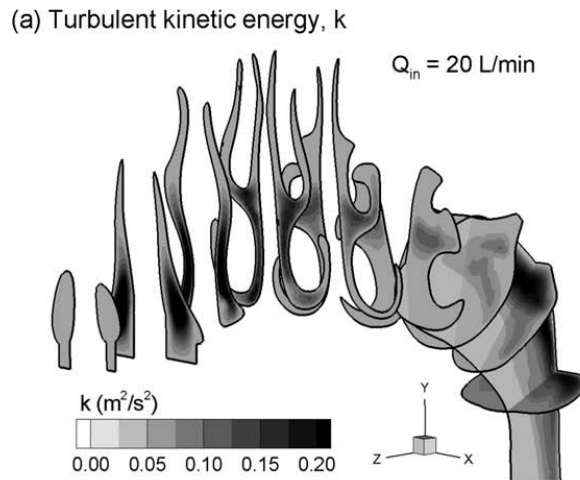


**Figure 1.8:** Turbulent kinetic energy, reference[41]

number is less than 0.2 in the nasal cavity. This indicates that a quasi-steady approximation is reasonable[22]. Also Olsen et al. (1973)[31] showed experimentally that during inspiration the steady flow assumption is valid for flow rates up to  $2.5L/s$ . Calay et al. (2001)[10] showed that when the peak velocity is reached flow is similar to results obtained from quasi-steady results, during acceleration and deceleration however different velocity profiles are seen in the model (asymmetric bifurcation model).

For an adult typical the normal flow rates are:  $0.2L/s$  for light breathing and  $1.67L/s$  for heavy breathing. Using this data the Reynolds number varies from approximately 800 for light breathing to 9300 for heavy breathing[37]. For a child this is:  $0.05L/s$  in sedentary condition and  $0.5L/s$  for a heavily active condition. This corresponds to a Reynolds number of 368 and 3302 respectively[21].

### 1.3 Stridor

Stridor is an abnormal, noisy or toned/voiced breathing sound which is caused by obstruction or malformation of pharynx, larynx, trachea or the bronchia; whereby the turbulence of air and vibration of surrounding tissue are the source of the observed sound. An overview of the causes of stridor is given in section 1.3.1. Some studies have been dedicated to the type of noise that is produced by the obstruction(or by the throat in general). A small overview of these studies and their results are discussed in section 1.3.2

#### 1.3.1 Causes of stridor

There are many different types of airway obstruction that will cause stridor. In general inspiratory stridor indicates upper airway tract obstruction, whereas expiratory stridor indicates lower airway tract obstruction[36][17]. When the stridor is caused by soft tissue this can be explained by the fact that during inspiration the negative pressure gradient in the airflow towards the lungs creates suction; this can cause the epiglottis to be sucked toward the lung, and combines with arytenoid tissues to create a tube with diameter much smaller than the

remainder of the respiratory tract. Another possibility is that the soft tissue in the *upper* part of the trachea collapses due to the difference between ambient pressure and the more negative pressure in the trachea tract itself during *inspiration*[36]. In the lower part of the trachea this is not a problem (in the bronchi the pressure is even lower). During the *expiration* the increased pressure in the lungs can cause the trachea's *lower* soft tissue to collapse (pressure in lungs is higher than in trachea).

Especially with children stridor is an indicator for possible severe obstruction and requires careful examination; a narrowing by 1mm can increase airway resistance 16-fold while decreasing the cross-sectional area by 75%[12]. There are many possible causes for the occurrence of the stridor phenomena. The most common cause (for children) is laryngomalacia in the chronic case and laryngotracheitis in the acute case[45]. Laryngomalacia (see figure 1.9) occurs as a result of a floppy portion of the larynx that has not yet developed the strength to provide rigid support of the airway. During inspiration this structure can collapse creating a narrowed passaged inducing a toned sound[38]. Laryngotracheitis (see figure 1.10) is an inflammation of the mucous membrane, which is responsible for the formation of slimy substances (mucus), located in the larynx and trachea, which causes a narrowing of the airways. Some other causes are: vocal cord paralysis, tracheomalacia (floppy walls in trachea), stenosis (constriction, see figure 1.11), tumors and granuloma (mass that is formed to wall-off perceived foreign substances). Depending on the site of the lesion the stridor is classified as: Supralaryngeal, supraglottic, glottic and subglottic and tracheal[6]. See table 1.2 for a short, rough overview.

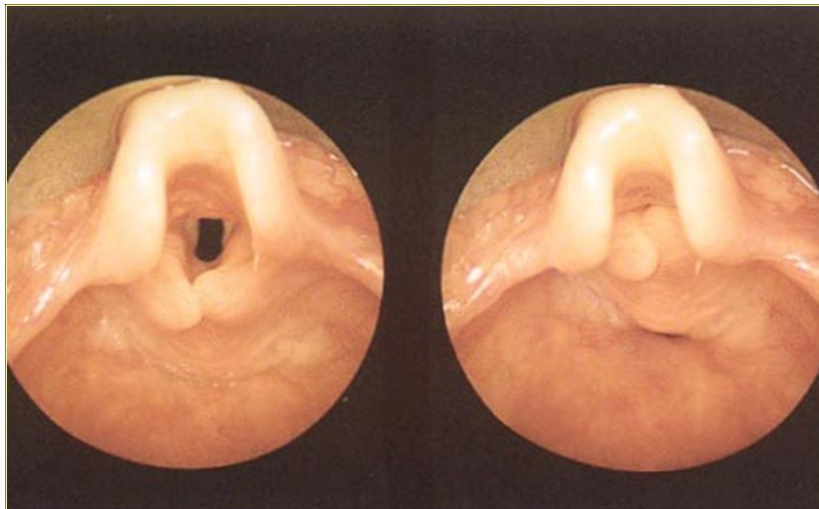


**Figure 1.9:** Laryngomalacia, arytenoid tissue collapses

### 1.3.2 Studies on stridor sounds

Efforts have been put into correlating the sound of stridor to location and or cause. Zwartenkot[44] used spectrograms to find differences between stridor sounds of multiple patients with different causes occurring at different locations. An example of such a diagram for stridorous sound from a child suffering from laryngomalacia can be seen in figure 1.12. He found it difficult to

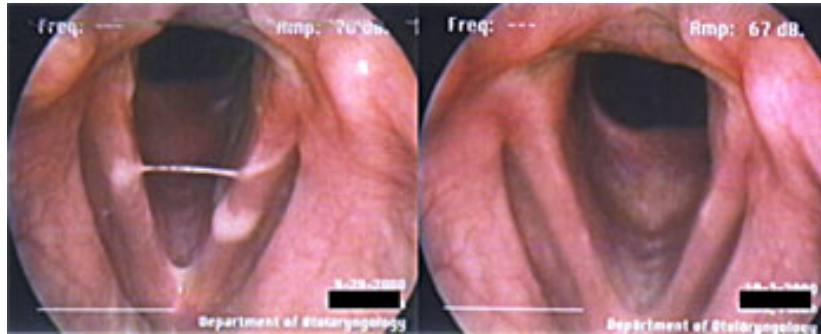


Figure 1.10: Laryngitis (left), resolved laryngitis (right)



Figure 1.11: Subglottic stenosis

Table 1.2: Rough classification of stridor (infants)

\*[43], +[45], #[1], %[44]

<sup>1</sup>granuloma do not necessarily need to be supraglottic this is an example from[44]

Cause	Part of cycle	Placement	Deformation	Occurance
Laryngotracheitis	N.A.	glottic/supraglottic	small	common <sup>+</sup>
Laryngomalacia	inspiration <sup>%</sup>	supraglottic	very large deformations	very common <sup>*</sup>
Vocal cord paralysis	inspiratory <sup>%</sup>	glottic	small	N.A.
Tracheomalacia	inspiration	upper part trachea	large deformation	uncommon <sup>*</sup>
	expiration	lower part trachea	large deformation	uncommon <sup>*</sup>
Subglottic stenosis	inspiration <sup>%</sup>	subglottic	very small	N.A.
Tumors	N.A.	N.A.	small	very rare <sup>#</sup>
Granuloma	inspiration <sup>1</sup>	supraglottic <sup>1</sup>	small	uncommon <sup>#</sup>

come to a conclusive correlation between diagram, location and cause; more data are needed.

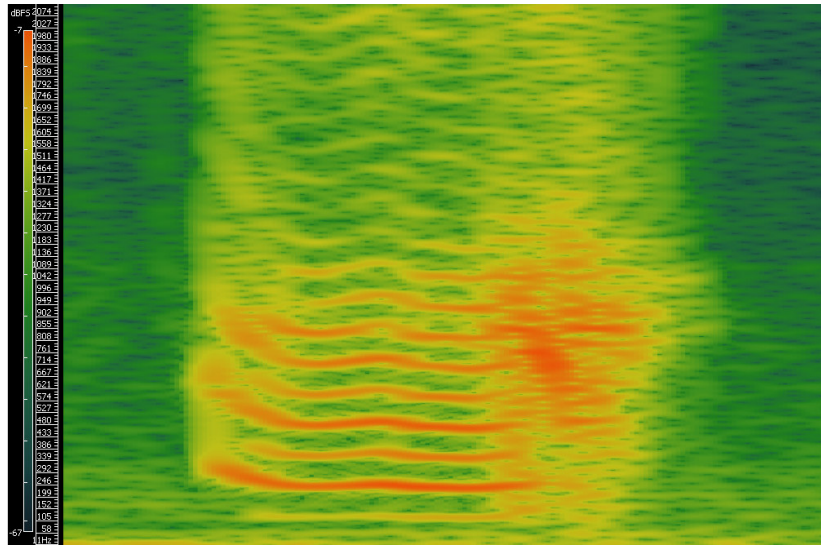


**Figure 1.12:** Spectrogram laryngomalacia[44]

Slawinski and Jamieson (1990)[36] found that *voiced* sources are observed when a sufficiently large pressure drop induces vibration in the tissue surrounding the constriction. The frequency of this vibration depends on two properties of the surrounding tissue: elasticity and mass. Vibration frequency decreases as the tissue enlarges or softens. Fricative sources will result when the pressure drop is too small to stimulate the surrounding tissue into periodic vibration, provided that there is sufficient pressure to produce a turbulent airflow past the constriction. With higher airflow velocities, the dominant spectral frequencies of the fricative source will shift to higher values. The acoustic signal generated by a fricative source is transformed by the entire respiratory channel whereas a voiced source is only shaped by that portion of the respiratory tract between source and receiver.

The most important conclusions from this research are cited below:

- (a) the location of the constriction: constrictions placed close to the nostrils emphasize higher frequencies and maintain similar values of murmur duration and intensity in both phases of the respiration cycle. Constrictions close to bifurcation increase the amplitude of lower frequencies and prolong the expiration phase.
- (b) the mass and elasticity of the tissue surrounding the constriction: large mass and low elasticity tend to result in a fricative source, reflected in the murmur as a noise with formants corresponding to natural frequencies of the respiratory tract. Smaller mass and higher elasticity tend to result in a voiced source, which appears in the murmur as a tone.
- (c) the shape of the constriction: long constrictions tend to generate fricative sources, while short constrictions tend to generate voiced sources (if the pressure drop is sufficiently large).
- (d) the cross-sectional area of the constriction (for fricative sources): lower frequencies dominate the signal spectrum when the airway is relatively large, while higher frequencies

emerge as the airways narrows. (also confirmed by Gray et al. (1985)[16])

- (e) the tissue tension (for voiced sources): high tension gives a high-frequency tonal quality to the murmur, while lower tension shifts the fundamental frequency (pitch) of the murmur to lower values.
- (f) the mobility of the constriction: with stable constrictions, resistance to airflow is equivalent in both phases of respiration and stridor is produced in both phases. Unstable constrictions produce changes in the spectrum from one cycle to the next and within each cycle.
- (g) The ratio of the duration of the constriction opening to the period of tissue vibration (for voiced sources): a small value of ratio (much lower than 1) is reflected in the spectrum of a murmur by many harmonics of fundamental frequency, while an appearance of only a few harmonics indicates that a constriction lumen is open much longer.

Leiberman et al. (1986)[23] tried to use a very simple acoustic model to estimate location and obstruction size. The upper airway tract was assumed to be an acoustic tube with varying cross-sectional areas, starting from the glottis, and ending at the lips and nose. The tube was assumed rigid and discretized sufficiently well. Using those assumptions the areas of the tube could be estimated directly from the acoustic signal (of stridorous sound). These estimates could provide useful during diagnosing the cause for stridor, although further development is still needed.

Milenkovic (1984)[29] tried to estimate the focal tract shape by measuring the pressure at two points; one at the inlet, and one at the outlet. His two point method seemed robust and he was able to reproduce area functions using the measurement data of speech.

## 1.4 Acoustic and mechanical properties

For simulation purposes the determination of the acoustic and mechanical properties are of importance. For this master thesis only the acoustic properties will be of use, however the mechanical properties might come in hand in further research.

The two most important parameters in acoustics are density and sound speed. Both of these parameters are influenced by the temperature. During a respiratory cycle the temperature of the air and boundary tissue changes. For both air and tissue the temperature in the core of the human is higher than near the boundary. Especially in more extreme conditions temperatures can change quite a bit; in the winter for example the body temperature is approximately  $35^\circ$  while the outside temperature could be even below the freezing point. These temperature changes cause for example diffraction of sound waves. However for this thesis it is assumed that the variation is small enough such that its effects can be neglected. Taking into account the temperature would make the problem at hand even more complex than it already is, while it is believed it will not add to the overall accuracy in this early stage of research. A temperature of  $25^\circ C$  is assumed giving rise to a density of  $1.1839 kg/m^3$  and a sound speed velocity of  $346.18 m/s$ .

Another property that is important for this thesis is the impedance. When an acoustic waves hits a wall part of the wave is reflected while an other part moves forward. The

relationship between the amplitude of the incoming wave, the transmitted wave and the reflected wave is a function of the impedances and wave front angle. This relation is governed by the following equations:[34]

$$\frac{B}{A} = \frac{2\rho_2c_2 \sin \delta_i}{\rho_2c_2 \sin \delta_i + \rho_1c_1 \sin \delta_t}, \text{ and} \quad (1.1)$$

$$\frac{C}{A} = \frac{\rho_2c_2 \sin \delta_i - \rho_1c_1 \sin \delta_t}{\rho_2c_2 \sin \delta_i + \rho_1c_1 \sin \delta_t}. \quad (1.2)$$

Where  $A, B$  and  $C$  represent incoming, transmissive and reflective amplitude respectively,  $\delta_i$  and  $\delta_t$  are the incoming and transmissive angle of the wave front respectively, and  $\rho_1c_1$  and  $\rho_2c_2$  are the impedances of two different mediums. For some tissues near the upper airway track the impedances are given in table 1.3

**Table 1.3:**

Approximate value for the impedance of different parts of a human, see [5][18][25]

Material	Impedance (MRayl)
Air	0.0004
Fat	1.38
Water	1.48
Blood	1.51
Soft tissue (average)	1.63
Musle	1.7
Bone	7.8

To give a sense of what the flexibility of the tissues surrounding the respiratory track are, the results of two research articles are shortly summarized.

Teng et al.(2008)[40] found a way to model the mechanical properties of the cartilage rings of a pig. It was found that the E-modulus is approximately  $57.915MPa$ . However a linear formulation did not give a satisfactory result whereas there proposed non-linear approach did.

In the paper by Xu et al.(2009)[42] an elastic model was used to model different tissues in the upper airway. The tongue, palate and surrounding tissue were modelled independently. Using MRI scans of a rat the movement of the different components was recorded (during pressurization of the rat). From this they extracted boundary conditions and finally also the material properties. The modulus was iteratively changed from values slightly above the ones obtained from literature ([19][27]) to values that matched the observed MRI deformation within 20%. This resulted in E-modulus values of 6000, 7000 and  $15000Pa$  for tonge,airway tissue and soft palate respectively.

For a more complete list of tissue modeling efforts you are referred to the literature study report by Lynch, C.T.(2011)[26]



## Chapter 2

# The computational model

In this chapter different ingredients of the computational model are discussed. First the chosen aerodynamic formulation is discussed in section 2.1. This is followed by the acoustic modeling in section 2.2. Then the boundary conditions are discussed in a general way. The model specific boundary conditions are elaborated on in each model's chapter.

### 2.1 Aerodynamic formulation

From a literature study [26] we concluded that the most appropriate way to calculate the fluid flow is using a large eddy simulation (LES). This is mainly because of the high accuracy (compared to for example DES, RANS or URANS), shown for both purely CFD but also acoustic simulations. Given the flow properties as presented in section 1.2, it is possible to use an incompressible approach (maximum Mach number diaphragm:  $M = \pm 0.16$ , maximum Mach number airway models  $M = \pm 0.06$ ). Pursuing a compressible approach might give an extra way to check the acoustic modeling. This would, however, be at the cost of more complex airflow modelling (i.e. more equations, more variables, more boundary conditions) and extra computational time. Further extra care has to be taken when extracting acoustic waves since the mean and fluctuating part of the variables are not decoupled, making the signal to noise ratio lower. For this thesis the incompressible Navier-Stokes equations are used for the sake of simplicity. For the encountered flow regime this set of equations can give accurate results. Other methods are sought to validate the acoustic simulation.

When using LES, there are different options available to model the subgrid scales. From the literature study mentioned earlier it followed that a selective subgrid scale (SGS) model would probably perform best, given the transitional behaviour of the flow. What a selective model essentially does is turning off the SGS model when the flow properties do not correspond to expected values for fully turbulent flow. Implicitly this also causes the beneficial behaviour of turning off the eddy viscosity near the wall[35].

In this thesis the selection function as described in the paper by Sagaut et al.(1999)[35] is used:

$$f_s(\theta, \theta_0) = \begin{cases} 1 & \text{if } \theta \geq \theta_0 \\ r(\theta, \theta_0)^{1/2} & \text{else} \end{cases} \quad (2.1)$$

$$r(\theta, \theta_0) = \frac{\tan^2(\theta/2)}{\tan^2(\theta_0/2)}, \quad (2.2)$$

where  $\theta$  is the parameter used to determine the three dimensionality of the flow (in this case the angle between vorticity vectors) and  $\theta_0$  is the threshold value of  $\theta$  above which the selection function is turned on.

In this thesis the flow property criterion as given in Farhadi, M and Rahnama, M(2006)[14] is used. They propose that the flow can be considered turbulent, or 3 dimensional enough, when the vorticity angle between one point and the average of the surrounding points is larger than  $20^\circ$  (hence  $\theta_0 = 20^\circ$ ). The resulting model is compared with two other LES SGS models in section 4.3, to see how it performs on an airway model.

## 2.2 Acoustic modeling

In the literature different methods are found to model the acoustics from a flow simulation. These methods all fall under the common used abbreviation CAA (computational aeroacoustics). It is possible to calculate the acoustic waves directly using the conservation laws governing fluid flow, where during post processing it is tried to split the mean and fluctuating part of the pressure. Most methods pursue a hybrid approach where one solver solves for fluid dynamics and a second solver, using these results, solves for+ acoustics. Examples of these are the Lighthill analogy, Kirchhoff integral, and the use of Ffowcs Williams-Hawkins surfaces.

Both the direct and hybrid approach show advantages and disadvantages. For the direct approach a very high resolution simulation is necessary because of the large differences in scales that are present (acoustic fluctuations can be multiple orders of magnitude lower than normal flow features). The advantage comes in by the fact that most physical effects are taken into account, such that strong acoustic waves can also interact with the flow. This allows for a coupling between acoustic and fluid flow modes. The main disadvantage is the very high computational demands that this approach requires. Also handling of the boundary conditions becomes extra critical (each variable needs to leave the domain smoothly such that inlets and outlets do not give noise to the acoustic signal).

Especially for low Mach number, simulations using a hybrid method can give very good results. The decoupling of the acoustic and fluid dynamics removes the need for a very high resolution CFD calculation. Also the signal to noise ratio is improved due to the decoupling. A disadvantage of hybrid methods is that not all physical effects are taken into account: coupling with fluid flow is not possible and depending on the applied approximations effects such as diffraction and reflections can get lost. The coupling is important for very strong acoustic waves, because these can have an impact on the fluid motion. Small waves will only cause very small molecular movement that do not influence the main flow structures.

For internal flow the two most suitable options are either direct solving of the Navier-Stokes equations or the use of the Lighthill equation as is concluded from literature study [26]. However the complexity and high computational demands for a direct approach make it the lesser option. This is partly because of time constraints. Since both the development of a working computational code and the application of the code (on multiple models) needs to be covered in one project.

The Lighthill equation can be used to calculate the near field acoustic field, also the propagation of the sound perturbations can be taken into account. This is ideal for the problem faced in the current research project. It can be used to see where sound production takes place, and how this sound production is affected by different geometries.

The equation can be obtained directly from the Navier-Stokes equations using differentiation and basic operations [24]. This will eventually lead to,

$$\frac{\partial^2 \rho'}{\partial t^2} - c^2 \frac{\partial^2 \rho'}{\partial x_i^2} = \frac{\partial^2}{\partial x_i \partial x_j} T_{ij}, \quad (2.3)$$

where  $c$  is the speed of sound,  $\rho'$  is the perturbation of the mean density and  $T_{ij}$  the Lighthill stress tensor which is given by the following relation:

$$T_{ij} = \rho u_i u_j + 2\mu S_{ij} + \delta_{ij}(p' - c^2 \rho'). \quad (2.4)$$

Where  $S_{ij}$  is the strain rate in the fluid,  $\mu$  is the dynamic viscosity,  $p'$  is the perturbation in mean pressure and  $\delta_{ij}$  the Kronecker delta function.

In multiple papers (see for example [7][30][32]) from which a couple are in a similar flow regime as will be encountered in this thesis, the Lighthill equation is simplified to

$$\frac{\partial^2 \rho'}{\partial t^2} - c^2 \frac{\partial^2 \rho'}{\partial x_i^2} = \frac{\partial^2}{\partial x_i \partial x_j} \rho u_i u_j, \quad (2.5)$$

This can be done under the assumption that the Reynolds number is sufficiently large that the dissipation by the viscous stress tensor can be ignored and that adiabaticity is well held. Under the incompressibility assumption this equation can be further simplified to become

$$\frac{\partial^2 \rho'}{\partial t^2} - c^2 \frac{\partial^2 \rho'}{\partial x_i^2} = \rho_0 \frac{\partial^2}{\partial x_i \partial x_j} u_i u_j. \quad (2.6)$$

The right hand side of the equation can be fully calculated from a CFD calculation. This allows for the decoupling of the acoustic and flow simulation. Because of this many authors use specialized acoustic simulation software to calculate the acoustics. This often means switching to the frequency space using the Fourier transform. For this thesis it is chosen to implement the Lighthill equation into OpenFOAM. This has several advantages. First, this allows for the quasi simultaneous simulation of both acoustic and flow parameters, thus every CFD time step is followed by several acoustic sub cycles (the time step for the acoustic simulation needs to be smaller in general because of the high wave velocity). Because this is done immediately after the CFD time step there is no need to save every time step thereby seriously reducing memory demands. Secondly the programming efforts are reduced significantly since both temporal and spatial discretization algorithms are preprogrammed in OpenFOAM. Thirdly post processing algorithms are also readily available for OpenFOAM, making the data analysis more convenient and less time consuming. Finally using a time accurate simulation for the acoustic variables allows for the investigation of the reflections and propagation visually.

## 2.3 Boundary conditions

Both for the acoustic and CFD simulation boundary conditions need to be applied. For the models presented in this thesis, the boundaries of the computational domain can be divided into roughly three groups: inlet, outlet, and walls. In this section some background information is given regarding the different types of treatment of the boundaries used on the models in this thesis. For model specific boundary conditions you are referred to the model's chapter itself.

### 2.3.1 Inlets and outlets

Depending on the problem different inlet and outlet conditions are applied. For the velocity this is either a von Neumann, a Dirichlet or pressure derived normal velocity boundary condition. In the last case OpenFOAM determines the inlet velocity based on the pressure gradient. This allows for non uniform inflow. When using this boundary condition smoothing was applied on the velocity to reduce peak velocities.

The pressure is set either using a von Neumann or Dirichlet boundary condition. This boundary condition can cause reflection. When calculating the acoustic pressure waves directly (i.e. not using the Lighthill equation) this is a major problem, but also for non acoustic purposes it can be of importance to make the boundary non-reflective since the reflected pressure influences the upstream flow structures. It is attempted to incorporate a sponge layer as formulated in Chen et al.(2004)[11].

$$\tilde{\mathbf{Q}} = \mathbf{Q} - \sigma(\mathbf{Q} - \mathbf{Q}_{target}), \quad (2.7)$$

where damping is applied to  $\tilde{\mathbf{Q}} = (\rho', u', v', w', p')^T$  each time step, and where  $\mathbf{Q}_{target}$  is a given reference. The damping coefficient  $\sigma$  is defined as

$$\sigma(l) = \alpha_2 \left( \frac{L-l}{L} \right)^{\beta_1}, \quad (2.8)$$

where  $l$  is the distance from the outer boundary of the buffer zone and  $L$  is the buffer zone width. Parameters  $\alpha_2$  (Chen used 1) and  $\beta_1$  (Chen used 1.5) are used to determine the nature of the damping coefficient  $\sigma$  which varies smoothly from zero at the interface between the buffer zone and propagation region to a value, normally one, at the outer boundary.

This method is applied to the acoustic waves  $\rho'$  and the pressure. After some tests it was shown that it works for the acoustic waves, for later simulations the reference value is not constant making this method inconvenient. For the density perturbations it was found that a convective outlet boundary condition (subset of Robin boundary condition)2.9, allowed the acoustic waves to leave the domain without reflections.

$$\frac{d\phi}{dt} + U_n \frac{d\phi}{dn} = 0 \quad (2.9)$$

In this equation, for the acoustic waves,  $\phi = \rho'$  and  $U_n = c$  where  $c$  is the speed of sound. The spatial derivative is taken normal to the boundary element. In test this method showed superior results compared to the sponge layer method.

For the pressure it was not clear if the method improved the results, after some instability issues the sponge layer was deactivated for precautionary reasons. Since for the models the acoustics were of main concern, the pressure sponge layer did not have a direct influence on the acoustic perturbations. Further since the pressure is becoming almost homogeneous near the exit for all models, it can be assumed the changes in flow structure (due to reflections) are small enough to have only small to no effect on acoustic frequency spectra.

### 2.3.2 Walls

For the wall treatment in a CFD simulation roughly three methods are most commonly used: wall functions, hybrid methods (LES for flow RANS for wall) and direct calculation. When using a relatively high  $y^+$  value of the first cell near the wall, both wall functions and hybrid

methods show improvement (compared to no wall treatment) in one case but give erroneous results in others. For example wall functions work good for fully developed non separated flow, and hybrid methods work best in separated flow but not so much in laminar flow. For the complex flow presented in this thesis, which involves separation, back flow, unsteadiness but also laminar flow neither methods seem fit. Therefore a direct approach is chosen. It is attempted to keep the  $y^+$  value for the first cell layer such that it is still placed in the viscous sub layer ( $y^+ < 5$ ) as is advised by Breuer et al.(2007)[8]. Others claim however that the  $y^+$  value for the first cell should be smaller than 1 to capture the boundary layer accurately[28][39]. This is computationally very expansive, however.

Also for the acoustic simulation different options exist for the treatment of the wall. The physically correct condition near a rigid wall is obtained by setting the molecular velocity at the wall to zero. To make sure the molecules do not move (normal to the wall) there cannot be a pressure gradient at the wall. Hence a zero pressure gradient normal to the wall should give the correct results (von Neumann boundary condition). In real life not all of the wave is reflected back however, part is absorbed and transmitted because the walls are not rigid and can vibrate. To take some of this into account an impedance boundary condition can be placed. Spa et al.(2009) showed that this can be achieved using the following equation.

$$\frac{\partial p(\mathbf{x}, t)}{\partial t} = -\frac{Z}{\rho} \frac{\partial p(\mathbf{x}, t)}{\partial \mathbf{n}} \quad (2.10)$$

In this equation  $p$  is the pressure,  $\rho$  the density and  $Z$  the impedance. Obviously this is very similar to equation 2.9, making the implementation straight forward.



## Chapter 3

# Acoustic validation

The purpose of this chapter is to check how the acoustic results using the Lighthill equation compare to results from literature. First, the reed instrument is discussed. This 2D model is computationally inexpensive, but can give a lot of insight nonetheless. The effect of decoupling the fluid and acoustic part of the simulation can be seen. Further the source term, that is also calculated in the reference paper, can be compared to see the accuracy of the calculation of this parameter by the for this thesis developed code. Also the resulting frequency spectrum can be compared. First the fluid flow results are discussed followed by the acoustic results. Second, the diaphragm is analysed. For this problem both a 2D and a 3D model are created. Opposed to the reed instrument this model is fully internal. This is interesting because, the upper airway models are fully internal flows as well. For the diaphragm both numerical and experimental data is available for comparison. This is used to see the accuracy of the acoustic simulation for internal flow. Also for this model first the CFD results are discussed, followed by the acoustic results. At the end of the chapter a better feeling for the accuracy of the acoustic part of the computational method should be obtained.

### 3.1 Reed instrument

For the external flow test a reed instrument, of which the layout is shown in figure 3.1, is chosen. Only one mesh is created for this model, consisting of  $2.0 \cdot 10^5$  cells, which is shown in figure A.1.

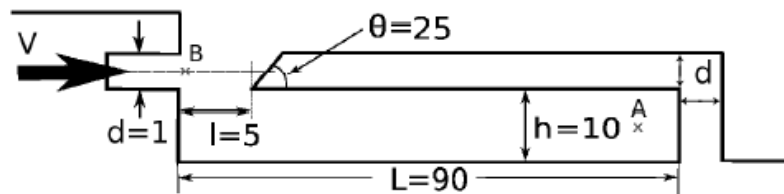


Figure 3.1: Reed model, dimensions[30]

In the reed instrument model the main flow features are seen near the inlet. A small inlet of  $1mm$  produces a jet having a velocity of  $12m/s$ . This jet hits a split, which pushes

the flow upwards. However the distance between the split and jet inlet is chosen such that an oscillating jet is produced. This oscillation creates vortexes above and below the split. These vortexes are highly correlated to the sources responsible for the acoustic waves. This model is of interest because it can be checked if the source term is implemented correctly into the computational model. Further this model allows comparison of a solution obtained by a direct approach with one using a hybrid method (Lighthill equation). Also the jet that is producing the acoustic sources streams with  $12m/s$ , this velocity could also occur in a human airway. Before the results are shown first the boundary conditions are discussed.

### 3.1.1 Boundary conditions

For the reed instrument the inlet flow can be considered uniform. Therefore an imposed flow velocity vector ( $12m/s$  in x-direction) is applied at the inlet and a von Neumann boundary condition for the pressure. At the outlet a differential pressure (normalized with the density as is default in OpenFOAM) is set to  $0Nm/kg$  (Incompressibility is assumed hence the absolute value is of no importance) and for the velocity a von Neumann boundary condition is used. For the acoustic waves at the inlet and the outlet a convective boundary condition is used as discussed in section 2.3.

At the walls the pressure and density is determined using a von Neumann boundary condition, and for the velocity a no-slip ( $u = (0\ 0\ 0)$ ) condition is applied.

### 3.1.2 CFD results

From the paper by Miyamoto, M. et al.(2010)[30] some numerical reference data is available. In this paper a direct approach is used for the calculation of the acoustics. This is done by a compressible large eddy simulation. It is claimed that the coupling between acoustic waves and jet oscillation is important, which is the reasoning for the compressible approach.

Unfortunately the figures are in black and white, also the instance shown in the figure is unknown. Nonetheless the order of magnitude of the different parameters and the overall similarity can be checked.

In figure 3.2 the velocity field is plotted. It seems that the activity in the resonator is a little bit lower than for the reference simulation. This is not always the case, the oscillation frequency and amplitude is not fully steady; therefore the amount and size of the vortexes that are seen above and below the split changes somewhat in time. It is also noted in the paper that higher velocities lead to better resonance. Looking more general at the results for the velocity the simulations look quite similar (only one snapshot is shown).

In figure 3.3 the vorticity is shown. The magnitude up close and further away seem of the right order. Also the size of the vortexes seems to be in the same range. Notice how close the vorticity is related to the the source term, shown in figure 3.4. Also the source term seem be calculated correctly. The source term will in turn be responsible for the changes in density as follows from the Lighthill equation 2.6. In the reference paper the Lighthill equation is only used to show the sources, the propagation is not calculated using this equation. It is claimed that the coupling between acoustics and mean flow is too important for this case to separate. Therefore a compressible LES was run instead, which takes into account this coupling. The two resulting density fields are shown in figure 3.5. First note the different scales on the legend. Using the Lighthill equation only the perturbed acoustic field can be calculated, not the mean values. However, just to see how it compares the range (difference between

maximum and minimum) is set the same and shifted such that the picture looked close to the reference figure. There are similarities but the range does not allow good comparison.

Further, one can see some high frequency waves in the reference value figure. Knowing the dimensions of the figure these waves should have a frequency of approximately  $113kHz$ . It is unknown where this frequency comes from and it is not seen in the right figure. It is not explained or noted in the paper[30]. Looking at the more global picture (figure 3.6), there are some waves that can be seen.

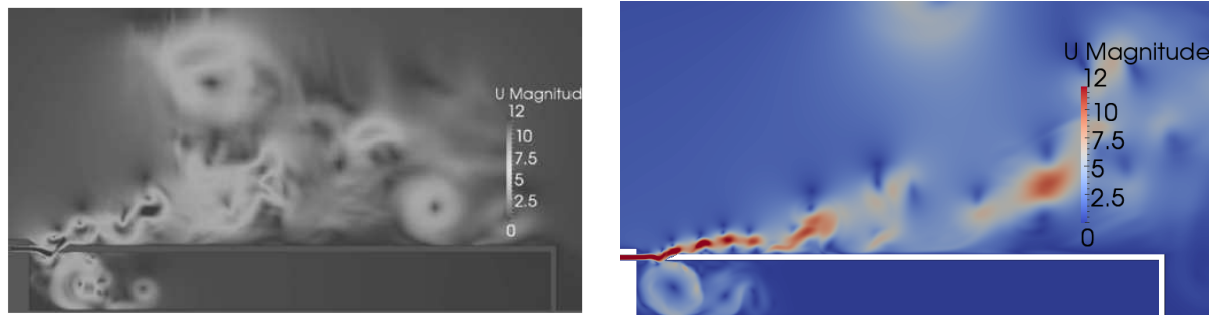


**Figure 3.2:** Reed velocity field[m/s], reference[30](left) and thesis research(right)

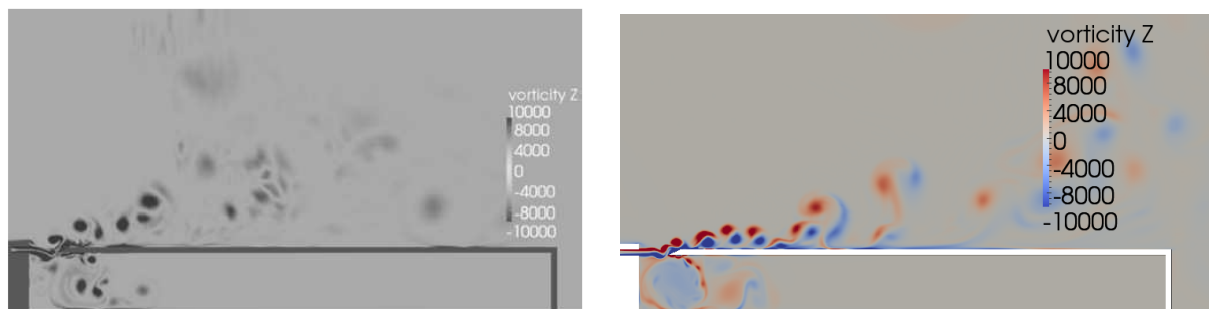


**Figure 3.3:** Reed vorticity field[ $s^{-1}$ ], reference[30](left) and thesis research(right)

### 3.1.3 Acoustic analysis

The system of resonator, jet and split is studied by multiple scientists. Empirical relations exist to estimate the frequencies that dominate the sound spectrum. In Miyamoto, M. et al.(2010)[30] the same configuration is used as in this thesis. They claim that a representative value for the first fundamental frequency of the *resonator* is  $913.1$  and for the third  $2739.3Hz$ .

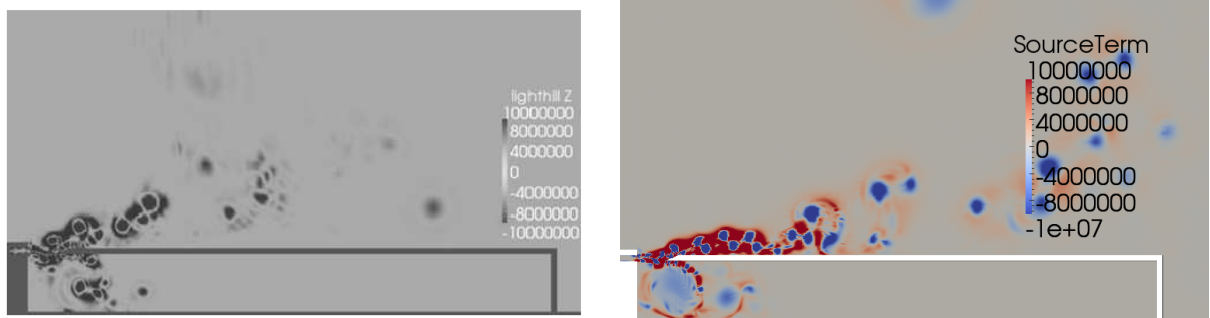


Figure 3.4: Reed source term field[ $kg/m^3/s^2$ ], reference[30](left) and thesis research(right)

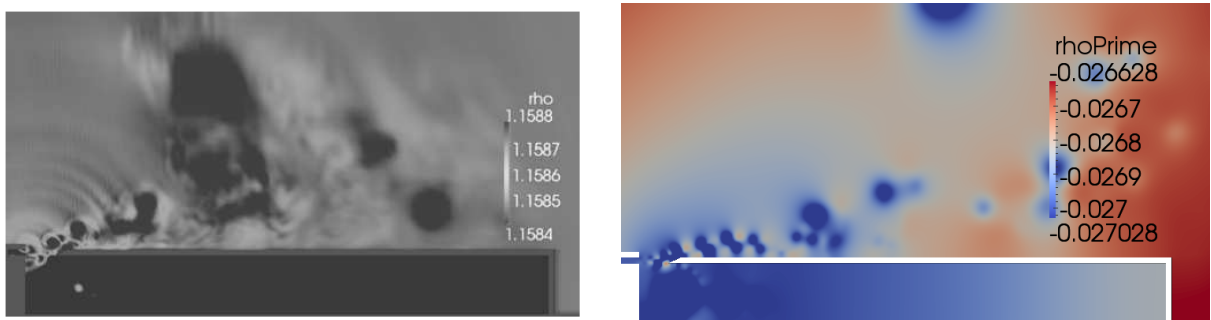


Figure 3.5: Reed density field[ $kg/m^3$ ], reference[30](left) and thesis research(right)

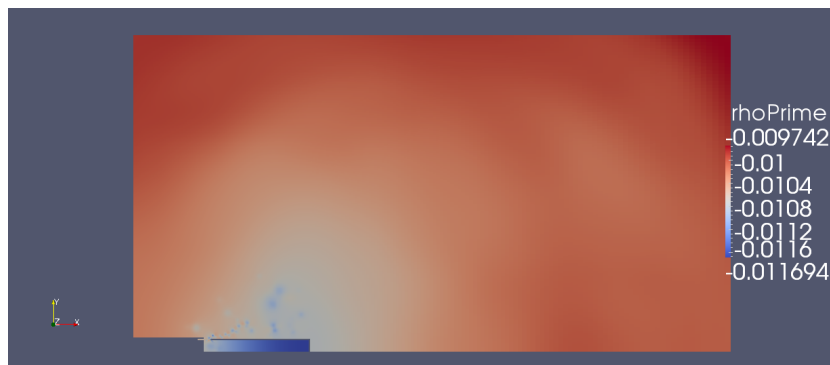


Figure 3.6: Reed, density field[ $kg/m^3$ ]. Overall look of the density field with the axis scaled properly

An empirical formula shown in this same paper that originates from Brown, G.M. (1937), that predicts the frequency of the edge tone reads

$$\nu = 0.466j(100V - 40)(1/(100l) - 0.07), \quad (3.1)$$

where  $V(= 12)$  denotes the speed of the jet and  $l(= 0.005m)$  is the distance between the flue and the edge. The number  $j$  is taken as  $j = 1.0, 2.3, 3.8, 5.4$ . For  $j = 1$  it gives the fundamental frequency and others denote overtones. Filling in the values of this simulation yields 1043.28Hz, 2399.55Hz and 3964.47Hz for the first three fundamental frequencies. These values are only for the combination flue-edge and do not incorporate the effect of a resonator. The earlier mentioned values for the *resonator* fundamental frequencies are obtained from  $\omega = c(n + 1/2)\pi/L$  where  $n$  is an integer. However an open end correction is applied to give the 913.1 Hz and 2739.3 Hz. The authors show that the frequency follows relation 3.1 but lock on the fundamental pipe frequencies. This can only be captured when the acoustic and fluid equations are coupled.

In figure 3.7 the raw output for the density near the end of the pipe is shown (near point A in figure 3.1). One notices immediately that the value is decreasing steadily. Integrating the source field over the computational domain gives a negative value. Hence netto the source field acts as a sink for the density, causing the decrease in value. Probably due to the missing coupling between the acoustic and fluid flow simulation there is no mechanism to keep the density from decreasing. Using a moving average still a 'normal' sound wave plot can be created. This is also shown in figure 3.7. Notice the signal is transformed to pressure, this is done using the equation,

$$p' = \rho' c^2 \quad (3.2)$$

which is given in a thesis by Escobar, M.(2007)[13]. This equation holds if linear acoustic propagation and isentropy can be assumed. Looking at the right part of the figure one can see that amplitudes of 100Pa are achieved. This is the same order of magnitude as is seen in the reference paper.

A Fourier analysis can be applied and compared to the reference data. This is shown in figure 3.8. The figure shows the numerical reference data extracted from the paper and is displayed, using Photoshop, over the results from this thesis. The overall sound pressure is of the same level. Note that the intensity is not normalized with  $10^{-12}$ , the lowest humanly perceivable sound intensity, as is common in acoustics. Although the peak at  $2.4kHz$  corresponds nicely the third peak is not present at the reference data and the first peak is at a slightly different frequency. Looking at the fundamental frequencies as calculated with equation 3.1(1043.28Hz, 2399.55Hz and 3964.47Hz), however, the values calculated with the Lighthill equation are very close. Only the third value seems to be off. This value looks more to be 3700Hz. The difference with the reference data is most likely because of the decoupling of the fluid and acoustic part of the simulation.

## 3.2 Diaphragm

The results for the reed instrument show that most features that are expected from the acoustic signal can be found. The reed instrument problem, however, is an external flow

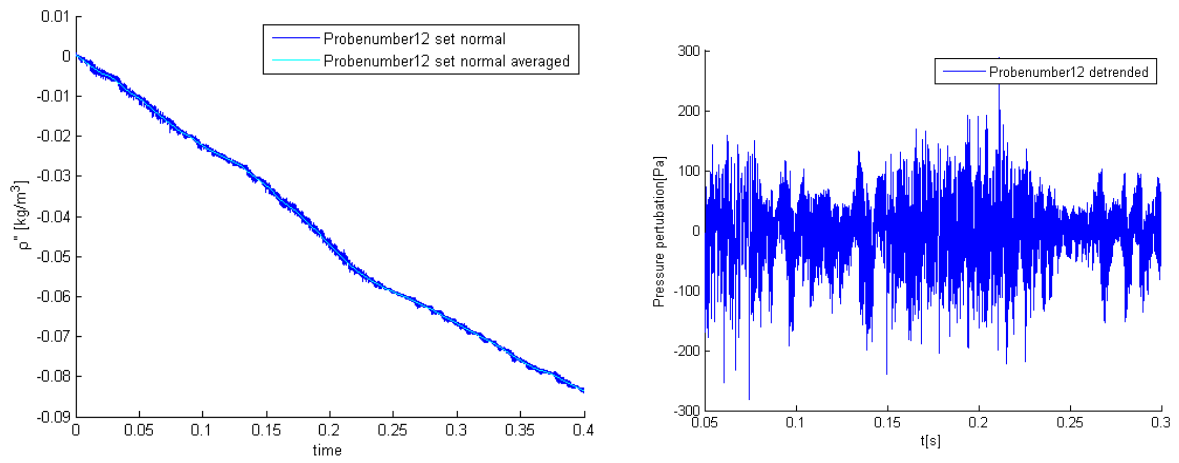


Figure 3.7: Reed, acoustic point data: left raw density output, right detrended converted output

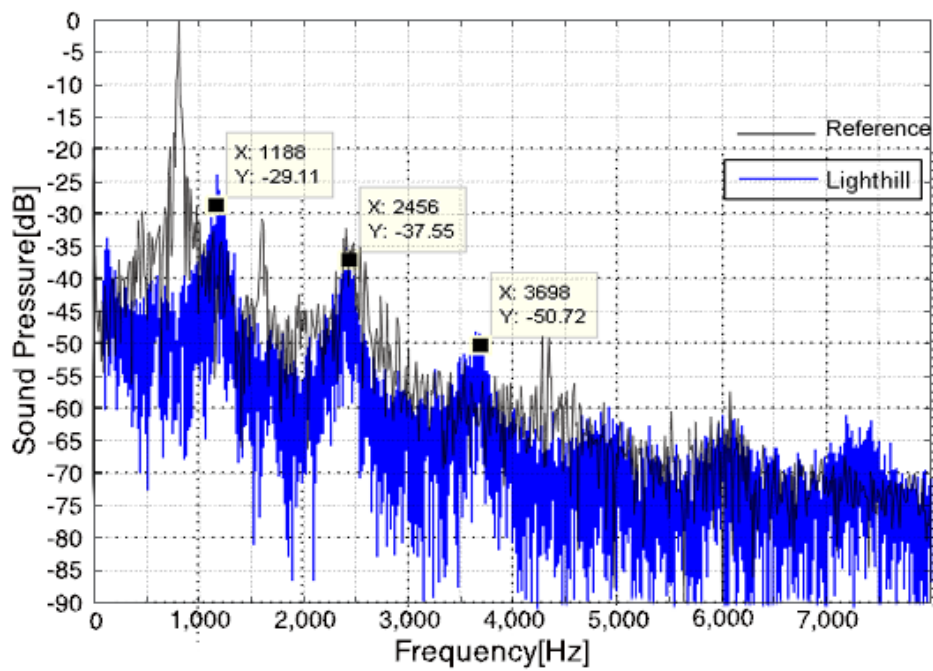
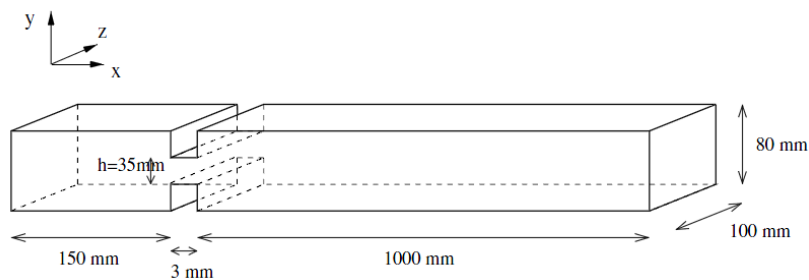


Figure 3.8: Reed, sound pressure[30]

problem whereas the final model to be analysed is an internal flow. For internal flow the acoustic waves are more restricted and have a harder time leaving the domain, because in general only at the inlet and outlet the waves are allowed exit. The waves reflect on the walls, giving rise to complex acoustic field. Therefore a validation for internal flow acoustics is value adding to the research and can give more insight in the accuracy of the final results of the thesis. Two reference sources are available: a paper by Gloerfelt, X. and Lafon, P. (2007)[15] and a paper by Bailly, C. et al.(1996) [4]. The first paper covers an LES calculation using a direct approach for the noise created by a diaphragm at  $6m/s$ . The second paper also covers a noise calculation (albeit using a different approach), however the most interesting part is that experimental data is given for a diaphragm at  $14m/s$ .

### 3.2.1 The geometry

A 2D model and a 3D model are created. The 2D model is mainly used to test different boundary conditions and gives a quick insight into both the flow and acoustic properties of the model. However the 2D model does not take specific properties into account such as: the out-of-plane fluctuations and spherical spreading of acoustic waves. Both of these effects alter the results. Hence it is expected that the 3D version gives better results. See figure 3.9 for the dimensions of the reference model. The 2D model and 3D fine model are both smaller (length behind diaphragm is 600mm). For the 3D coarse meshed model the correct dimensions are used, but an extra part is meshed at the end of the model to see its effect of acoustic wave outflow. This extra part, and the mesh density, can be viewed in appendix figures A.2 & A.3. The coarse mesh has an element count of  $2.48 \cdot 10^6$  and the dense mesh an element count of  $3.51 \cdot 10^6$  (while also being shorter, resolution is approximately increased twice in each direction). The simulation in the reference paper used  $4.01 \cdot 10^6$  cells, especially out-of-plane more elements are used compared to the coarse mesh. Near the boundary layer fewer elements are used however ( $\Delta y_{ref} = 0.6$  and  $\Delta y_{the\ coarse} < 0.1$ ). Further it is interesting to note that the order of the scheme used in the reference paper is higher (10 point finit difference scheme, and a runge kutta method is used for the temporal discretization).



**Figure 3.9:** Diaphragm 3D Model, dimensions[15]

### 3.2.2 Boundary conditions

For the diaphragm the same type of boundary conditions are used as for the reed instrument, for convenience it is repeated here. The inlet flow can be considered to be more uniform

then the outlet. Therefore an imposed flow velocity vector ( $6m/s$  and  $14m/s$  in x-direction) is applied at the inlet. At the outlet the differential pressure is set to  $0Nm/kg$  and for the velocity a von Neumann boundary condition is used. For the acoustic waves at the inlet and the outlet a convective boundary condition is used as discussed in section 2.3.

At the walls the pressure and density are determined using a von Neumann boundary condition, and for the velocity a no-slip (Dirichlet) condition was applied.

### 3.2.3 CFD results

The diaphragm flow shows interesting behaviour. The flow is not symmetrical even though the geometry is, which is at first a bit counter intuitive. However this flow structure, where the jet is attached to the wall on one side and back flow is seen on the other side, is more stable than a symmetric jet flow. In figure 3.10 a snapshot of the instantaneous velocity profile of different simulations is shown. The top figure is calculated using the most dense mesh, the middle simulation is from the coarse mesh and the bottom part is taken from a reference paper[15]. Note that all figures show that the jet attaches to the upper wall. In the numerical case it is more or less random whether the flow attaches to the upper or bottom wall (influenced by for example numerical errors and mesh asymmetry). The figures are rotated such that the flow is attached to the upper wall for easy comparison. In a real flow gravity, surface quality (symmetry, smoothness, dirt etc) and inflow condition (e.g. disturbances from wind tunnel) influence the attachment point. These effects do not play a role in the numerical model, however.

The attachment point seems to be the same for the two coarse meshed models. The jet in the middle figure seems to be mixed into a uniform flow a little bit sooner than for the reference figure. The fine mesh clearly shows more structures. The jet attaches a bit sooner on the wall. After this the flow separates again and reattaches to the bottom wall. The separation and reattachment points are however not fully steady. The double wall attachment structure is not shown in the reference paper. This might be because of the improved wall treatment (resolution is much higher) or because the domain is slightly shorter for the finest mesh (600 mm after diaphragm opposed to 1000 mm).

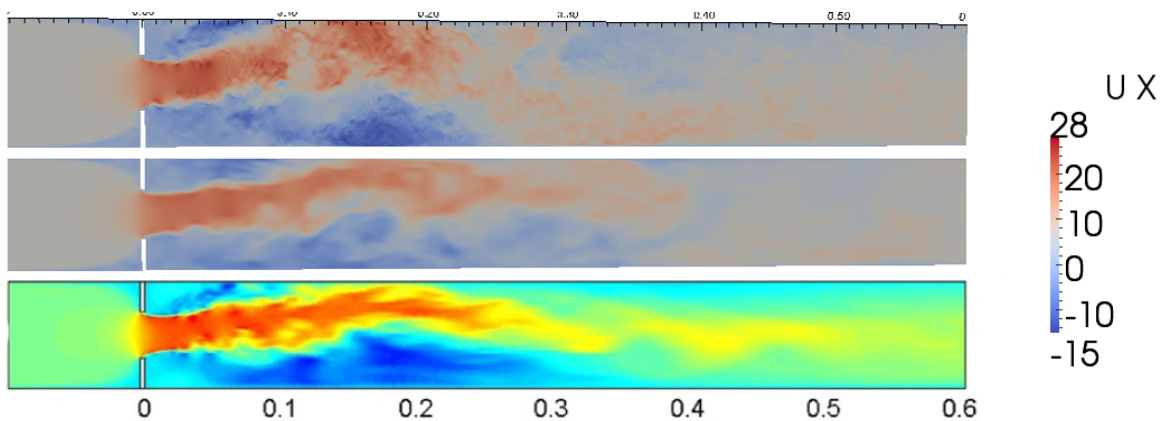


**Figure 3.10:** Diaphragm 3D Model  $V = 6m/s$ , Velocity field: Top fine, middle coarse, bottom from[15]

In figure 3.11 the vorticity field is shown. Here the difference in mesh density is seen relatively

pronounced. The overall features are still very comparable, however. For example the point at which the centre of the jet begins to show vorticity is close to each other. Also the decrease of the vorticity further downstream seems to be at the same rate. Also the resemblance with the reference simulation is good. Since the vorticity is closely related to the sound production this gives a hint that the sources are probably of the same strength as would be the case for the reference paper, if they had reported such thing. The source term is not available from the reference, but the coarse and dens mesh can be compared. This is shown in figure 3.12

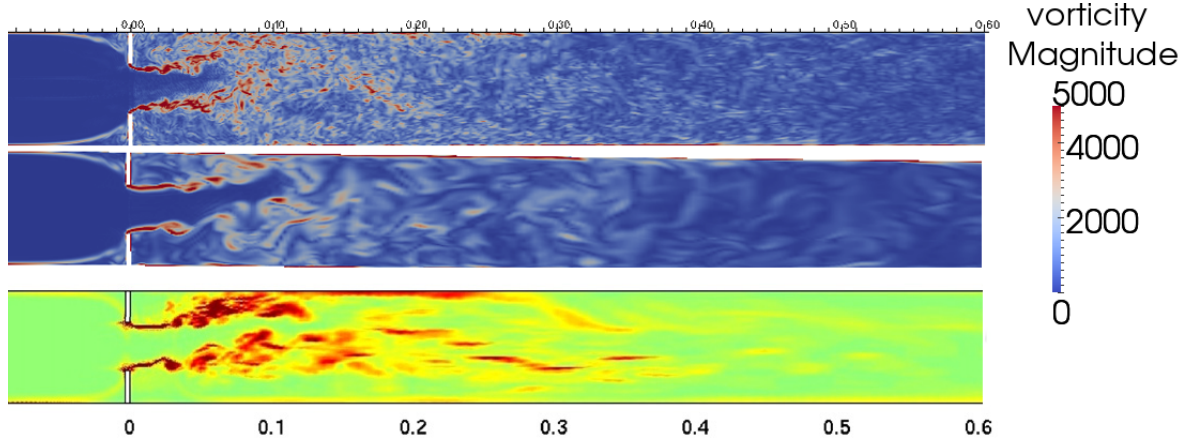


**Figure 3.11:** Diaphragm 3D Model  $V = 6\text{m/s}$ , Vorticity (magnitude) field: Top fine, middle coarse, bottom from[15]

The order of magnitude of the acoustic sources in the higher density simulation is slightly higher in than the coarse meshed model solution. It looks like the coarse mesh has a more averaged distribution compared to the fine mesh solution; the very fine structures are blurred. After 300 mm most sources seem to be gone. Hence most of the sound production is close behind the diaphragm. When looking at the first sources after the diaphragm the distance between source peaks and valleys are approximately the same near the diaphragm.

In figure 3.13 the results for the simulation with an inlet velocity of 14 m/s are shown. Look-

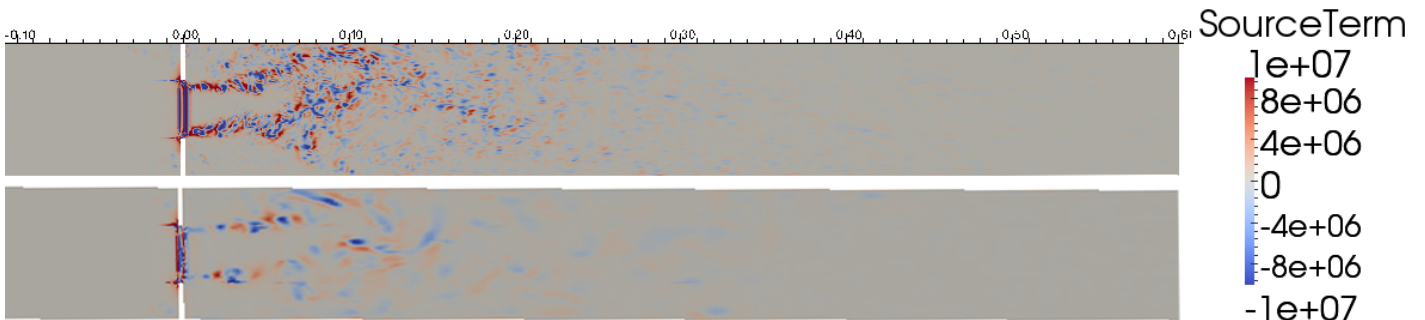


**Figure 3.12:** Diaphragm 3D Model  $V = 6\text{m/s}$ , Source term field: Top fine, bottom coarse

ing at the velocity the jet clearly has a much larger velocity. Because of this the attachment point at the wall is also slightly further downstream compared to the 6 m/s case. The overall

difference in flow structure is however not so different from the other case. Also the vorticity and source terms show similar behaviour, although both have an increased value (see legend).

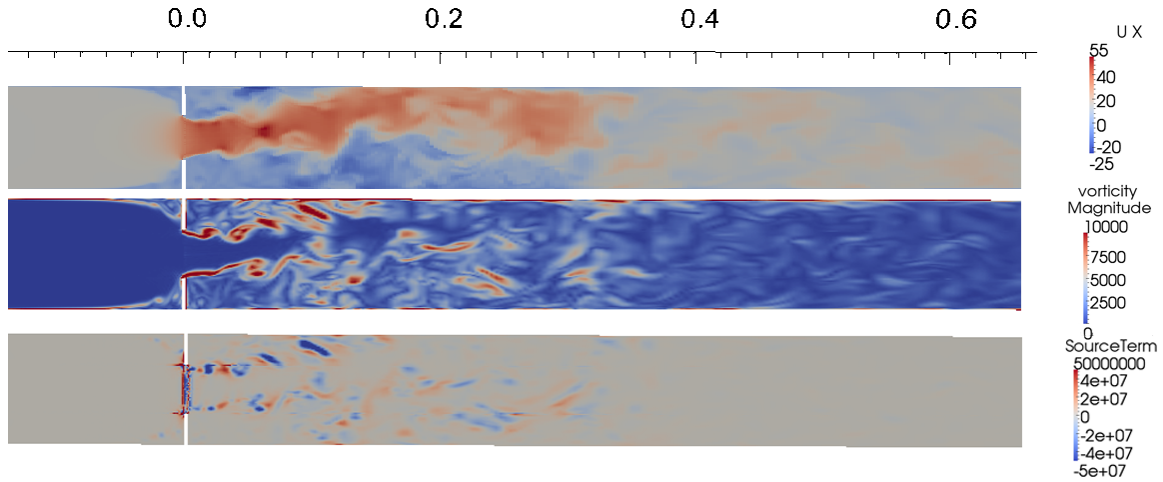


**Figure 3.13:** Diaphragm 3D Model  $V = 14m/s$ , Top velocity field, middle vorticity (magnitude) field, bottom source term field

Finally in figure 3.14 the results for a 2D calculation are shown. The 2D case shows a distinct difference with the other figures. Probably due to reduction of mixing in a 2D case the jet can 'survive' much longer. When looking in the next section it can be seen that the acoustic signal is, however, representative for the geometry. Further the model is tested for different wall boundary conditions for the acoustics as is also discussed in the next section. Further the sponge layer, convective outlet boundary conditions and different combinations of in and outlet flow boundary conditions are tested on the model. This finally resulted in the boundary conditions discussed in section 3.2.2. These tests are performed on the 2D model because of the significantly shorter run times for a two dimensional model compared to a three dimensional model.

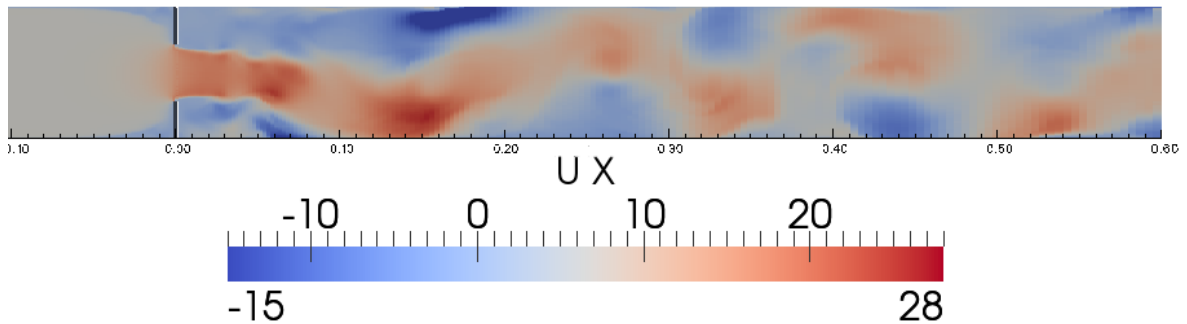


**Figure 3.14:** Diaphragm 2D Model  $V = 6m/s$ , velocity field

### 3.2.4 Acoustic results

In figure 3.15 the raw signal from the 3D coarse mesh simulation is plotted for probe number 22 (placed near the outlet at coordinate (0.95,0,0) in meters). Using a moving average (signals below 100Hz are filtered, and the line is detrended) the fluctuating signal is retrieved by subtraction. Also the resulting pressure fluctuations are shown. Note that the start up of the simulation is clipped.

Using the latter signal the sound spectrum can be calculated. In the paper by Gloerfelt, X. and Lafon, P. (2007)[15] a direct approach was attempted to calculate the noise generated by the duct. The results from this paper are extracted (by reading out one of their diagrams), and plotted with results using the Lighthill equation. The overall and a zoomed spectrum are shown in figure 3.16, using the clipped fluctuating signal as presented right in figure 3.15. Between 400 Hz and 800 Hz the spectrum overlaps nicely. Outside these frequencies differences are seen. The lower frequencies seems to be over predicted compared to the reference paper. For the other values it seems the trend is good but the absolute value a bit off. Looking back at the source terms plotted in the previous section it could be the case that the larger structure are not broken up in smaller sources giving more energy to the higher frequencies. Unfortunately no acoustic data is available for the fine mesh, hence this cannot be confirmed.

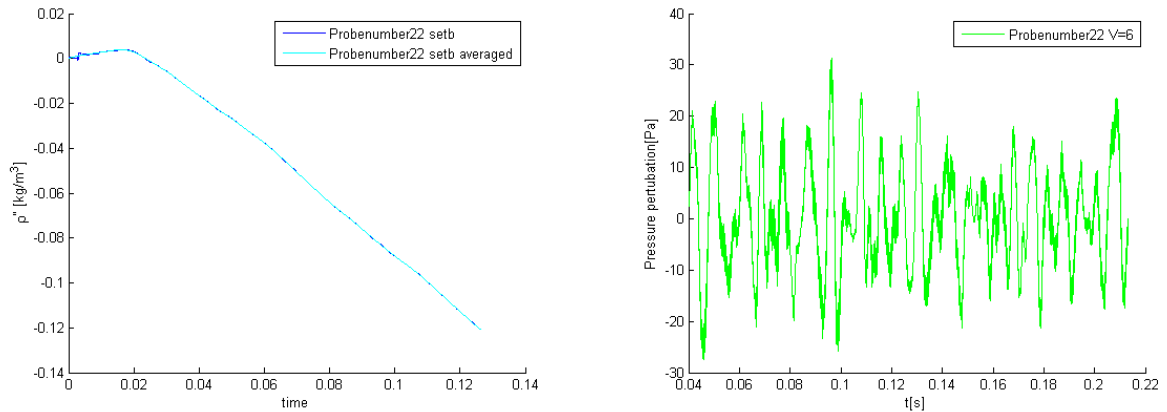


**Figure 3.15:** Diaphragm coarse 3D Model  $V = 6m/s$ , left raw density signal and right resulting pressure perturbations

Next the acoustic data resulting from the higher inlet velocity are discussed. For this set up experimental data is available from the paper by Bailly et al.(1996)[4]. The data is read out and plotted with the results from the Lighthill equation. In figure 3.17 the raw output signal and the resulting pressure perturbation are plotted. A similar signal as for the previous case is obtained. Notice how the pressure perturbations have increased in magnitude, however. Using this signal the acoustic intensity distribution can be plotted, which is shown in figure

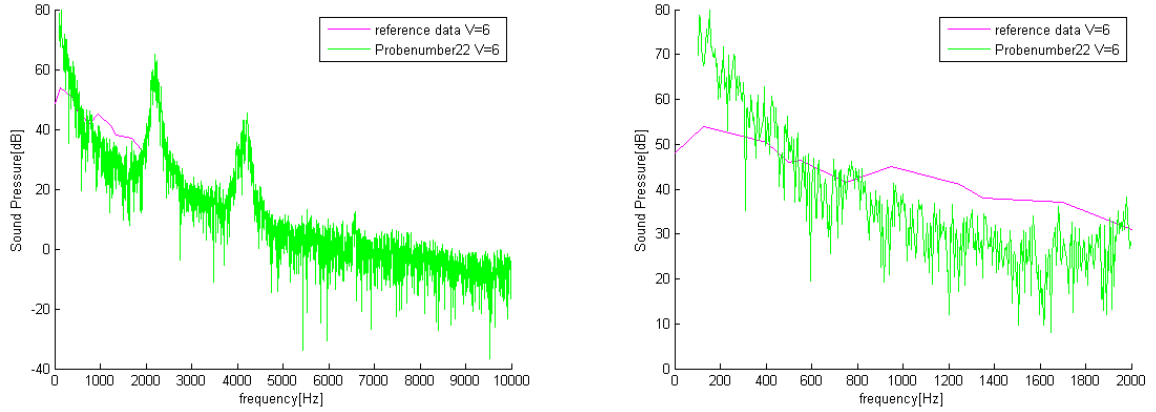


**Figure 3.16:** Diaphragm coarse 3D Model  $V = 6m/s$ , left overall sound pressure and right zoomed sound pressure

3.18. Again the lower frequencies are slightly over predicted but the general trend is to be good. The results are a lot closer than for the previous simulation.

It has been experimentally verified that there exists a  $U^4$  law[15]. From this law it is possible to calculate how much decibel the total radiated sound pressure should increase for a specific increase in velocity. This is given by,

$$\log(P_{6m/s}) - \log(P_{14m/s}) = 4 \log(6/14), \text{ thus} \quad (3.3)$$

$$10 \log(P_{6m/s}) = 10 \log(P_{14m/s}) + 40 \log(6/14) = 10 \log(P_{14m/s}) - 14.7. \quad (3.4)$$

Using this, the two plots can be merged and compared. In figure 3.19 the original and shifted spectra are plotted. The law should be used for the total radiated power, not the distribution. Nonetheless the resemblance is very good; also at the lower frequency part. This is a good result, and gives more confidence in the results for the first simulation. Notice that both simulations show two peaks in the spectra. Looking at the geometry: the probe is placed in the middle thus an up and down bouncing wave would pass it every half and whole period. There are two opposing walls one having length 0.1m and one 0.08m, because of the nature of the flow most flow perturbations are in the xy-plane though. Using these values one can calculate the following frequencies: for the top and bottom wall the frequency of a whole period amounts to  $346.15/0.16 = 2164\text{Hz}$  which is close to the first top of  $\pm 2200\text{Hz}$  and for the half period  $346.15/0.08 = 4327\text{Hz}$  which is close to the last top  $\pm 4200\text{Hz}$ , and using the other walls no frequencies are calculated that can be seen back in the spectrum.

Finally in figure 3.20 the acoustic spectrum for the 2D case is shown. In this figure the zero gradient boundary condition calculation is shown together with an impedance boundary

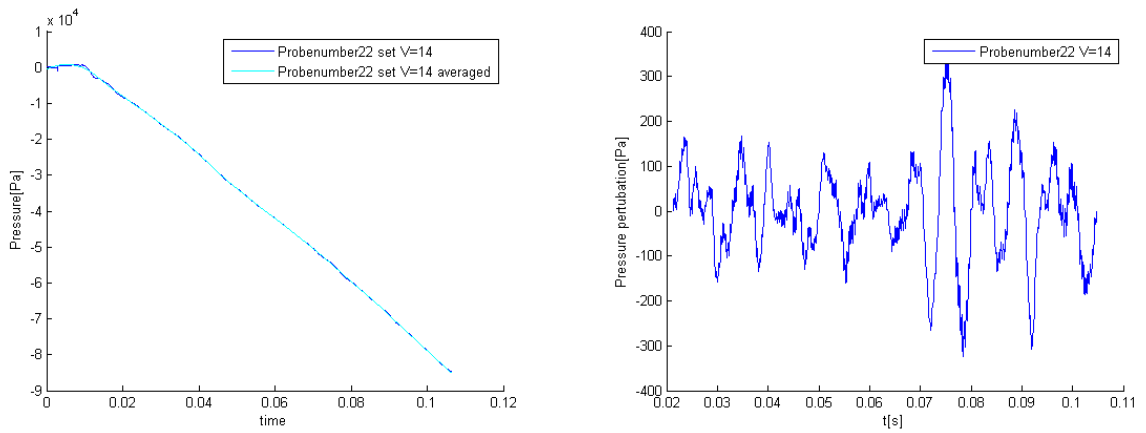


Figure 3.17: Diaphragm coarse 3D Model  $V = 14m/s$ , left raw density signal and right resulting pressure perturbations

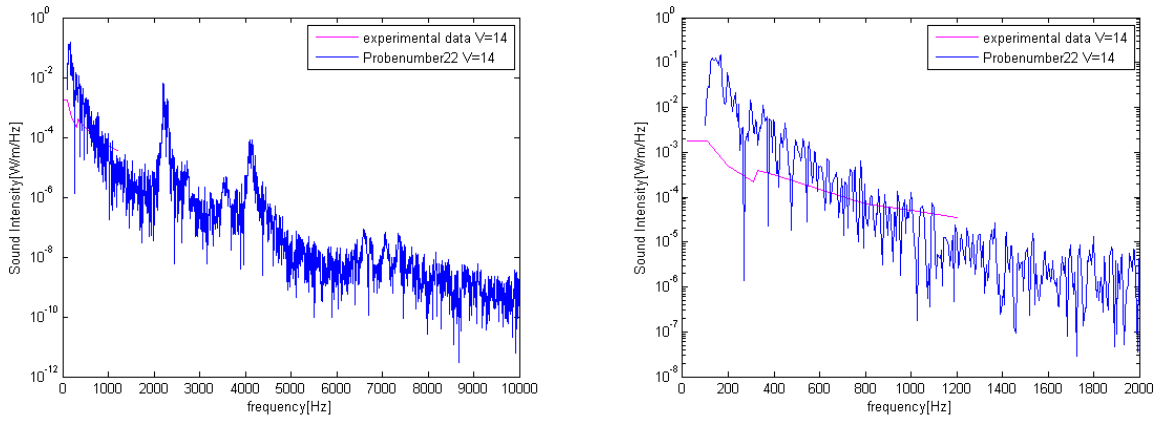


Figure 3.18: Diaphragm coarse 3D Model  $V = 14m/s$ , left overall sound intensity distribution and right zoomed sound intensity

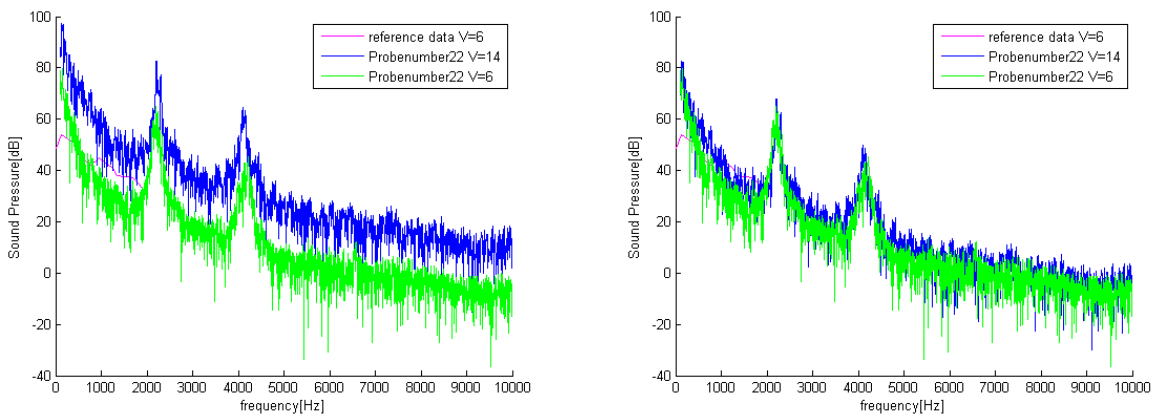
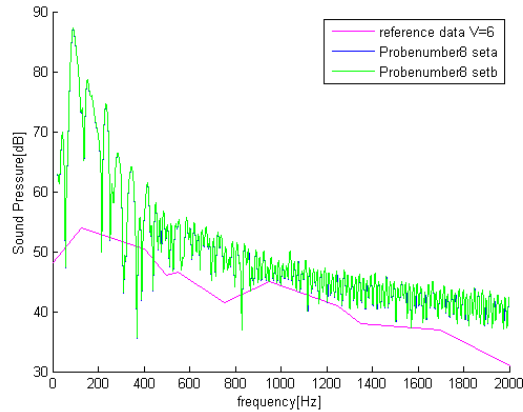


Figure 3.19: Diaphragm coarse 3D Model  $V = 6m/s$  and  $V = 14m/s$ , left unaltered sound pressure distribution and right shifted sound pressure distribution

condition. This second boundary condition allows a small part of the signal to be transmitted through the wall. Using the impedance values for human tissue it can be seen that this type of boundary condition hardly affects the results (a difference of approximately 0.5dB). For a smaller geometry the difference might become bigger since more reflections are present, however the use of an impedance boundary condition seems limited. Vibration of tissue will probably yield more significant changes in acoustic behaviour. The signal itself seems to be representative, comparing with the reference data. However the strong jet behaviour near the outlet causes a lot of noise, so only a short period of time can be used for the acoustic analysis.



**Figure 3.20:** Diaphragm 2D Model  $V = 6\text{m/s}$ , Sound pressure: set a: impedance boundary condition, set b: zero gradient boundary condition

### 3.3 Conclusion

In this chapter the acoustic performance of the computational code developed for the thesis is checked on two models. This is the reed instrument for external flow and a diaphragm model for internal flow. Using both numerical and experimental reference data it is shown that the magnitude of the predicted signal is close to the reference data.

For the reed instrument some resonant peaks are predicted when using the Lighthill equation. It is possible to give a physical interpretation of these peaks. However deviation from the reference numerical simulation is seen. Although the flow properties are very comparable, in the acoustic data some differences can be seen. These are due to the missing coupling of the fluid and acoustic simulation. Further a drift in the raw signal of the density is seen which can be explained by the uneven distribution of positive and negative acoustic sources. Using a moving average the resulting signal can be processed to give good results.

Also for the diaphragm the correct decibel levels are predicted. Also the power distribution over the different frequencies is close to what is expected. The lower frequencies seem to be slightly over predicted. Scaling the results using the  $U^4$  law shows that the increase in sound level is predicted correctly. Further it is seen that an impedance boundary condition does not alter the results much. And gives only marginal differences compared to a zero gradient boundary condition.

From all previous results it can be concluded that satisfactory accuracy can be obtained using the Lighthill equation. The overall levels are predicted good and also the frequency peaks and distribution are close to what is expected.



## Chapter 4

# Analysis of a simplified upper airway model

In this chapter the analysis of the results of the simplified upper airway model(SUAM) are discussed. This model is used to get a better feeling for the mesh density that is required to get accurate results before progressing to the final problem. The model is a good first step since it is derived from real airway geometries and shows the same type of flow structures that are encountered in a real airway. The original simplified upper airway model was courtesy of by Chris Lacor (Vrije Universiteit Brussel) and is discussed in the paper by Jayajaju, S. et al.(2008)[20].

Further it is checked whether the implemented selective LES model is able to capture the transitional behaviour of the flow that is characteristic for upper airway geometries as was discussed in section 1.2. The validation is possible because a particle image velocimety (PIV) experiment from the paper by Brouns, M et al.(2006)[9] is available as a reference result.

Besides giving insight in the validity of the CFD methods that are used, the model can also be used to investigate the effects of a constriction on the flow and the acoustic behaviour. Because of the simplicity the model allows for relatively easy adaptation as is seen in the section covering the geometry. The boundary conditions, which are slightly different than for the previous cases, are discussed next. This is followed by the validation of the LES-model. Finally the results of the different models are shown, both the CFD and the acoustics are discussed.

### 4.1 The geometry

From the original SUAM multiple versions are derived; different constrictions are placed to investigate the effect on noise production, secondly different levels of mesh density are used to investigate the appropriate mesh resolution.

The dimensions for the original model are shown in figure 4.1. The air flows in at the top of the model through the inlet which transitions to the oral cavity. From here the flow needs to bent 180° ending in the nasopharynx(B-B). Next a sharp edge can be seen (near C-C), this is where the epiglottis would be in a real human airway. Further downwards the area reduces as the air flows through the glottis(G-G), and widens again when transitioning to the trachea(H-H).

The constrictions are 50% and 75% of the tracheal area which can be viewed in figure A.4. The reason for these values are medical; starting from  $\pm 50\%$  constriction of the trachea stridor can be diagnosed and the upper limit of constriction is approximately 75%. In this latter case the patient will have severe problems breathing and medical procedures are necessary in general. The circular constrictions are medically possible (this type of constriction can for example be caused by scar tissue), and is placed just below where the vocal cords would be. These constrictions are placed to see how these effect both the flow and sound production. More specifically, it is investigated if it is possible to see the difference in sound production for the different constrictions, and if soundwaves generated by the sources are convected such that their influence can be seen near the inlet.

To test the effect of the LES subgrid scale model, a coarse meshed upper airway model is used. As the cell size decreases the SGS model becomes less important, hence the effect of the subgrid scale model is best tested on the coarse model.

A total of three meshes is tested: the most coarse mesh for the LES SGS model, a fine mesh for the acoustic analysis and a super fine mesh as a reference solution. The meshes are found in figure A.5 (coarse  $8.89 \cdot 10^5$ , fine  $2.52 \cdot 10^6$  and super fine  $4.59 \cdot 10^6$ ). For the different constrictions the mesh density is distributed the same for each model (for the 0%, 50% and 75% cases).

## 4.2 The boundary conditions

For the airway models the problem is slightly different then for the diaphragm flow. Here the inflow is not necessarily uniform whereas the outflow *is* (more or less). Therefore compared to the previous case the inlet and outlet boundary conditions are switched (thus the flow speed is imposed on the outlet instead of the inlet). Another possibility would have been to use a pressure-pressure boundary condition. However since the required pressure difference to acquire a given mass flow is not known beforehand, this set up would require iterations; this is very inconvenient.

At the inlet the differential (density normalized) pressure is set uniform to  $0Nm/kg$  and the velocity inlet is determined automatically by the pressure difference. This allows a non-uniform inflow which is beneficial. Namely, for the reference model used to acquire the PIV data an already developed channel flow is present at the inlet. The non-uniform inflow might result in a better developed inflow of air, possibly yielding better results further downstream.

At the outlet the pressure has a zero gradient condition and the velocity is imposed such that the correct mass flow is achieved. Since for the SUAM experimental data is available, where a flow rate of  $30L/min$  is used, a similar boundary condition is implemented.

Also for the SUAM reflection caused by the pressure boundary conditions could be a concern. However both the inlet and the outlet conditions are relatively steady, this reduces the effects of reflected pressure waves. For the acoustic waves again a convective outflow is used. Also on a piece of the wall near the inlet a convective outflow boundary condition is used for the density waves. This allows waves that are orthogonal to the inlet also to leave the domain more freely. Furthermore near the inlet and outlet the source term is set to zero to reduce numerical noise caused by the the boundary conditions that are in place near this area.

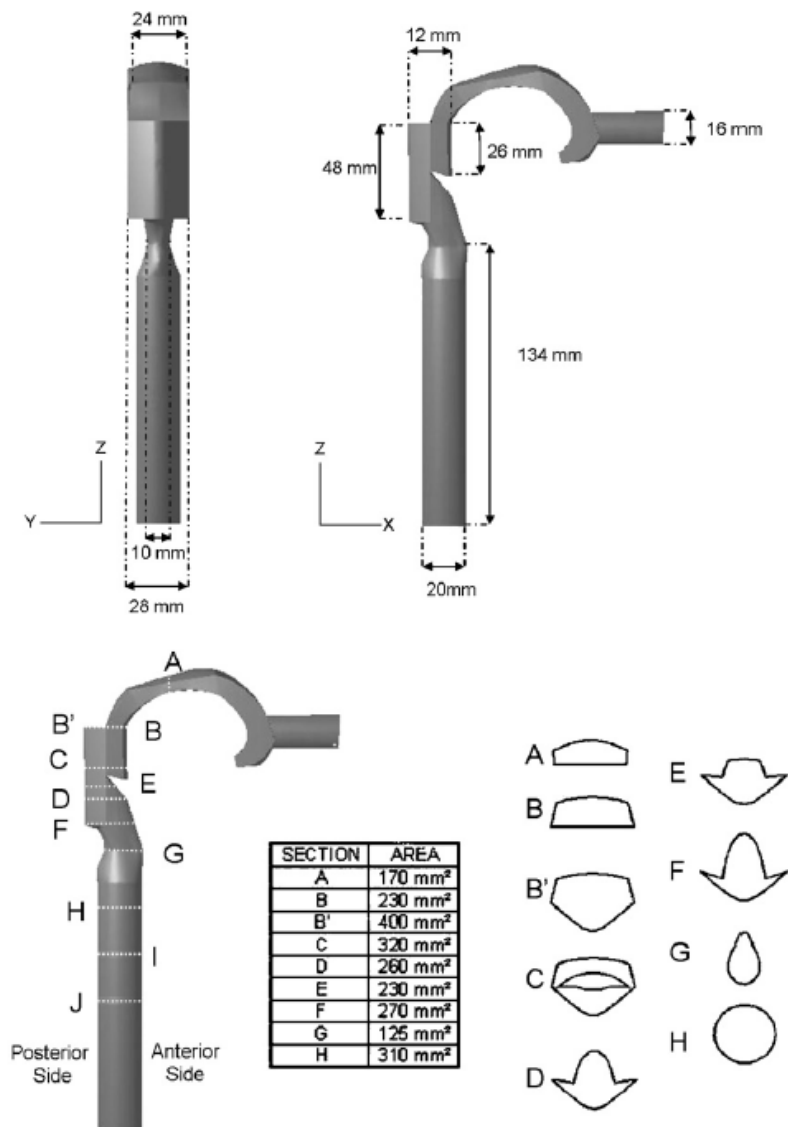


Figure 4.1: SUAM dimensions[20]

### 4.3 Comparing LES models

After comparing different papers during a literature study[26] it was found that many different subgrid scale model exist for LES. Although many papers are published concerning this subject it was difficult to find the absolute best SGS model. Also when restricting oneself to the problem at hand, the simulation of an upper airway model, still different options exist. However during the search the concept of selective SGS models came back several times. It is mentioned in for example [28] and [35] that these models give good behaviour near walls and for transitional flows. Since these are two important properties seen in upper airway models this model is chosen.

In total three different models are tested on the original upper airway model. The (normal) Smagorinsky and  $k$ -equation SGS model are tested, which are implemented by default in OpenFOAM, and the selective Smagorinsky SGS model is tested, which is implemented by adapting the original Smagorinsky model with a selection function. The selection function is described in section 2.1.

Since the aspects of the flow itself are covered in the next section only the numerical values will be shown here. In figure 4.2 different line plots are shown. The height of the cross sections is shown in in figure 4.1. Note that this figure is extracted from the reference paper[20] and is superimposed on the MATLAB plots from the results of the coarse model simulations. Note that the simulation used a mesh with  $8.89 \cdot 10^5$  cells, which is 3 times less compared to the reference paper's finest mesh. Still reasonable accuracy is obtained. The normal Smagorinsky model performs the worst. The one equation ( $k$ -equation eddy viscosity) model performs better. And the selective Smagorinsky seems to perform best. Clearly the selection function is a great improvement on the normal Smagorinsky model for this type of flow. However for an increasingly dens mesh the subgrid scale model becomes decreasingly important. A drawback of the selective Smagorinsky model is that the creation of the selection field takes extra time. Nonetheless also for the final mesh the selective Smagorinsky model is used since it showed good results for the simplified upper airway model.

### 4.4 Fluid flow validation

The fluid flow analysis is done using the finest mesh. Afterwards a comparison is made with the (somewhat) coarser mesh which is used for the acoustic analysis and with PIV data. This should give some insight in the accuracy of the source term that is used for the solution of the density wave equation.

To gain some insight into the flow, streamlines are plotted in figure 4.3. These are the streamlines for the original model. The flow enters the model smoothly from the inlet into a volume of increased cross sectional area. This creates some vortexes which are clearly seen in the top view. Also just below the inlet there is a spot where the flow keeps recirculating. A bit further the flow needs to bend  $180^\circ$ , and still is does not show smooth streamlines before hitting the epiglottis (the sharp edge). Next the flow is accelerated when going through the glottis (the part with the smaller cross section), which smoothens the streamlines a bit. Below the glottis the flow attaches to the right wall. On the other side of the wall back flow is seen in one big recirculation zone. Further downward the flow becomes more steady as it nears the outlet.

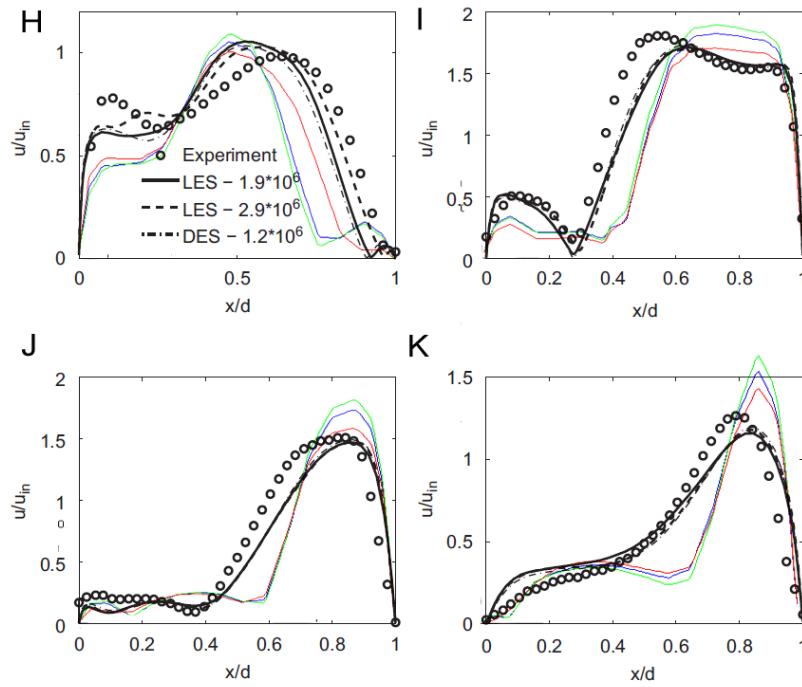


**Figure 4.2:** Lineplots  $(U_x^2 + U_z^2)^{0.5}/U_{in}[-]$ , Letters indicate cross sections in figure 4.1, —*One Equation model*, —*Smagorinsky* and —*Selective Smagorinsky*. Reference[20]



**Figure 4.3:** Simplified upper airway model, streamlines: side view upper part(left), side view bottom part(middle) and top view(right)

Next see figure 4.4. Here the streamlines for the different levels of constrictions are put next to each other to see the influence of the constriction on the flow behaviour. It can be seen that the jet that originally attaches to the right wall (due to the momentum gained upstream), is now forced to stream more to the middle of the trachea because of the constriction. For the 50% case this means that surrounding the jet circulation zones are formed, whereas for the original case this was only present at one side of the jet. Downstream the 75% constriction it is difficult to see a pattern, a lot of mixing seems to take place. All models seem to get more steady at about the same length after the glottis.

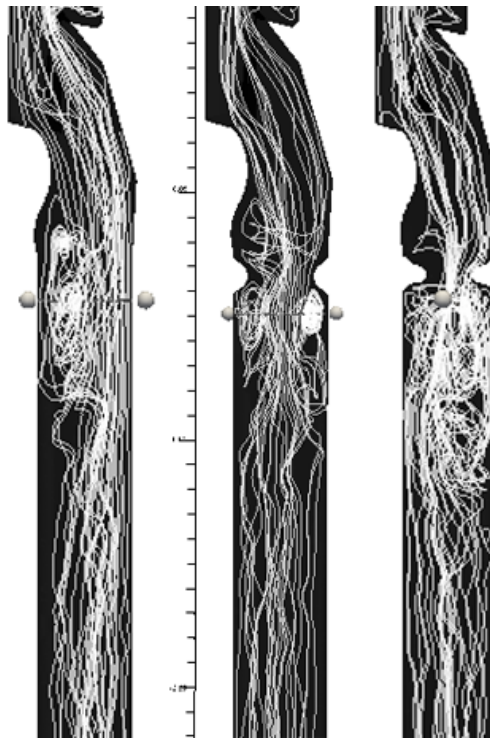


**Figure 4.4:** Simplified upper airway model, streamlines: original(left), 50% constriction (middle) and 75% constriction(right)

To get a better understanding of the flow and in particular the recirculation, the speed in vertical direction is presented in figure 4.5. First notice that in the upper part of the models, where they are still identical, the flow does not seem to be influenced yet by the constriction. Only after the epiglottis the flow changes per model (this is difficult to see from one instance but is more obvious for an animation). For example notice that for the constricted models there are circulation zones present above and below the constriction. The back flow above the constriction is stronger for the 75% case than for the 50% case. Also downstream of the constriction the back flow is stronger for the 75% constricted case compared to the other simulations as can be seen from the intenser colors. The backflow from the 50% and normal case seems to be approximately the same in strength. Further as can also be seen from the streamlines, indeed multiple zones exist for both of the constricted models. Do remember that it is a three dimensional flow so there is more to it than just the two recirculation zones that can be seen in this 2D cross section (around the entire circular constriction backflow zones

exist). For the highly constricted case it can be seen that the jet is diverted to the opposing side of the trachea compared to the original model. It is interesting to note that this is the side where softer tissue is present. The c-shaped cartillages, that give rigidity to the trachea, are placed on the side where the jet normally impinges. Now that the jet hits a more floppy part of the trachea this might introduce vibration. A fluid structure interaction simulation can probably give more information about this.

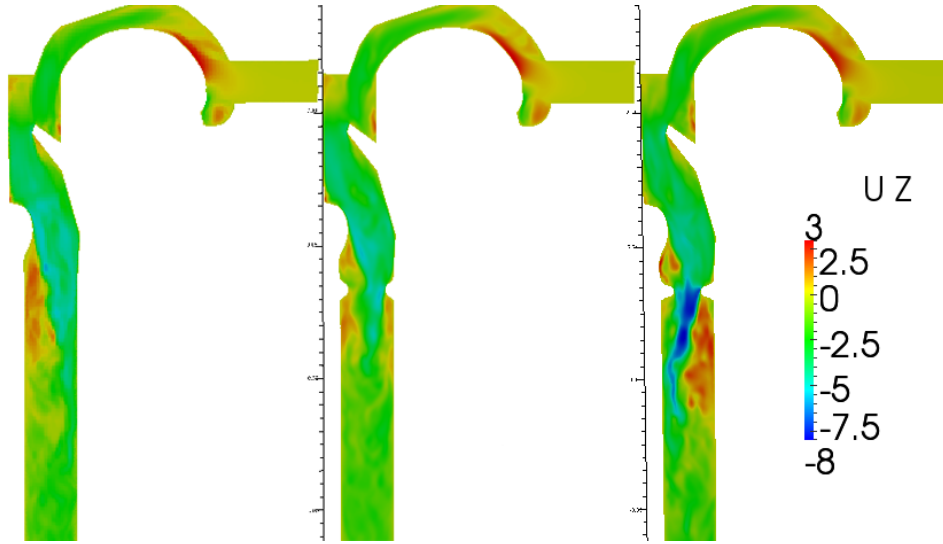


**Figure 4.5:** Simplified upper airway model,  $U_z$ [m/s]: original(left), 50% constriction (middle) and 75% constriction(right)

Next, in figure 4.6 the magnitude of the flow is shown. Notice that there is no noticeable difference in jet velocity between the original case and the 50% constricted case. From the snap shot shown here it can be seen that the jet is somewhat shorter. At first this is counter intuitive. However the jet must be diverted because of the constriction. The redirection of the jet to the middle of the trachea causes more mixing, and stress near the wall thereby reducing the jet length. For the most constricted case, the jet is longer than for the 50% constricted case. This is probably because of the increased jet velocity, and the placement of the jet against the wall, which reduces mixing compared the previous case. The maximum jet velocity is almost twice as high as for the other cases.

The vorticity can give more insight in the three dimensionality of the flow. As can be seen in figure 4.7, indeed in the 50% constricted case it seems that more mixing is taking place compared to the original case. The strength of the vorticity does not differ much and is only slightly increased due to the constriction. The amount however is different; the vorticity in the constricted case is spread over a larger area. For the 75% constricted case the vorticity strength *does* increase. Also further downstream more vorticity is present indicating that the flow remains turbulent for a longer period of time before becoming more laminar. This figure also indicates that the strength of the sources between the original case and the 50% constricted case should not differ to much. Whereas the 75% constriction case should show an increased source strength. Looking at figure 4.8 it is seen that the previous analysis is correct. The sources are surrounding the edges of the jet. This yields more sources in the constricted case than for the normal case. Further it can be seen that the sources for the

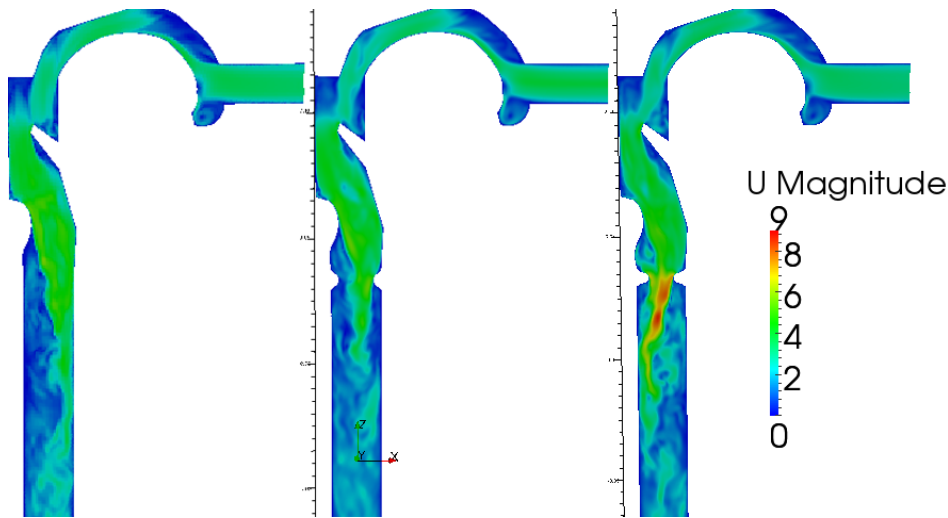


**Figure 4.6:** Simplified upper airway model,  $|U|[m/s]$ : original(left), 50% constriction (middle) and 75% constriction(right)

most constricted case are much stronger than for the other cases, as was expected from the vorticity. As was explained by surgeon Hans Hoeve from Erasmus Medical Center Rotterdam, a rule of thumb is that after 50% constriction stridor can be diagnosed. From the simulation a similar conclusion can be drawn (although only three cases are run). It is seen that the sources created by turbulence are not significantly stronger for the 50% constricted case compared to the normal healthy model, but are only present in a larger area. This more pronounced presence of the sources is probably the cause of stridor sound. However, it is not ruled out that due to for example tissue vibration the extra sound is created (compared to a healthy person). Most likely it is combination of multiple effects.

Finally in figure 4.9, the pressure is presented. The figures are *not* scaled the same. For the original case a pressure drop (normalized with density as is default in OpenFOAM) of approximately  $\pm 10 Nm/kg$  is seen. This increases to  $\pm 16 Nm/kg$  and  $\pm 34 Nm/kg$  for the 50% and 75% constricted case relatively. Hence the area reduction from 100% to 50% is of much less influence than the constriction from 50% to 75%. The person with the latter constriction will have severe trouble breathing since the lungs have to generate a bigger under pressure to get the same mass flow.

Now that all the aspects of the flow are shown it is important to know how good the results are, therefore a comparison is made with experimental PIV data. The averaged velocity profile is compared, similarly as was seen in section 4.3. Now the three different meshes are plotted together with the PIV data in figure 4.10. It should be noted that to the combination of result write-out rate and simulation time the average of the fine mesh is not yet fully converged. It is expected that the actual results are better than shown in the diagram as also becomes more obvious further in this section. Nonetheless all results are shown for the sake of completeness. It can be seen that the finest mesh shows very good agreement with the experimental data. Deviation can be caused by measurement inaccuracy, differences in measurement plane (the coordinates of the cross sections are not known exactly but are approximated), differences in geometry, boundary conditions and assumptions used in the numerical model.

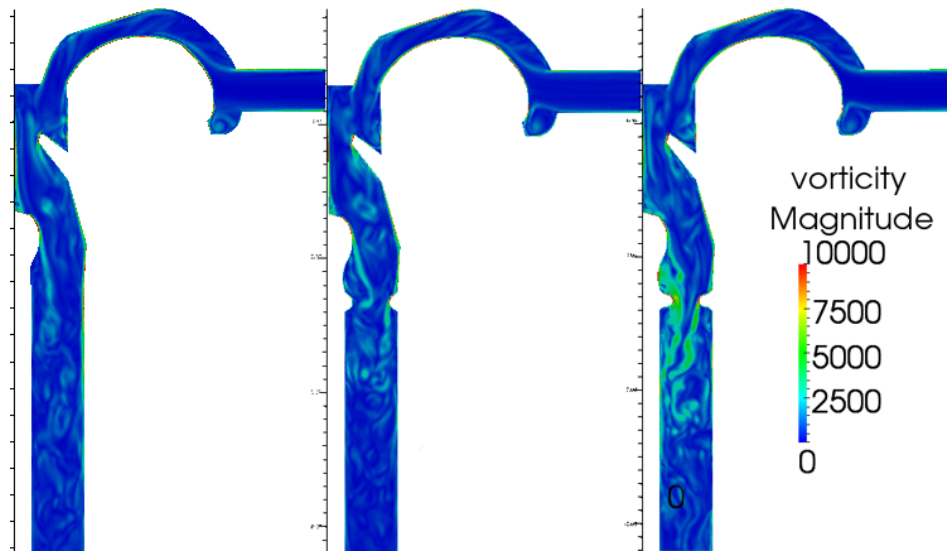


**Figure 4.7:** Simplified upper airway model, vorticity $[s^{-1}]$ : original(left), 50% constriction (middle) and 75% constriction(right)

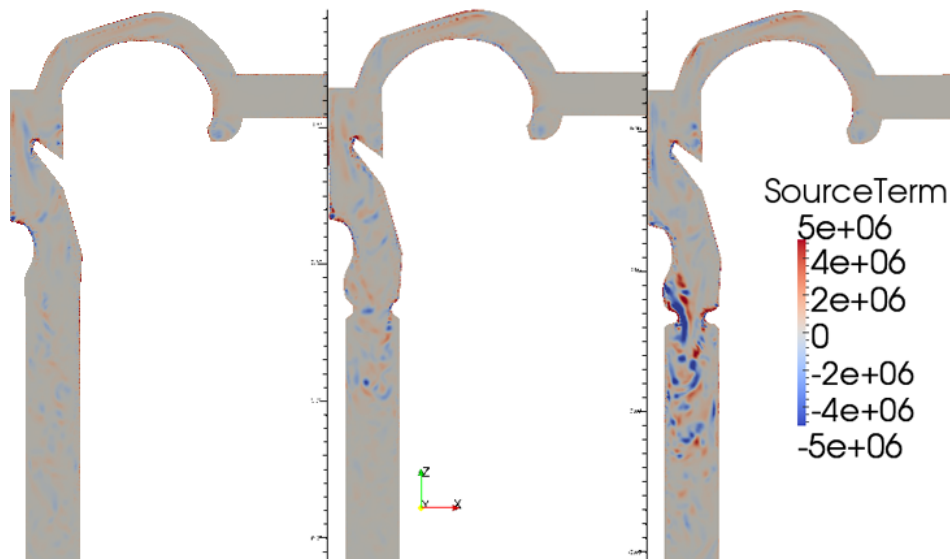


**Figure 4.8:** Simplified upper airway model, source term  $[kg/m^3/s^2]$ : original(left), 50% constriction (middle) and 75% constriction(right)

Before starting on the acoustic analysis the models used for this acoustic analysis, which

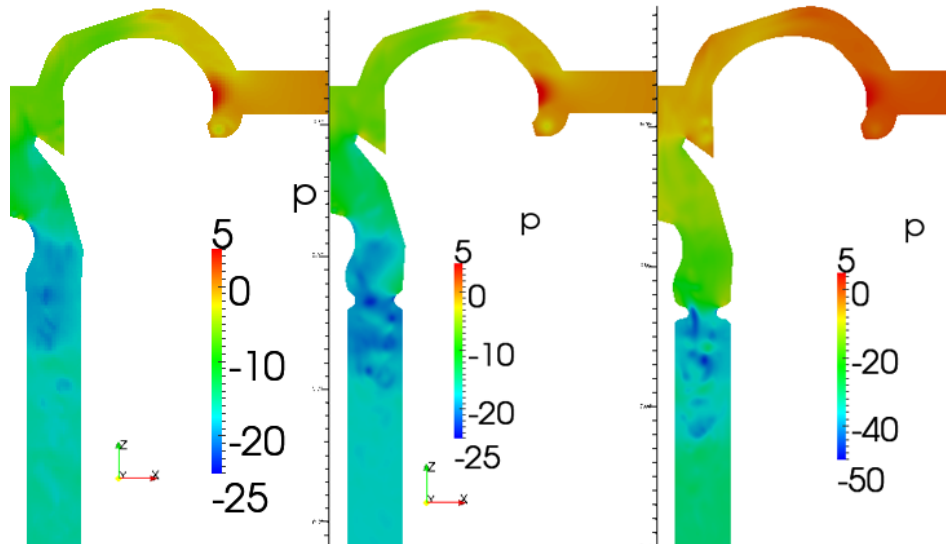


**Figure 4.9:** Simplified upper airway model, pressure [ $Nm/kg$ ]: original(left), 50% constriction (middle) and 75% constriction(right)

are slightly coarser than the ones shown up till now, are compared to the results for the finest mesh. This allows us to see whether the acoustic sources are calculated properly. Two instances that looked closely the same are selected from the fine and super fine 75% constricted cases and compared. In figure 4.11 the velocity in vertical direction is shown together with the velocity magnitude. The two instances look almost the same which allows for easy comparison. Some differences are seen because of the difference in time instance. However looking at the properties such as recirculation zones, separation and reattachment points and jet velocity, the figures are qualitatively the same.

In figure 4.12 the vorticity and source terms are plotted. Also here it is seen that the strength and distribution is very similar. It is difficult to spot significant differences. From this and the previous figures it is safe to assume that the acoustic analysis is based on realistic values, since both the flow structure and the resulting source terms calculated using the fine mesh are looking good compared to the finest mesh.

## 4.5 Acoustic analysis

Using the source terms seen in the previous section the density wave equation is solved. With this data a sound spectrum is created. As with the other simulations the raw acoustic data first needs to be detrended. A cut off frequency of 60 Hz is used, also the frequencies above 7000 Hz are not shown. This is because the frequency range of the human voice lies within

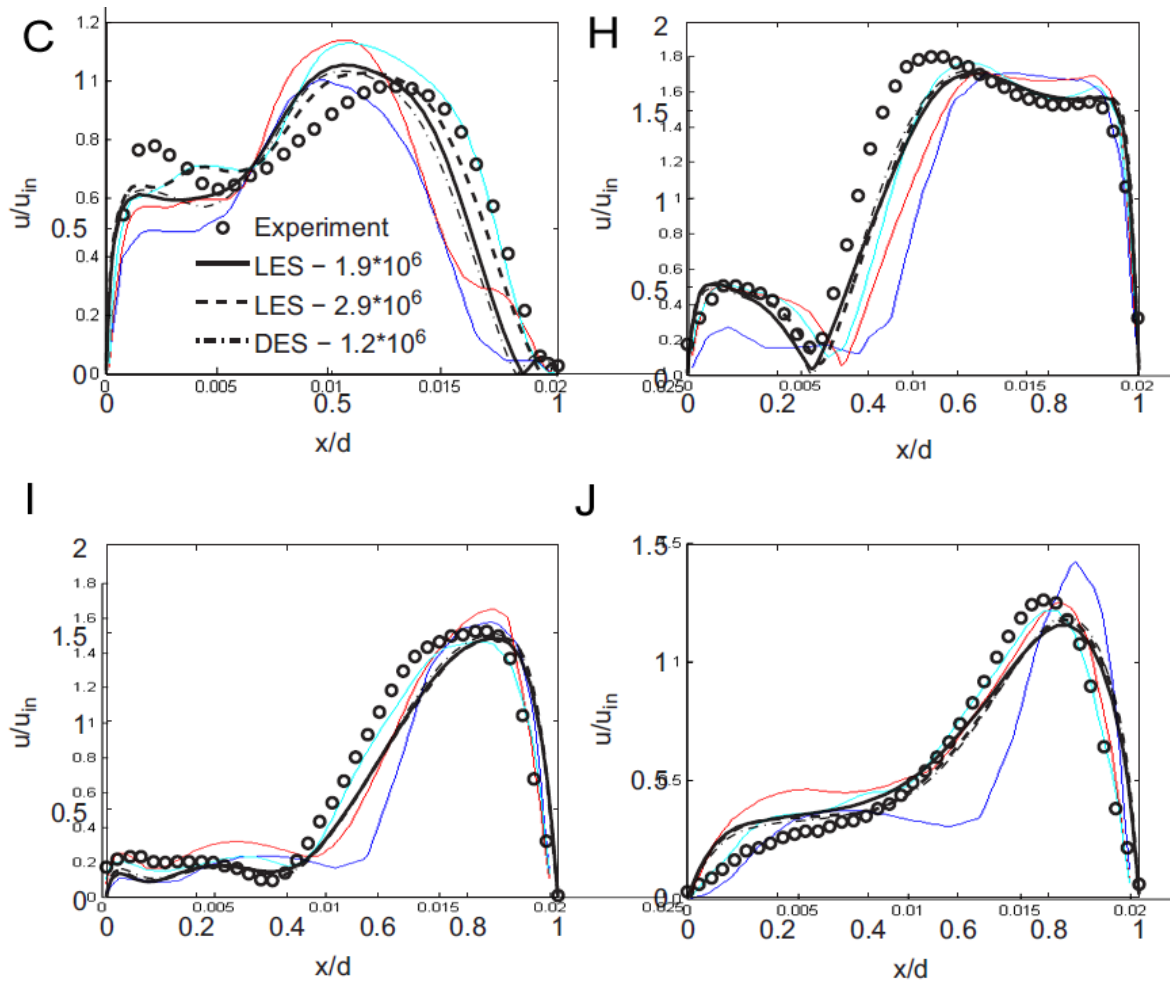


**Figure 4.10:** Comparison of different meshes with experimental data,  $(U_x^2 + U_z^2)^{0.5}/U_{in}[-]$ , Letters indicate cross sections in figure 4.1, —Coarse model( $8.89 \cdot 10^5$  cells), —Fine model( $2.52 \cdot 10^6$  cells) and —Super fine model( $4.52 \cdot 10^6$  cells). Reference[20]

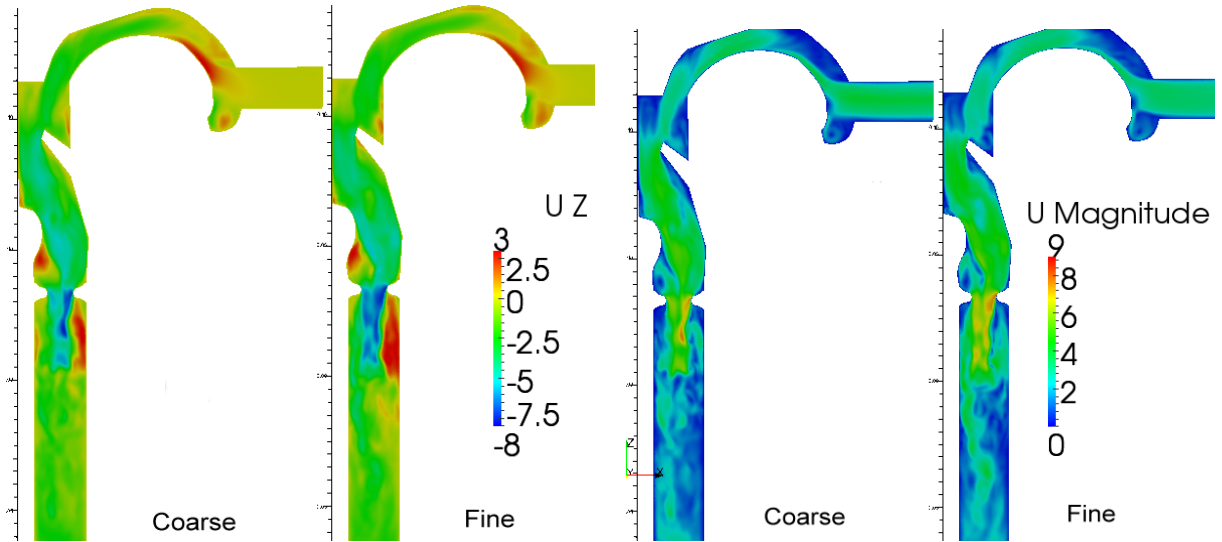


Figure 4.11: Simplified upper airway model, left  $U_z$  [m/s] and right  $|U|$  [m/s]

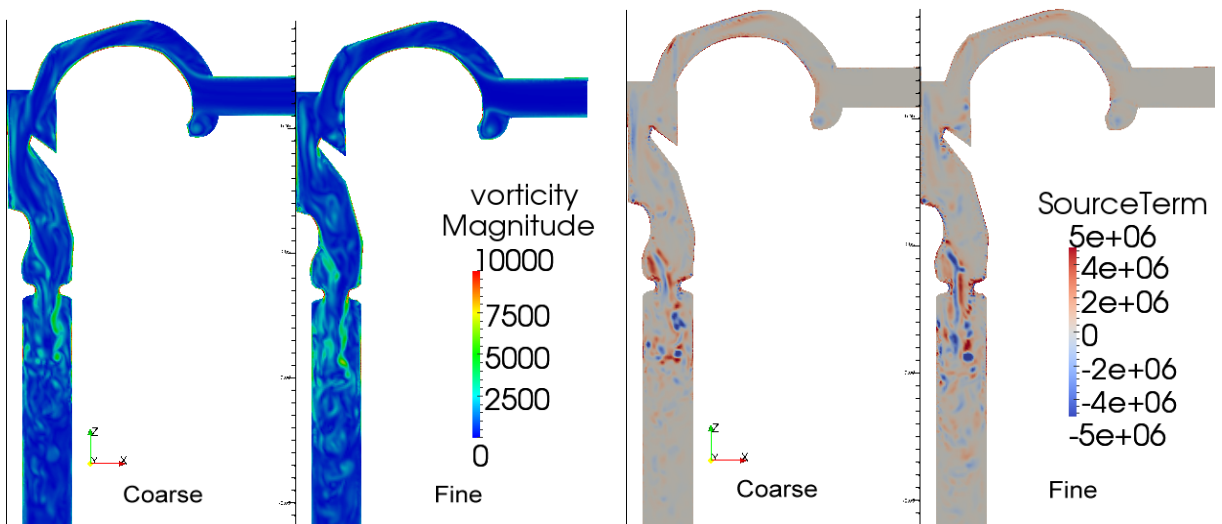
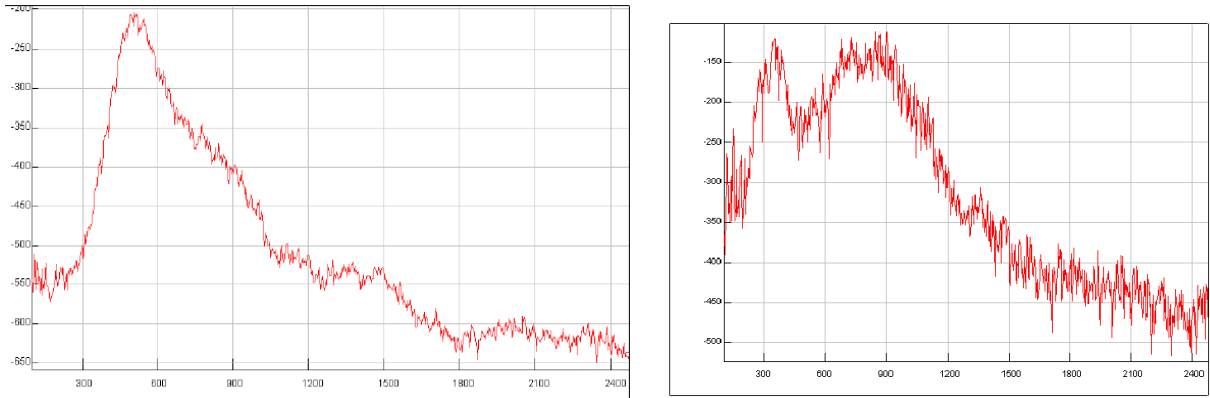


Figure 4.12: Simplified upper airway model, left vorticity  $[s^{-1}]$  and right source term  $kg/m^3/s^2$

these bounds [2]. In the experimental research on stridor performed by Zwartenkot[44] sounds with frequencies between 150 Hz and 2500 Hz are investigated. Hence it is expected that the most important features are seen using the ranges as reported in this thesis. In figure 4.13 and 4.14 some frequency spectra are shown from infant stridor patients. Samples were taken by Zwartenkot, and are analysed in the research mentioned earlier. Note that although these patients have a somewhat similar problem, the frequency spectra deviate a lot from each other. It can be seen than both toned and noisy features are seen. Further an overview of common sounds and the resulting sound strength is given in table 4.1. This table and the figures allows one to put the sound strength en spectrum in perspective.

**Table 4.1:** Common sounds and the resulting sound level[3]

Source of sound	Sound pressure level
Threshold of pain	130dB
Jet engine at 100m	110-140dB
Traffic on a busy roadway at 10m	80-90dB
TV (set at home level) at 1m	60dB
Normal conversation at 1m	40-60dB
Calm room	20-30dB
Auditory threshold	0dB



**Figure 4.13:** Averaged Fourier spectrum on experimentally obtained stridor sound[44], left: 15-month-old boy with subglottic stenosis, right: 1-week-old boy with a little subglottic stenosis and much supraglottic mucus

In figure 4.15 the pressure over time is plotted originating from the signal captured by the inlet and outlet probe of the normal and 50% constricted case. What can be seen is that the inlet and outlet signal are approximately the same and overlap quite well (because of the small length of the model almost no lag is seen). In figure 4.16 the same figure is seen but for

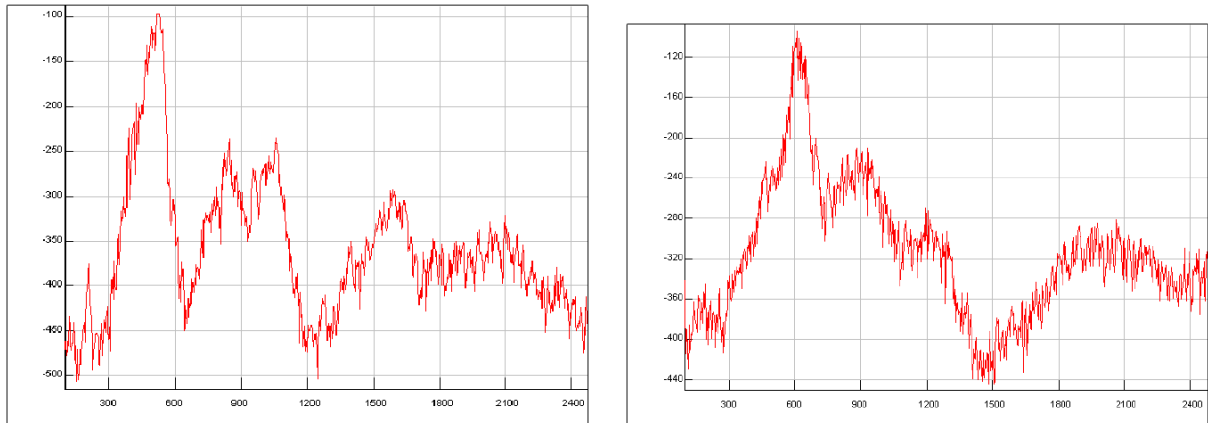


**Figure 4.14:** Averaged Fourier spectrum on experimentally obtained stridor sound[44], left: 16-month-old girl with subglottic stenosis, right: 11-month-old boy with a glottic and subglottic stenosis

the 75% constricted model. Here more difference can be seen between the inlet and outlet. This could indicate that waves are reflected from the constriction, prohibiting the waves from traveling upwards. Whether this is the case is discussed later on.

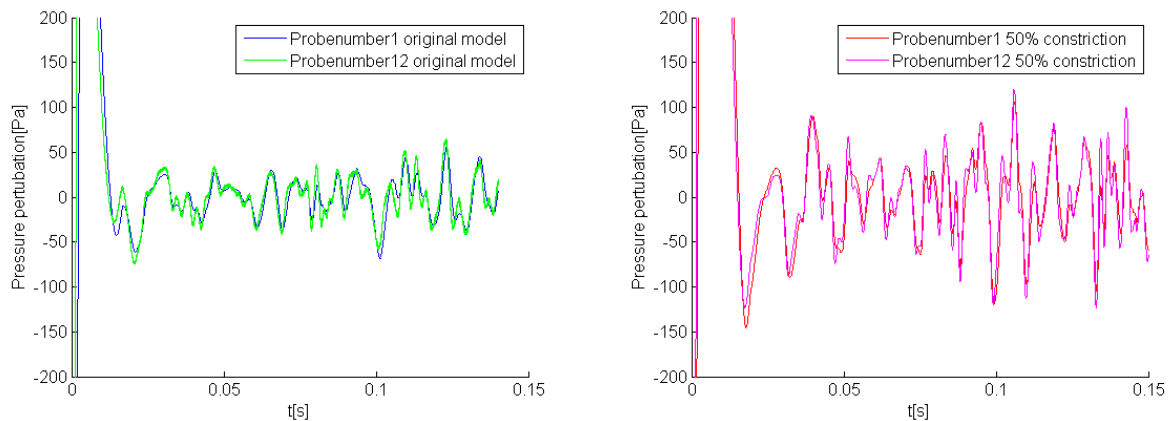


**Figure 4.15:** Simplified upper airway model, pressure[Pa] over time: Left original model and right 50% constricted model. Probenumber 1 is placed near the inlet and probenumber 12 near the outlet.

In figure 4.17 the same signals as before are shown but plotted together per probe. As expected the normal model shows the lowest amplitude signal. However, for the inlet the 50% constricted case shows the largest amplitude. This is somewhat unexpected, but could be because part of the highly constricted case signal is reflected when traveling upstream. Namely when looking at the outlet signal, in the right figure, the two signal amplitudes are much closer together. The overall signal frequency seems to increase for the increasing constriction when looking comparing the hills and valleys of the 50% and 75% constricted cases.

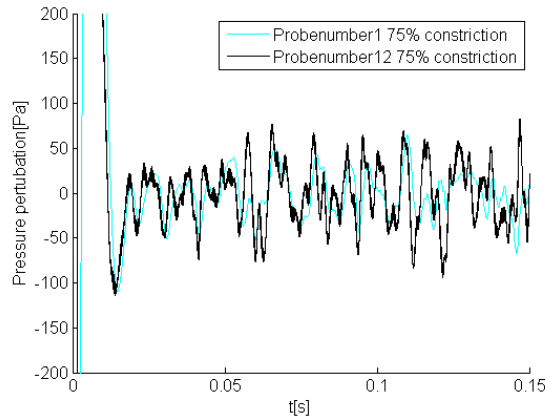


**Figure 4.16:** Simplified upper airway model, pressure[Pa] over time: 75% constricted model. Probenumber 1 is placed near the inlet and probenumber 12 near the outlet

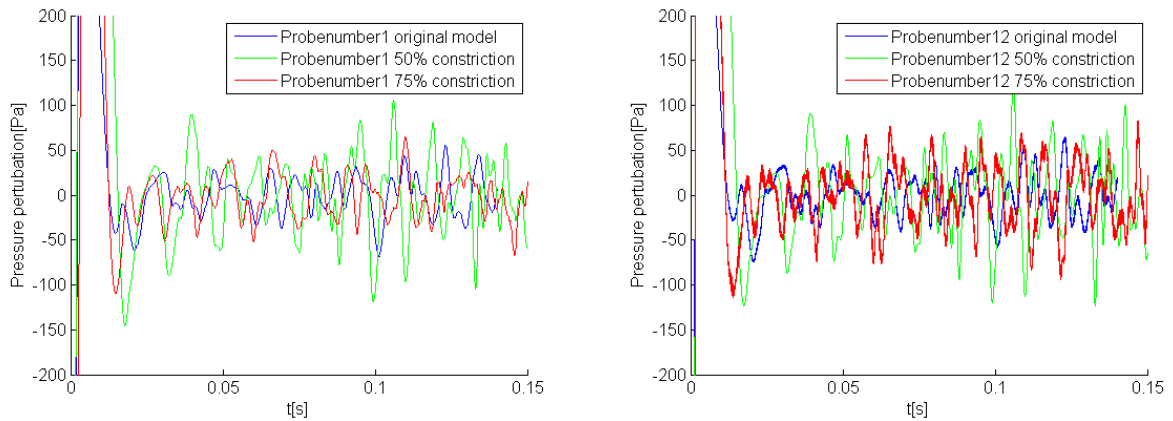


**Figure 4.17:** Simplified upper airway model, pressure[Pa] over time: Left all models inlet probe right all models for outlet probe

In figure 4.18 the frequency spectrum for the inlet is shown for two different ranges. When looking at the signal originating from the highly constricted case at the inlet it has the same level of noise for the lower frequencies (below 600Hz) as the healthy airway. However a peak is seen near 800 Hz. All higher frequencies show more signal strength with a difference of approximately 10dB compared to the healthy airway. The 50% constricted case shows an increase in sound pressure almost the entire frequency range. Also a peak is seen near 800 Hz. From 250 Hz up to 550 Hz it even shows a much larger signal strength than the most constricted case. However between 900 Hz and 1250 Hz the most constricted airway shows the strongest signal. For even higher frequencies the two signals have comparable strength. It can be seen that the strength of the signal for the low frequencies is probably slightly over predicted (keeping in mind the results for the diaphragm). The signal is larger than a normal conversation (see table 4.1). When comparing the spectra with those from actual

stridor sounds, as shown in figures 4.13 and 4.14, it is seen that the increase in signal strength towards the lower frequencies is normal, for the very low frequencies the sound pressure level should drop again. The latter observation is not represented in the signals calculated for the simplified upper airway model. Further it can be seen that stridor sound shows a more peaked signal. Although peaks are seen, they are not as pronounced as in the stridor sound. This could be explained by the missing tissue vibration and missing coupling between fluid, acoustics and tissue vibration.

Now looking at the outlet signal in figure 4.19, the values of the 75% constricted case are approximately the same as for the 50% constricted case. Also for the lower frequencies the signal is now larger than the healthy airway as was not the case before. From this the previous conclusion seems valid; part of the signal is blocked by the constriction. To investigate this more directly a sound perturbation is placed in the trachea. The acoustic signal propagation, without turbulent sound production, is measured at the inlet. This results in the signal shown in figure 4.20. Indeed a large part of the signal is blocked by the constriction. This is more so for the 75% case than the 50% case. This explains why the signal near the inlet can still be stronger for the 50% case than for the 75% case.

It is important to note however that the signal strength near the inlet should increase for increasing constriction. A possible explanation is that when a constriction increases the dominant sound production mechanism moves from turbulent flow to tissue vibration as the main source of sound. This is reinforced by the observation of the more significant pressure drop for the highly constricted case compared to the 50% constricted case as is seen in figure 4.9.

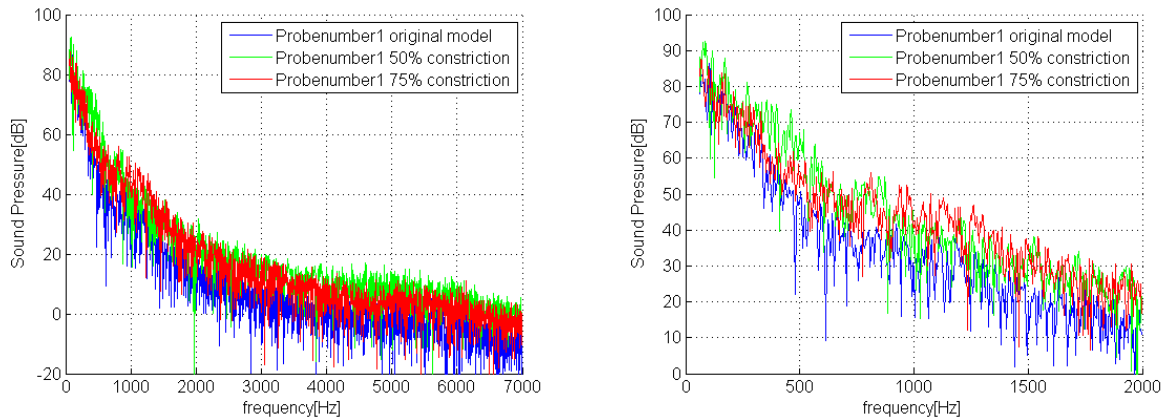


**Figure 4.18:** Simplified upper airway model, sound pressure inlet [dB]: Left overall view right zoomed view

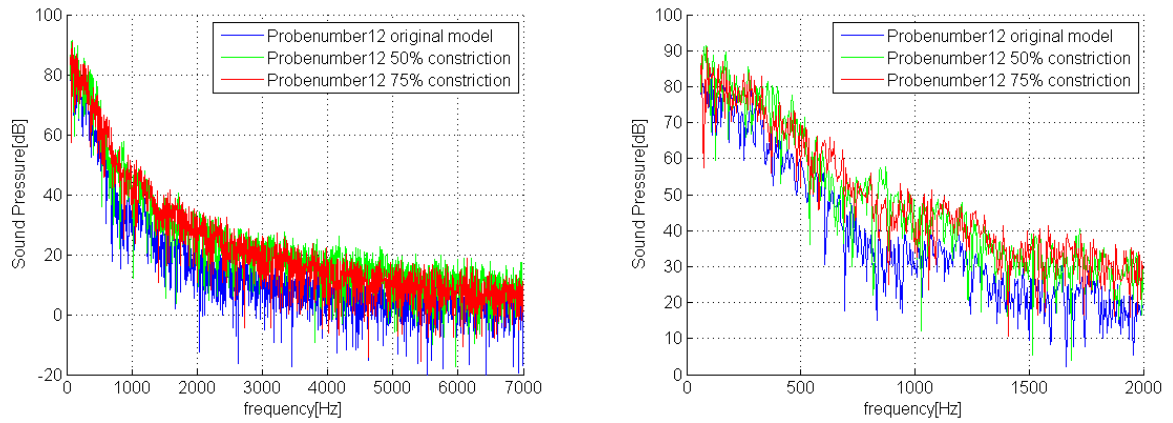


**Figure 4.19:** Simplified upper airway model, sound pressure outlet [dB]: Left overall view right zoomed view

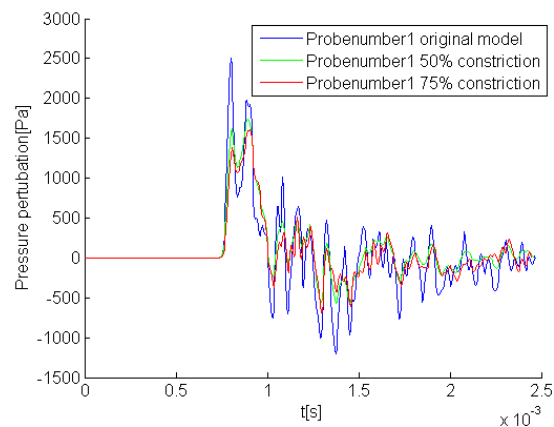


**Figure 4.20:** Simplified upper airway model, pressure [Pa] over time: Left 75% constricted model Right zoomed plot



## Chapter 5

# Analysis of a realistic CT-scan derived airway model

Using the experience that is gained from the previous models the final model, a realistic upper airway model (RUAM), is built. A stridorous is available and is adapted to obtain a 'healthy' patient such that comparisons can be made. By looking at both a healthy and stridor patient the predictive capability can be better investigated. The most interesting part is to see how the sound production changes for the two models and how this affects the sound propagation towards the exits. This gives insight into whether the computational model is sufficiently good for the analysis of realistic upper airways. And into what steps need to be taken before it can be used as a diagnostic tool. The models are presented in the first section. Next the boundary conditions are briefly discussed. This followed by the analysis of the results.

### 5.1 The geometry

For the RUAM two versions are created: one directly derived from a CT-scan of a stridor patient (This work was performed by Wim Vos at Fluida ([www.fluida.com](http://www.fluida.com))) the other was adapted (by author) such that it would represent a healthy (healthier) person. This adapting is a difficult task and rather subjective, since everybody's respiratory track looks slightly different. Using geometries from literature and consultancy from surgeon L.J.H. Hoeve (Erasmus MC, Rotterdam), the final geometry was created. The resulting model can be viewed in figure 5.1. Since the geometry is rather complex different views are shown in appendix A.4 to gain a better understanding.

First of all it should be noted that the top part of the model is not present. The algorithm to convert a CT-scan to a 3D-model is not optimized for the nasal cavity. And in the oral cavity almost no free space is present whilst not breathing through the mouth. The model is therefore cut off near the nasopharynx. This cut off influences the results in two ways. First of all the inlet condition is different; when the flow travels through the nose it needs to bend 180 degrees to arrive at the nasopharynx. The flow might become turbulent or separated before arriving at the nasopharynx. The inlet of the nasopharynx as modelled in the RUAM does not fully represent this flow correctly. However the area is relatively large in this part of the geometry which allows the flow to settle a bit. This probably reduces the inlet's effect on the sound production in the trachea (where most of the sound production takes place). Secondly the acoustic waves as measured near the nasopharynx might not be the same as

near the outlet in the mouth or nose. Since the waves are effected by the geometry the signal is altered in the region between mouth/nose - nasopharynx. However for this initial research this is not of great importance. The absolute value of the signal is not of importance, only the difference between the signals for the healthy and stridor patient are of interest.

On the anterior side two dead end air pockets are seen which are caused by tissue that is connected to the epiglottis and the epiglottic vallecula. On the posterior side there are air pockets which are most likely caused by the esophagus. Further down a v-shaped area can be seen which holds the vocal cords (just above section B-B in figure A.6). A small bump can be seen which is caused by the connection points of the vocal cords. Below the vocal cords a (sub glottic) stenosis can be seen for the original model (section B-B in figure A.6). It is attempted to remove this stenosis as can be seen in the figures shown in appendix A.4, also the difference in cross sectional area can be seen in these figures. Further downwards the trachea becomes bigger in cross section. Normally the cross sectional area should be more constant; however, it is very difficult to adapt this to nominal values. The healthy patient model is probably not fully optimal, however the resulting airflow should still be a great improvement (looking at noise production and ease of breathing) compared to what is seen in the original airway.

Two meshes are created for each model. A fine mesh and a mesh that is somewhat coarser near the boundary (coarse  $2.10 \cdot 10^6$  and fine  $3.38 \cdot 10^6$  elements). The fine mesh is used as reference model and did not generate acoustic results. The mesh that is used to obtain the acoustic results is somewhat coarser. Both meshes can also be viewed in appendix A.4.

## 5.2 Boundary conditions

Although the boundary conditions for the realistic upper airway model are approximately the same as for the simplified model they are briefly repeated here. At the inlet the differential, density normalized, pressure is uniform  $0Nm/kg$  and the velocity inlet is determined automatically by the pressure difference. This allows a non-uniform inflow which is beneficial for the RUAM, because the oral and nasal cavity are not available in the computational model.

At the outlet the pressure has a zero gradient condition and the velocity is imposed such that the correct mass flow is achieved. For the RUAM there is no reference data, neither are patient measurement data available. The only thing that is known, is that RUAM is derived from a CT-scan. During this scan the patient must breath very slowly. Therefore the geometry of the airway is valid for slow breathing; the boundary condition should represent this same condition. A value of  $12L/min$  is chosen, which should be a good mean value (see section 1.2).

Also for these models reflection caused by the pressure boundary conditions could be a concern. However both the inlet and the outlet conditions are relatively steady, this reduces the effects of reflected pressure waves. For the acoustic waves again a convective outflow is used. The wall close to the in and outlet also have a convective boundary condition for better convection of waves perpendicular to the inlet.

Further near the inlet and outlet the source term is manually set to zero to reduce numerical noise caused by these parts of the model.

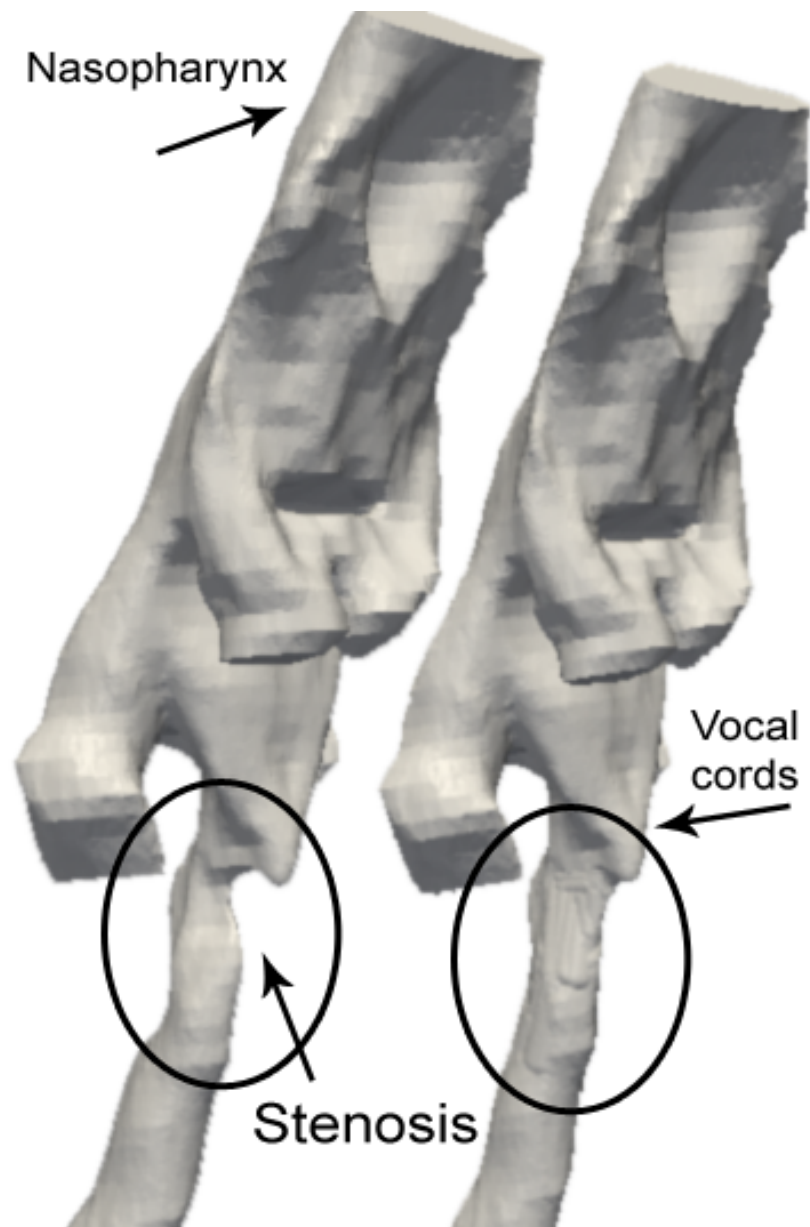
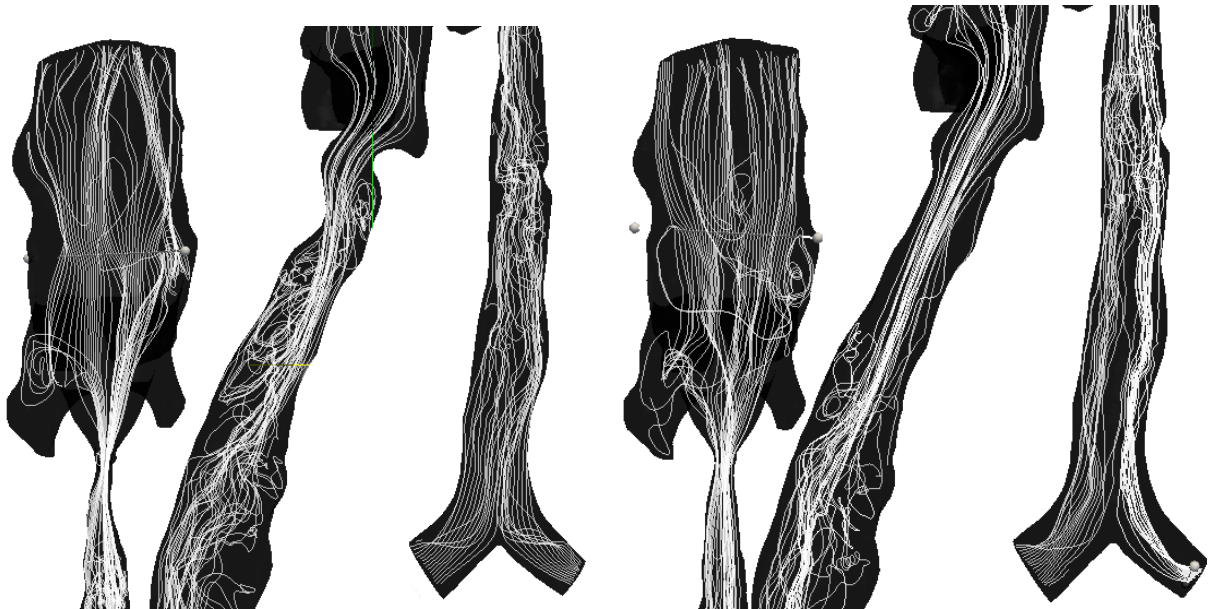


Figure 5.1: RUAM layout. Original (left) and adapted(right)

### 5.3 Fluid flow analysis

Because of the complexity of the geometry it is difficult to get a good view of the flow field in every part of the model. Therefore two cross sections are shown for most figures thereby hopefully getting a better understanding. The plane which is used to create the cross sections can be viewed in the appendix figure A.10.

In figure 5.2 the stream lines are displayed for a single time step. From this the 3D nature of the flow becomes apparent immediately. Especially below the vocal cords the jet causes a transition to more turbulent flow. For the stridor patient model strong back flow is seen next to the jet, also below the jet the flow is highly three dimensional. Near the outlet and inlet the flow shows more laminar behaviour. Of course near the outlet the flow is forced to become more uniform because of the boundary conditions. However in a lung the divisions to smaller and smaller bronchi also removes the larger eddies which enforces forces laminar flow. For the healthy person only below the jet back flow is clearly visible. Near the inlet and outlet the flow is very similar.



**Figure 5.2:** Realistic upper airway model, streamlines: left - stridor patient and right - healthy person  
The figure shows part of the RUAM starting at the top on the left side and finishing on the right side of the figure at the bottom of the RUAM

The placement of the jet and the velocity field can be seen in figure 5.3. The first thing that can be seen is the large difference in velocity. The velocity magnitude of the jet of the stridor patient model is about  $18m/s$  while the jet of the healthy patient model is about half of this value. This is due to a combination of an increased cross sectional area and because the flow can stream more smoothly resulting in a more uniform flow stream toward the trachea. In the stridor patient model the flow needs to bend more due to the constriction. The flow thereby experiences adverse pressure gradients causing flow separation and jet formation. This yields stronger back flow(see also figure 5.4).

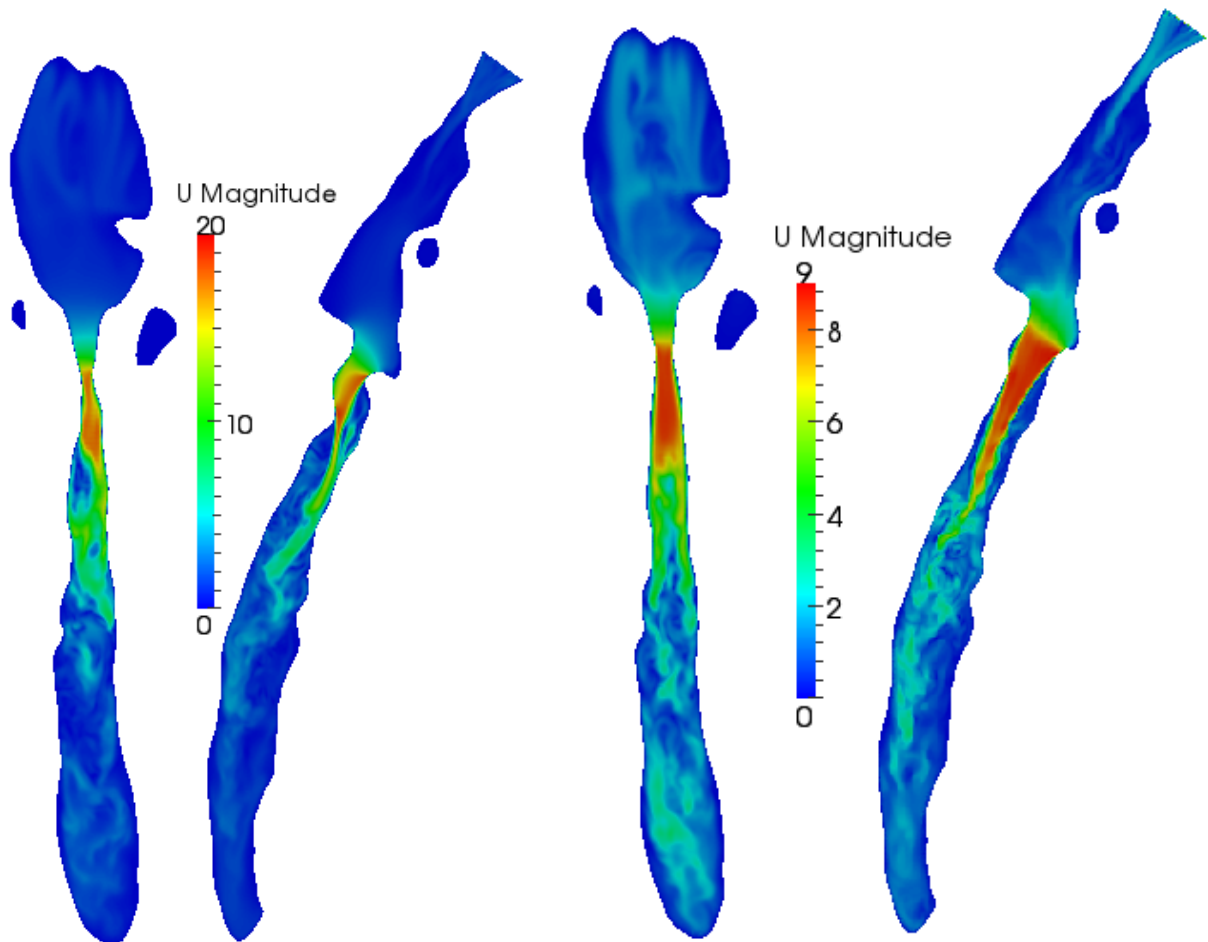


**Figure 5.3:** Realistic upper airway model, velocity magnitude[m/s]: left - stridor patient and right - healthy person

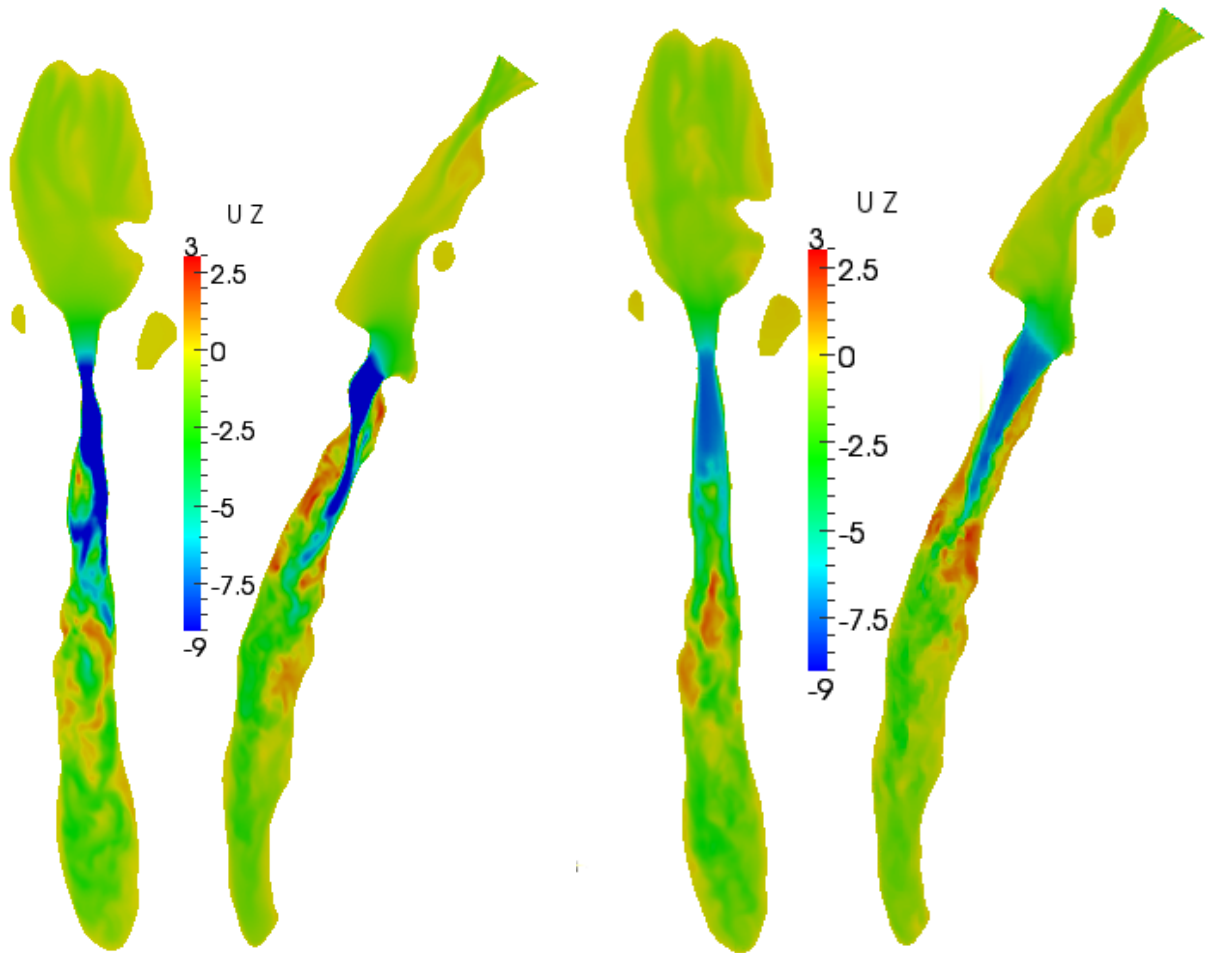


**Figure 5.4:** Realistic upper airway model, velocity z-direction[m/s]: left - stridor patient and right - healthy person

As was explained in section 2.1 the LES model makes use of a selection function. This selection function gives insight in what parts of the flow turbulent behaviour is expected. The selection function is shown in figure 5.5. The figure reinforces what was already seen in the stream lines. The selection function is mostly zero near the inlet indicating laminar behaviour. Near the vocal cords, where the jet starts, turbulent behaviour is seen in the stridor patient model. Also surrounding the jet and downstream the jet turbulence is present. For the healthy patient model it can be seen that the jet is more laminar and less three dimensional indicated by the small lower value for the selection function; mostly downstream of the jet turbulence is seen. Near the outlet also more laminar behaviour is seen, for both models, although to a lesser extend as the near the inlet.

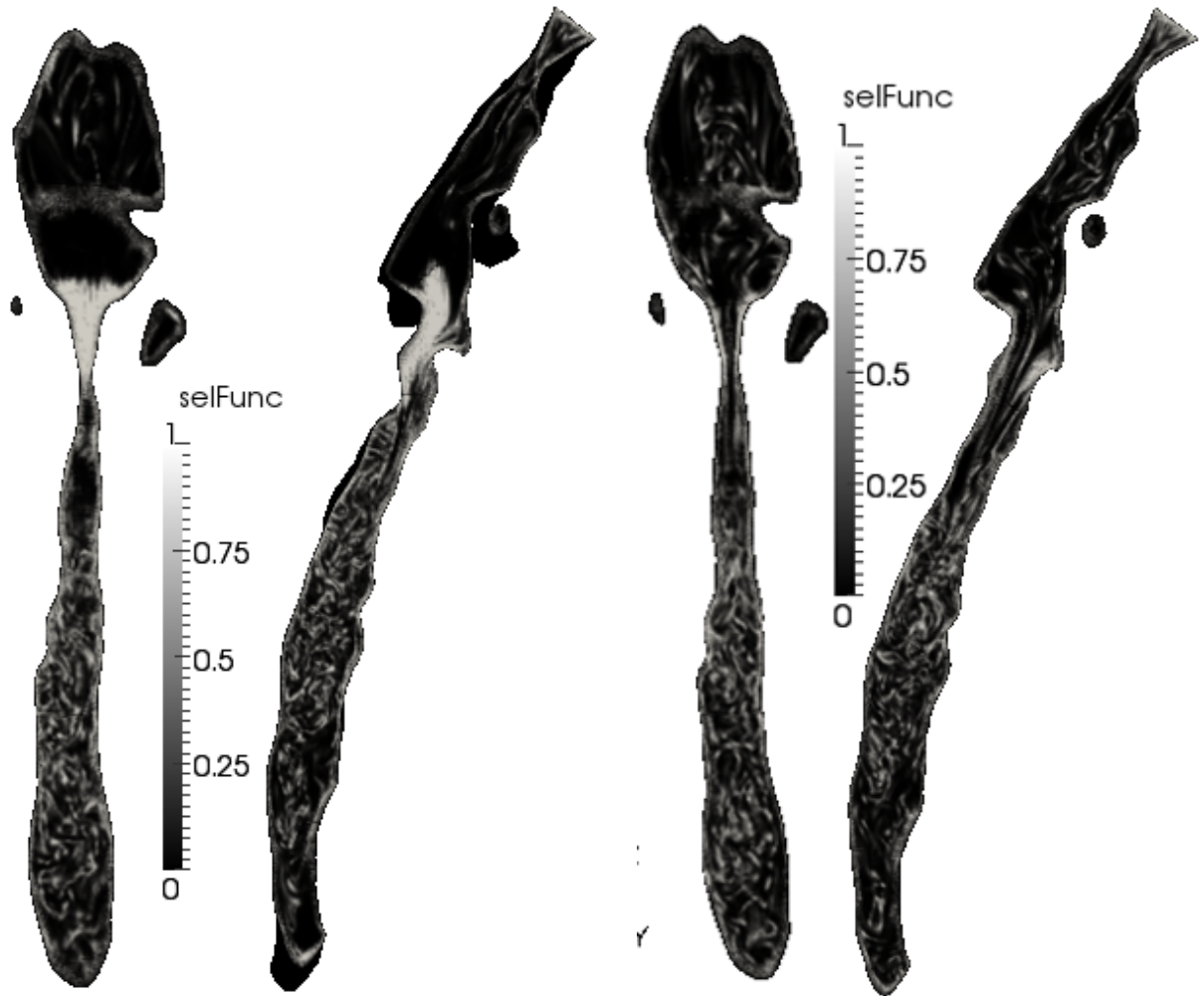


**Figure 5.5:** Realistic upper airway model, selection function[-]: left - stridor patient and right - healthy person

The vorticity is used to calculate the selection function. Also it is an indicator for the production of sound. Therefore in figure 5.6 the vorticity is shown. The vorticity in the constricted model is stronger and also is spread to more parts of the computational domain. Below the jet the vorticity magnitude and patterns are similar for the two models, yet next to the jet the vorticity is stronger for the stridor patient RUAM.

Now take a look at the source terms in figure 5.7. The same range is used for the legend for both models. First of all the acoustic sources are about 5 times stronger for the constricted case and are active in a larger part of the domain. The healthier model shows less sound production although not a whole order of magnitude. Possibly the healthy person's upper airway is not modified enough to get to the point of a regular amount of sound production. Now the area near the constriction is changed from  $16\text{mm}^2$  to  $29\text{mm}^2$  which is still lower than a factor 2. This factor could have been increased a bit. Another explanation is that it might be the case that a healthy patient still produces turbulent sound production but not a whole order of magnitude smaller than a stridorous patient. A simulation of a real healthy person, using a CT-scan derived model instead of a manually adapted model, should provide more information about this.

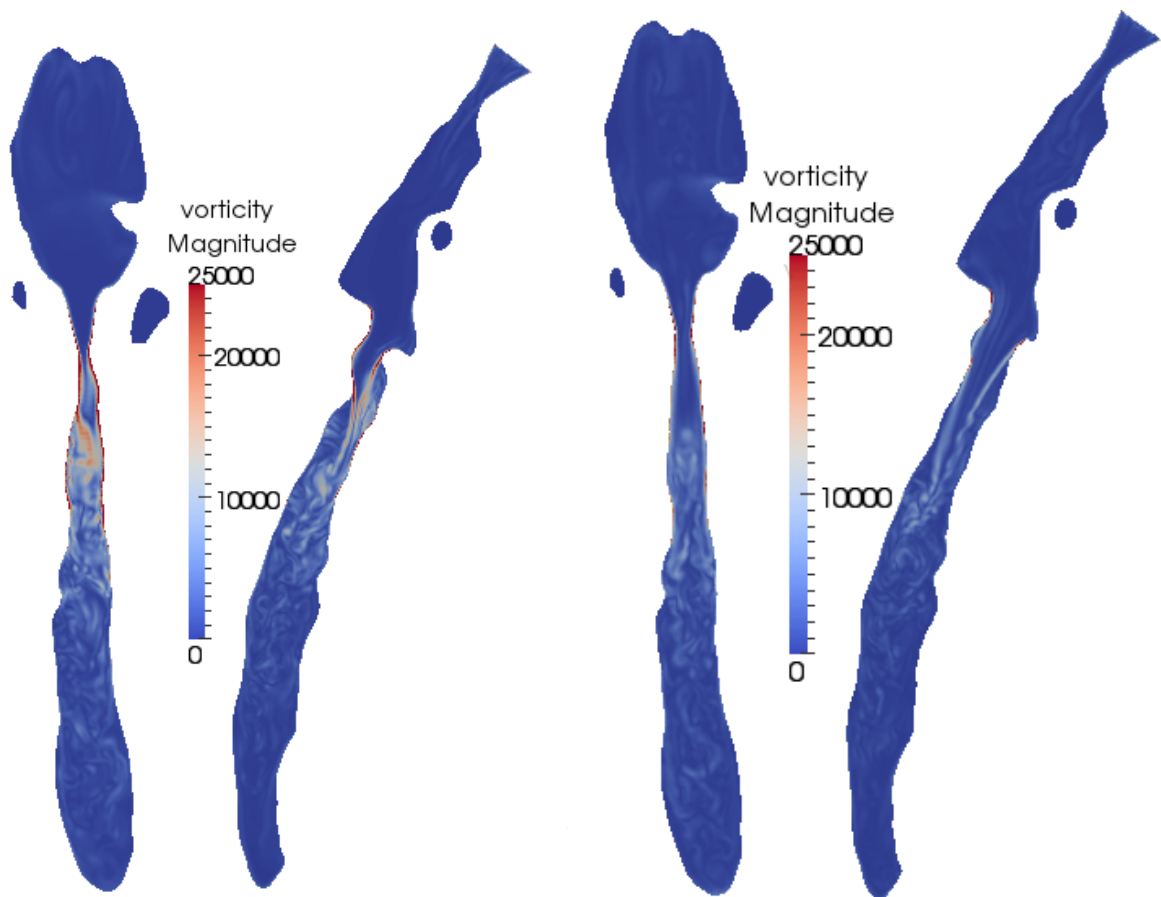


**Figure 5.6:** Realistic upper airway model, vorticity magnitude field [ $\text{s}^{-1}$ ]: left - stridor patient and right - healthy person

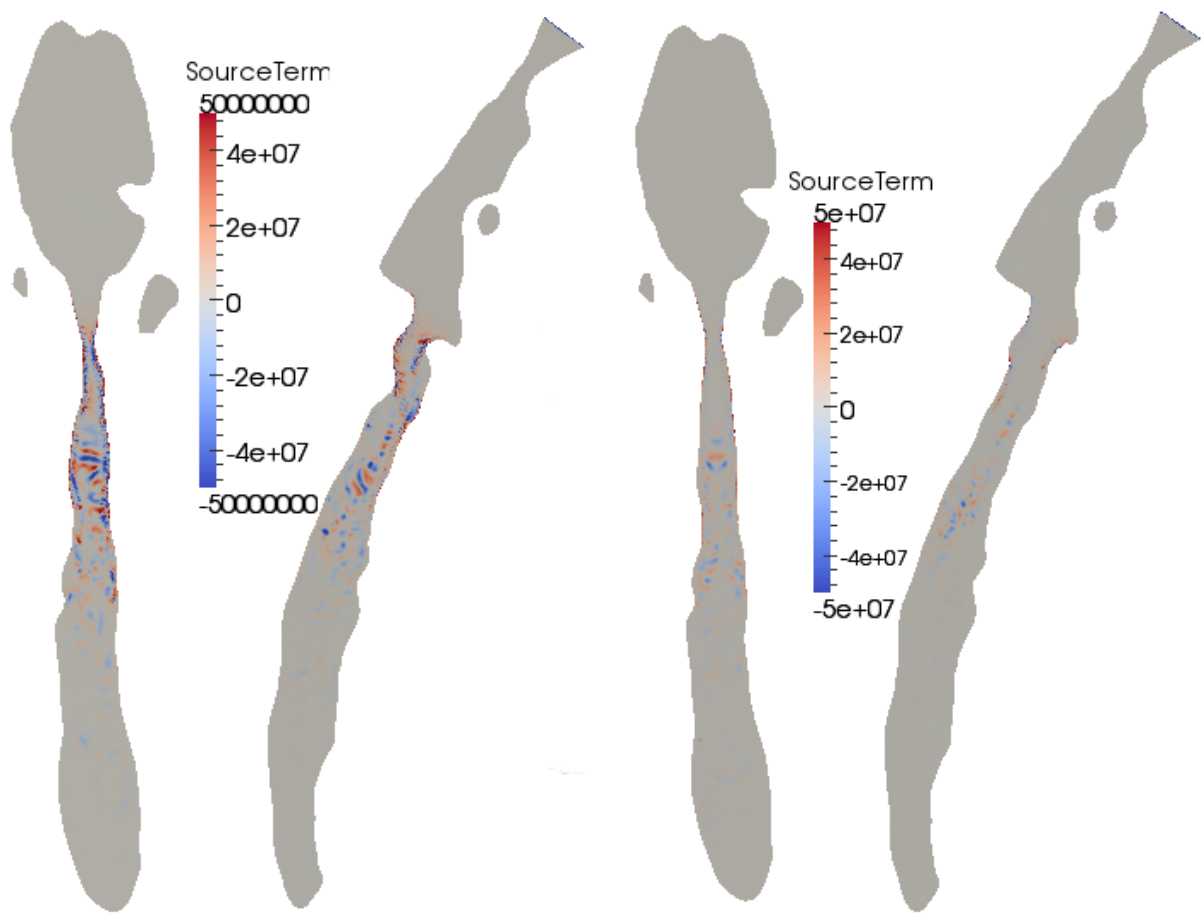


**Figure 5.7:** Realistic upper airway model, source term [ $kg/m^3/s^2$ ]: left - stridor patient and right - healthy person

Finally in figure 5.8 the pressure is shown. A large difference can be seen between the two models. The constriction causes a large pressure drop (about 5 times larger) which indicates that the stridorous patient needs more effort to obtain the same mass flow as a healthy patient even for quiet breathing.

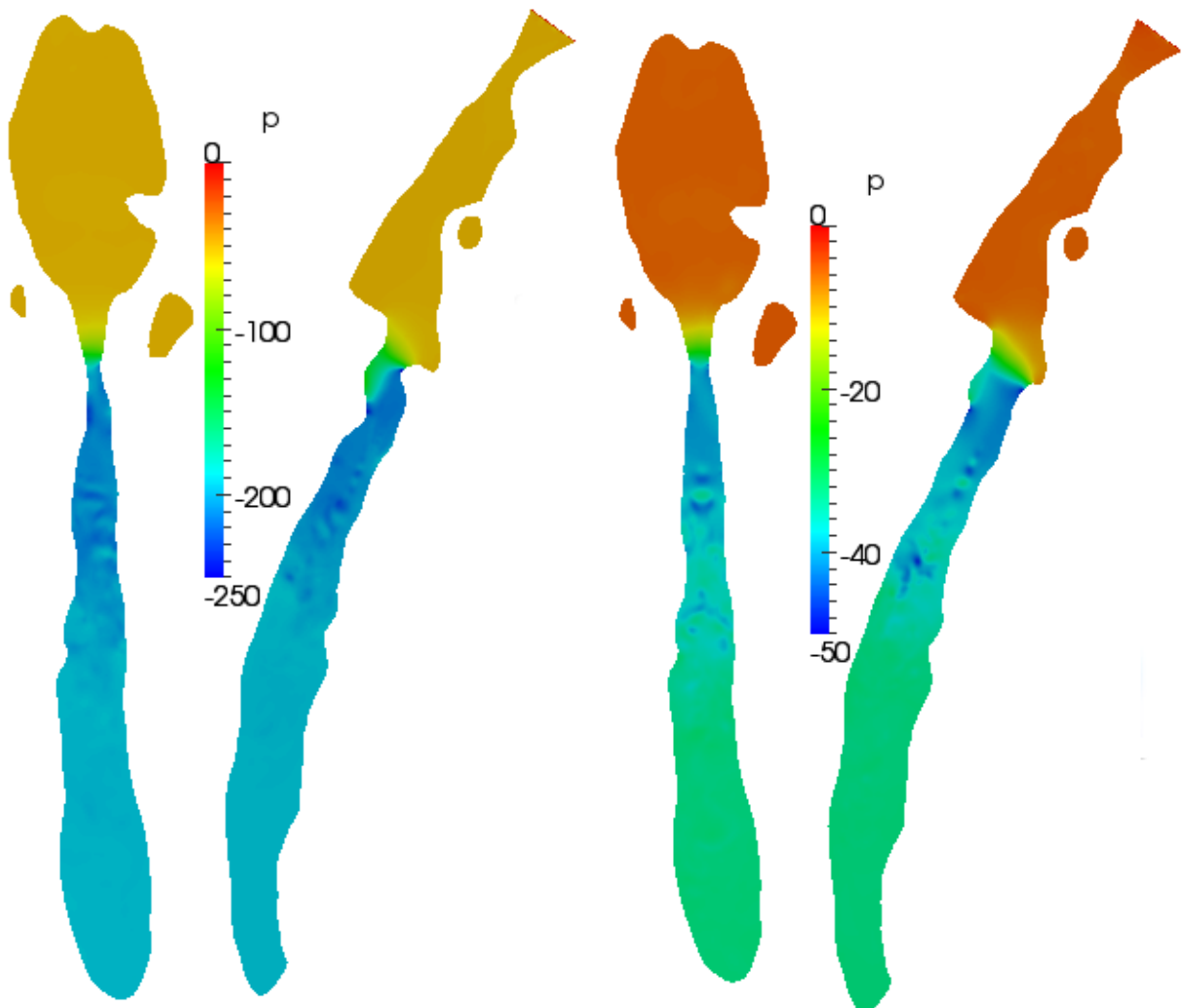


**Figure 5.8:** Realistic upper airway model, pressure[Nm/kg]: left - stridor patient and right - healthy person

As is mentioned in section 5.1 two mesh densities are used. In order to see the effect of reducing the mesh density some figures are now compared with each other. Only one view is shown for easier comparison. Further it should be noted that the difference between the

densities is mainly near the boundary layer. Also the snapshots of the different models are taken at a different time instances (the fine model was not run as long as the coarser model).

In figure 5.9 the velocity field can be seen for the different models. Note that the colour scaling for all models is the same to facilitate direct comparison. This is done to clip the results for the constricted model since part of the values fall outside this range. Between the coarse and fine models no significant differences are seen; only near the first separation point of the original model a different structure is present. This could however also be caused by the difference in time instance. An interesting feature that now can be seen now that the legend is scaled the same, is that the jet of the constricted model is not a whole lot longer than for the healthy patient model (when taking the jet length up to the green colour, this is 74mm for the stridor patient versus 62mm for the healthy patient). Just below the jet, at about half of the trachea (this is the part from just constriction up to the first bifurcation, also see figure A.6) the flow patterns converge to a similar solution. This can also be caused by the outlet boundary condition. For future research it is interesting to change the boundary conditions to for example a pressure-pressure boundary condition (now that pressure drop is already calculated in this report it does not have to be determined iteratively).

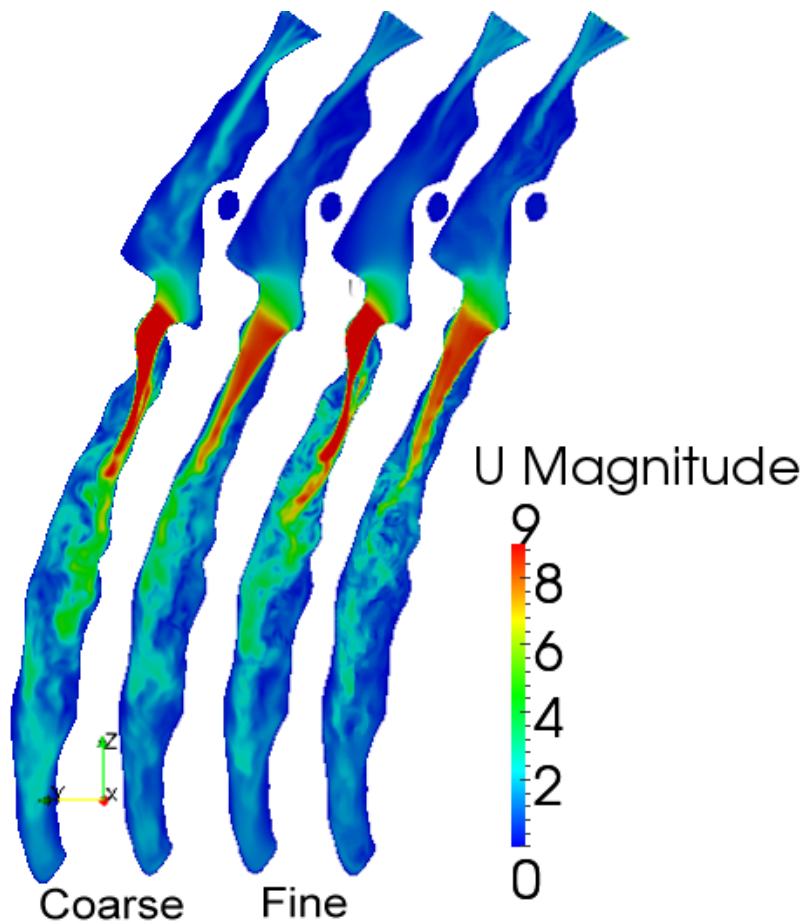


**Figure 5.9:** Realistic upper airway models, velocity magnitude [ $m/s$ ] from left right: stridor patient (coarse), healthy person (coarse), stridor patient (fine) and healthy person (fine)

The vorticity, figure 5.10 looks good. Also the source term, figure 5.11 shows only small differences between coarse and fine mesh. Note that the source term is displayed using a range that presents the sources of the healthy patient model better. The reduction of sources closing in on the outlet seems similar for constricted and healthy model. Near the jet the stridor patient model shows more sources over a larger area. The amplitude of the sources are almost exactly the same. Also the size of the sources is captured correctly by the coarser grid. This indicates that frequency of the sources is probably calculated correctly for the coarser mesh and validates the use of this model for the acoustic analysis.

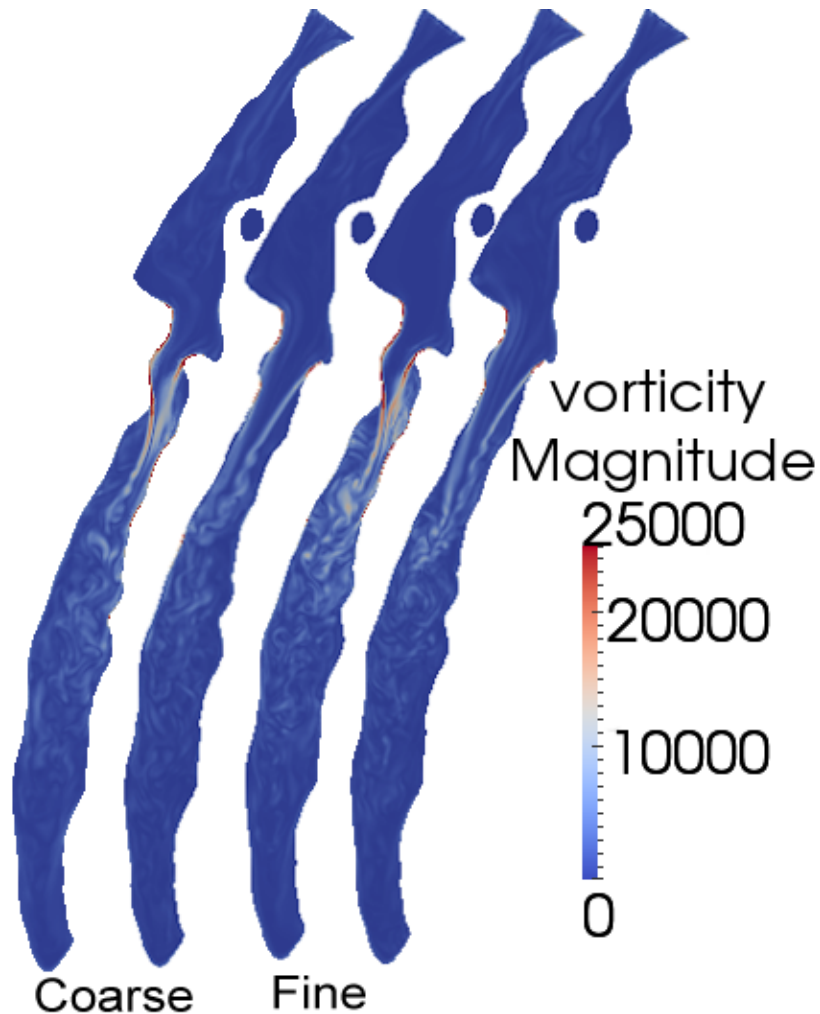


**Figure 5.10:** Realistic upper airway models, vorticity magnitude[ $s^{-1}$ ] from left right: stridor patient(coarse), healthy person(coarse), stridor patient(fine) and healthy person(fine)

## 5.4 Acoustic analysis

For the realistic upper airway model the acoustic analysis is done in a similar fashion as for the simplified upper airway model. Hence first detrending is applied and the pressure

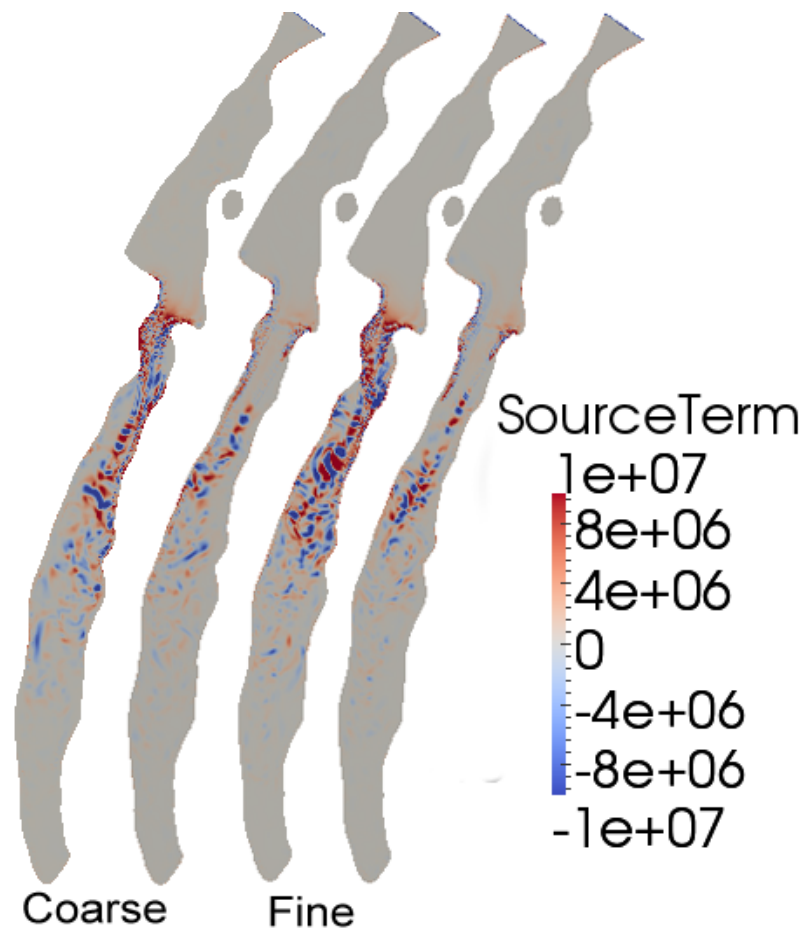


**Figure 5.11:** Realistic upper airway models, source term [ $kg/m^3/s^2$ ] from left right: stridor patient(coarse), healthy person(coarse), stridor patient(fine) and healthy person(fine)

perturbation is clipped (first 0.017s) to perform a Fourier analysis. It will be interesting to see how results compare between these two upper airway models.

First, the signal over time is shown in figure 5.12. As with the SUAM it can be seen that the acoustic signal for the normal(ized) case is almost identical for the inlet and outlet whereas for the constricted case the signal is different. This effect is even more pronounced than for the SUAM case. Also when comparing the two signals, in figure 5.13, interesting things can be seen. It seems that the signal at the inlet for both models is approximately the same. At the outlet the constricted case clearly shows an increased amplitude. The increased amplitude at the outlet is expected, however also at the inlet this should be the case.

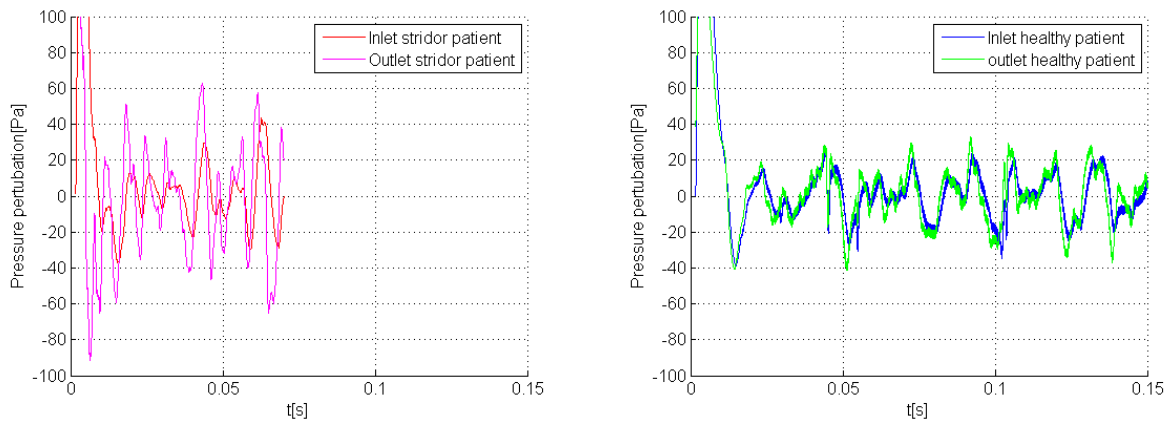


**Figure 5.12:** Realistic upper airway model, pressure[Pa]: left stridor patient and right healthy patient

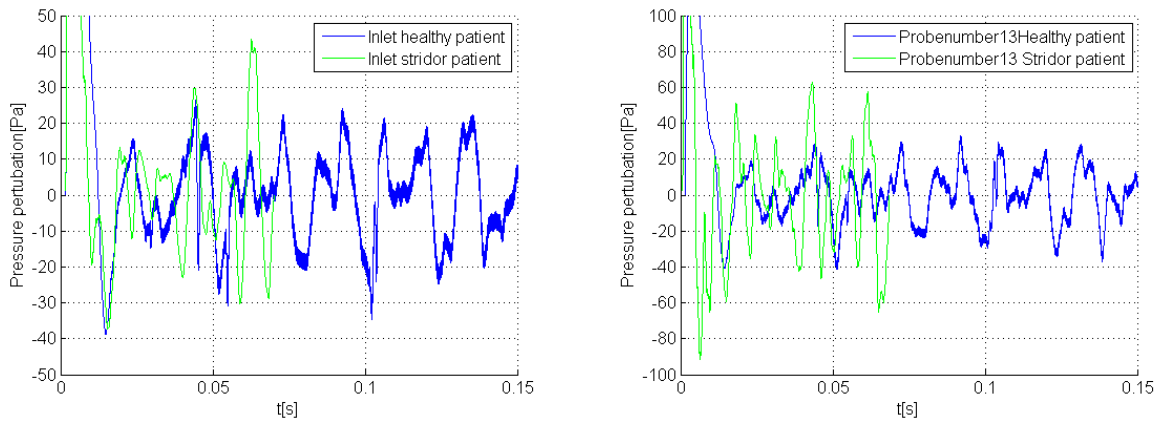


**Figure 5.13:** Realistic upper airway model, pressure[Pa]: left inlet and right outlet

The previous describe properties should also be seen back in the Fourier transformed signal in the form of the strength of the signal. Indeed this is the case by looking at figure

5.14 and 5.15. When looking at the inlet the signal from the healthy version and the stridor patient model look very similar. At some frequencies the constricted model even shows a lower sound pressure level.

There is a fundamental frequency for both models around 5500 Hz. This frequency is too high to be caused by stridor, looking at figure 5.16 which shows an experimentally obtained frequency spectrum it looks like the main power is before 5000 Hz. The peak could be caused by internal reflections in the model or a sharp edge at the boundary (two elements with a large angle placed anywhere with a sufficient high velocity), however for a complex geometry it's very difficult to determine where certain signals come from. One possibility could be from the area just above the glottis. The distance between the anterior and posterior side is approximately 30mm. A back and forth moving wave at this location would have a frequency of approximately  $346.15/(0.03 * 2) = 5767$  Hz. Although no sources are present here waves could still reflect towards this area.

When looking at the outlet some increased sound pressure can be seen for the constricted model near 150 Hz and 300 Hz. Also in the range 1600–2000 Hz an increase is seen in sound pressure level for the constricted model. The rest of the model seems to be of a similar level (Except near the large peak at 5500 Hz).

For the RUAM similar behaviour is seen as for the simplified model. The constriction seems to block part of the upstream travelling waves. Since the two approaches confirm each other more investigation into this phenomena would be interesting. Does indeed the dominant mechanism shift from turbulent sound production to tissue vibration? Perhaps a fluid structure interaction simulation would give more insight into this. For example it could be the case that the pressure drop causes more tissue vibration for the stridor case than for the healthy case. This would result in an increase sound pressure level at the inlet and outlet opposed to what is currently seen, only an increase of signal strength near the outlet.

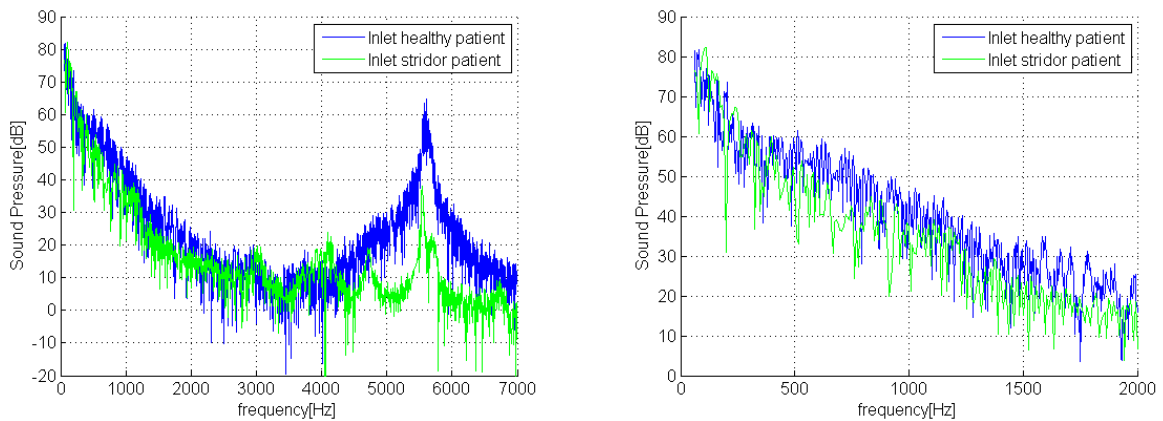


**Figure 5.14:** Realistic upper airway model, inlet sound pressure [dB]: left overall spectrum and right zoomed spectrum

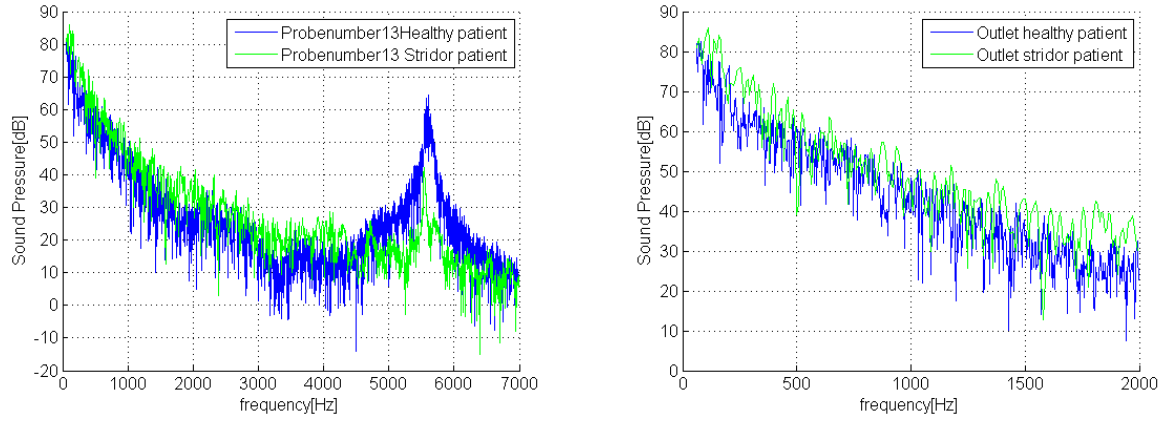


**Figure 5.15:** Realistic upper airway model, outlet sound pressure [dB]: left overall spectrum and right zoomed spectrum

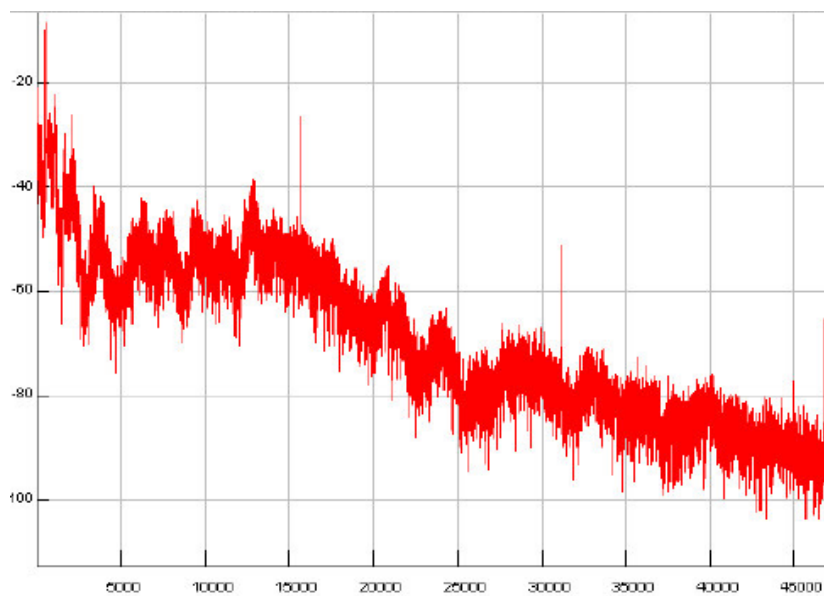


**Figure 5.16:** Frequency spectrum from experimental stridor sample from reference [44]

## Chapter 6

# Conclusions

In this report the acoustic numerical analysis of a stridor patient is discussed. There is a need for uninvasive diagnostics because of risks involved using anaesthetics, especially on young children. To find the obstruction from sound, first one needs to know what kind of sound is produced by what kind of geometry. Doing this numerically has the advantage of allowing one to change only one parameter at the time (geometric wise but also boundary condition wise).

The thesis covers to first steps towards a computational model that is capable of predicting the sounds created by stridor patients. A hybrid computational model is developed that uses LES with a selective subgrid scale model for the fluid part and the Lighthill analogy for the acoustic part.

Using the a reed instrument model and a diaphragm model it is shown that correct sound pressure levels can be obtained. For the reed instrument it is seen that coupling between flow and acoustics can not be captured using the current model. Other than the peaks the sound pressure level overlaps nicely. The peaks that are calculated can be explained. For the diaphragm good agreement with experimental results are obtained. However the lower frequencies seem to be over predicted

An upper airway model is used to validate the fluid part of the computational model. Very good agreement with PIV data is obtained. Also it is shown that the implemented LES model shows promising results. Also an acoustic analysis is performed on the upper airway. The sound production shows trends as expected. The upstream propagation of the sound is however hindered by the obstruction giving rise to low sound pressure levels at the inlet. The 50% constricted cases does show an increase sound pressure level near the inlet. The 75% constricted case as well, but not over the entire frequency range. At some parts similar levels as the healthy person are observed. For real patients the stridor in the 75% case should significantly be increased compared to the 50% case.

Also a realistic CT-scan derived model is presented. This model is altered to obtain a healthy person. The two models are analysed using the validated techniques. Comparison yields intuitive results for the fluid part. Also the acoustic source calculation shows results that are expected. Again the propagation is hindered by the obstruction. Near the outlet a significant increased sound pressure level is observed for the stridor patient while at the inlet sometimes even lower sound pressures levels are observed compared to the healthy person.

In a real patient extra constriction often means an increase of stridor sound near the inlet. This is not fully captured by the current computational model. For the SUAM it is

seen that initially the sound does increase but later on decreases again. However near the outlet a more consistent increase in signal is seen. Moreover from the CFD simulations it is seen that very large pressure drops are seen over the constrictions. This creates a force that can excite the tissue into vibration. Hence combining these results it is very well possible that for increasing constriction the sound production mechanism shifts from turbulent sound production to tissue vibration.

When looking at all results presented in the thesis it can be concluded that the Lighthill equation can be used for flow regimes encountered in upper airways. The flow results looked good and are accurate enough to perform an acoustic simulation. When looking at the spectra generated by the upper airway models the overall distribution could be possible, if compared to actual stridor sounds, however peaks are missing in the spectrum and the lower frequencies seem over predicted. Probably the peaks can only be captured by using flexible walls. Therefore it is needed to incorporate more physics into the computational model. A rigid wall approach is not sufficient to predict stridor sounds numerically.

## Chapter 7

# Future development and recommendations

The results presented in this thesis work show that there still is a long way to go to reach the final goal, being able to accurately predict the sound from a given geometry and using the results to determine the reversed relation. Although progress is made and the applicability of the Lighthill equation for upper airway acoustic analysis seems promising, improvement needs to be made before the numerical results can be considered accurate and reliable. Nonetheless, even with the current developed model more research can be done. In this chapter it is discussed what further steps can be taken to gain better understanding of the acoustics of the upper airways.

### 7.1 Further analysis using developed model

Using the model that is developed in the current thesis, still more research can be done. The effect of constricting is checked in this thesis but other changes are also of interest. For example the analysis of CT-scan derived healthy person would be interesting. This would give more confidence in the strength of the sources that are present in a healthy person for normal breathing. This would allow for better comparison between the results for the stridor patient. Further the rate of fluid flow can be altered. It would be very interesting to see how the acoustic results are influenced by the speed of breathing. It could be that only after a threshold of mass flow entering the model a significant difference is seen in the amount of produced noise. What is this threshold, if present at all? Also changing the phase of the breathing cycle would be an interesting simulation to see (inhaling versus exhaling). This is especially interesting when patient specific recorded data is available. For some cases it is known that stridor is observed for inspiration, but no sound is heard but for expiration and vice versa. Is this difference seen using only the noise generated from turbulent flow? Or is it necessary to add tissue vibration? One of these questions can also be determined experimentally. The mass flow can be changed by asking a patient to breathe faster or slower.

### 7.2 Patient data

One of the most important parts of further research is the possibility to compare the results with patient specific data. Because differences in upper airway geometry between patient is

expected especially for stridor patients, it is very favourable to have as much data as possible for this one patient (thus patient specific data). Only when for a single patient it is possible to accurately compute the acoustic behaviour, it can be tried to make generalizations. For example by putting the constriction of a stridorous patient in the airway of a healthy patient, using a computer program, and seeing if the acoustics are now different.

However to improve the accuracy of the computational model, and checking the results experimental data is needed. Hence it would be beneficial for university and medical institutions to open the discussion about what kind of data needs to be available for further research. This makes it possible to standardise certain procedures, such as to always document sound recordings of stridor patients and to obtain flow diagrams of the respiratory cycle. When this kind of data is readily available better conclusions can be drawn from numerical results and better insight could be gained into what parts of the computational model are not yet developed enough to get accurate results.

### 7.3 Model improvements

The improvements that can be made on the currently developed computational model will probably be incremental. Now that the first step is taken it will be relatively easy to incorporate small improvements. For example some of the assumptions (incompressibility, neglecting viscous stress tensor, isentropic relations) that are made in this thesis concerning the source term of the Lighthill equation can be removed to see whether the assumption are valid or not. Further there exist adaptations to the original model developed by Lighthill. These adaptations are often for the source term which should also allow for easy implementation. To change the source term one can simply build further upon the already existing code.

Perhaps more interesting are the effects of tissue vibration. For a highly constricted model the sound produced downstream of the constriction by turbulence seems to be blocked for a large part by the obstruction when travelling upstream. However vibration of the constriction will send sound waves in both upstream and downstream direction. Therefore for highly obstructed airways the vibrational modes might have a more significant contribution to the the perceived sound near the inlet than the turbulent sound generation.

To include this effect however would require adding a more significant amount of code to the existing computational model (compared to adaptations in the Lighthill equation). Different approaches are available to incorporate vibrations. The most difficult being a moving mesh approach, where the boundaries of the domain are allowed to move as a response to structural deformation. Implementing this would require extra efforts since the underlying equations need to be changed (from Eulerian formulation to arbitrary Lagrangian Eulerian formulation) to allow for mesh moving. Although part of this code is already implemented in newer versions of OpenFOAM, it would still require efforts to adapt the code properly. Also the the handling of multiple meshes should be incorporated that allow for a structure mesh and a fluid mesh (and the interpolation of variables on the contact surface). Further the structural models that describe the tissue behaviour need to be implemented manually.

An easier approach would be to use compatibility and equilibrium conditions on the structural-acoustic interfaces(following equations are from[33]). First the pressure in the flow must be in equilibrium with the structural stresses on the surface of the structure:

$$\boldsymbol{\sigma} \cdot \mathbf{n} = -pn. \quad (7.1)$$

And secondly it should hold that the velocity of the fluid should be equal to the normal velocity of the structural interface:

$$\mathbf{n} \cdot \frac{\partial \mathbf{u}}{\partial t} = \mathbf{n} \cdot \mathbf{v} \quad (7.2)$$

Taking the derivative with respect to time this yields the compatibility equation becomes

$$\mathbf{n} \cdot \frac{\partial^2 \mathbf{u}}{\partial t^2} = \mathbf{n} \cdot \frac{\partial \mathbf{v}}{\partial t} \quad (7.3)$$

Using the linearized momentum equation and equation 3.2 the following boundary condition is obtained

$$\mathbf{n} \cdot \frac{\partial^2 \mathbf{u}}{\partial t^2} = \mathbf{n} \cdot c^2 \frac{-\nabla \rho'}{\rho_0}. \quad (7.4)$$

Implementing these relations allows to take tissue vibration into account without the need for the fluid domain to alter in shape. Instead the vibration is imposed in the form of a boundary condition. This method is however (more) approximate and only valid for small vibrations. Hence problems such as Laryngomalacia can not be tackled using this approach. However the subglottic stenosis case might be a good candidate to test this method. The efforts that would be put in getting this method to work are however also a step toward more complicated modelling techniques used in full fluid structure interaction problems. Namely, for the vibro-acoustic method (the one explained here) the structural modelling needs to be implemented. This modelling can later also be used in an FSI calculation. The extra step of altering the fluid equations, and allowing moving meshes (which also needs remeshing schemes to keep the mesh smooth), is thereby postponed.



# Bibliography

- [1] Common causes of stridor. <http://www.wrongdiagnosis.com/symptoms/stridor/common.htm>.
- [2] Anonymous. Human voice. [http://en.wikipedia.org/wiki/Human\\_Voice](http://en.wikipedia.org/wiki/Human_Voice).
- [3] Anonymous. Sound pressure. [http://en.wikipedia.org/wiki/Sound\\_pressure](http://en.wikipedia.org/wiki/Sound_pressure).
- [4] C. Bailly, P. Lafon, and S. Candel. Computation of noise generation and propagation for free and confined turbulent flows. *AIAA and CEAS, Aeroacoustics Conference, 2nd, State College, PA, May 6-8, 1996*.
- [5] J. Baun. *Physical Principles of General and Vascular Sonography*. 2009.
- [6] P.S. Bellet. Principal causes of airway obstruction. [http://www.wrongdiagnosis.com/a/airway\\_obstruction/book-diseases-15b.htm](http://www.wrongdiagnosis.com/a/airway_obstruction/book-diseases-15b.htm).
- [7] B.J. Boersma. Numerical simulation of the noise generated by a low mach number, low reynolds number jet. *Fluid Dynamics Research*, 35:425–447, 2004.
- [8] M. Breuer, B. Kniazev, and M. Abel. Development of wall models for les of separated flows using statistical evaluations. *Computers & Fluids*, 36:817–837, 2007.
- [9] M. Brouns, S. Verbanck, J. van Beek, S Vanlanduit, J. Vanherzeele, and C. Lacor. Piv on the flow of a simplified upper airway model. *13th Int Symp on Applications of Laser Techniques to Fluid Mechanics*, (1120), 2006.
- [10] R.K. Calay, J Kurujareon, and A.E. Holdo. Numerical simulation of respiratory flow patterns within humman lungs. *Respiratory Physiology & Neurobiology*, 130:201–221, 2001.
- [11] X.X. Chen, X. Zhang, C.L. Morfey, and P.A. Nelson. A numerical method for computation of sound radiation from an unflanged duct. *Journal of Sound and Vibration*, 270:573–586, 2004.
- [12] J. Claes, A. Boudewyns, P. Deron, V. Van der Poorten, and H. Hoeve. Management of stridor in neonates and infants. *B-ENT*, 1:113–122, 2005.
- [13] M. Escobar. Finite element simulation of flow-induced noise using lighthill’s acoustic analogy. Technical report, Technischen Fakultät der Universität Erlangen-Nürnberg, 2007.

- [14] M. Farhadi and M. Rahnema. Large eddy simulation of separated flow over a wall-mounted cube. *Scienti9a Iranica*, 13(2):124–133, 2006.
- [15] X. Gloerfelt and P. Lafon. Direct computation of the noise induced by a turbulent flow through a diaphragm in a duct at low mach number. *Computers & Fluids*, 37:388–401, 2007.
- [16] L. Gray, J.C. Denny, H. Carvajal, and R. Jahrsdoerfer. Fourier analysis of infantile stridor: preliminary data. *International Journal of Pediatric Otorhinolaryngology*, 10:191–199, 1985.
- [17] J. Hirschberg. Acoustic analysis of pathological cries, stridor and coughing sounds in infancy. *International Journal of Pediatric Otorhinolaryngology*, 2:287–300, 1980.
- [18] YC Hu, PL Liao, WP Shih, XY Wang, and Chang PZ. Study on the acoustic impedance matching of human tissue for power transmitting/charging system of implanted biochip. *IEEE 3rd International conference on nano/molecular medicine and engineering*, 2009.
- [19] Y. Huang, A. Malhotra, and D.P. White. Computational simulation of human upper airway collapse using a pressure-/state-dependent model of genioglossal muscle contraction under laminar flow conditions. *J Appl Physiol*, 99:1138–1148, 2005.
- [20] S. T. Jayaraju, M. Brouns, C. Lacor, B. Belkassen, and S. Verbanck. Large eddy and detached eddy simulations of fluid flow and particle deposition in a human mouth-throat. *JOURNAL OF AEROSOL SCIENCE*, 39(10):862–875, 2007.
- [21] X. Jinxiang, Si. Xiuhua, K. Jong Won, and B. Ariel. Simulation of airflow and aerosol deposition in the nasal cavity of a 5-year-old child. *Journal of Aerosol Science*, 42:156–173, 2011.
- [22] K. Keyhani, PW. Scherer, and MM. Mozell. Numerical simulation of airflow in the human nasal cavity. *Biomech Eng*, 117:429–41, 1995.
- [23] A. Leiberman, A. Cohen, and A. Tal. Digital signal processing of stridor and snoring in children. *International Journal of Pediatric Otorhinolaryngology*, 12:173–185, 1986.
- [24] M.J. Lighthill. On sound generated aerodynamically. i. general theory. *Proceedings of the Royal Society of London*, 211(1107):564–587, 1952.
- [25] G.D. Ludwig. The velocity of sound through tissues and the acoustic impedance of tissues. *The journal of the acoustical society of America*, 2(6), 1950.
- [26] C.T. Lynch. The numerical acoustic and fluid flow analysis on a ct-scan derived upper airway model of a stridor patient, a literature study. Technical report, Aerodynamics, Faculty of Aerospace engineering, Delft University of Technology, 2011.
- [27] A. Malhotra, Y. Huang, R.B. Fogel, G. Pillar, J.K. Edwards, R. Kikinis, S.H. Loring, and D.P. White. The male predisposition to pharyngeal collapse: Importance of airway length. *Am J Respir Crit Care Med*, 166:1388–1395, 2002.
- [28] I. Mary and P. Sagaut. Large eddy simulation of flow around an airfoil near stall. *AIAA JOURNAL*, 40(6), 2002.

- [29] P Milenkovic. Vocal tract area functions from two-point acoustic measurements with formant frequency constraints. *IEEE, ASSP-32*(6), 1984.
- [30] M. Miyamoto, Y. Ito, K. Takahashi, T. Takami, T. Kobayashi, A. Nishida, and M. Aoyagi. Numerical study on vibration of an air-reed instrument with compressible les. *physics.flu-dyn*, 2010.
- [31] DE. Olsen, MF. Sudlow, K. Horsfield, and GP. Filey. Convective patterns of flow during inspiration. *Arch Int Med*, 131:51–57, 1973.
- [32] M. Piellard and C. Bailly. Several computational aeroacoustics solutions for the ducted diaphragm at low mach number. *AIAA/CEAS Aeroacoustics Conference*, AIAA 2010-3996, 2010.
- [33] D.J. Rixen. Coupled analysis of structures and acoustics. Technical report, Delft University of Technology, Faculty of Design, Engineering and Production, 2010.
- [34] G.J.J. Ruijgrok. *Elements of aviation acoustics*. VSSD, Leeghwaterstraat 42, 2628 CA Delft, The Netherlands, 2007.
- [35] P. Sagaut, E. Montreuil, and O. Labbé. Assessment of some self-adaptive sgs models for wall bounded flows. *Aerospace Science and Technology*, 6:335–344, 1999.
- [36] E.B. Slawinski and D.G. Jamieson. Studies of respiratory stridor in young children: acoustical analyses and tests of a theoretical model. *International Journal of Pediatric Otorhinolaryngology*, 19:205–222, 1990.
- [37] J. Soo-Jin, K. Woo-Seung, and SJJ. Sang-Jin. Numerical investigation on the flow characteristics and aerodynamic force of the upper airway of patient with obstructive sleep apnea using computational fluid dynamics. *Sciencedirect*, 2006.
- [38] Children’s Specialists. Laryngomalacia. <http://www.cssd.us/body.cfm?id=464>.
- [39] L. Temmerman, M.A. Leschziner, C.P. Mellen, and J. Fröhlich. Development of wall models for les of separated flows using statistical evaluations. *Computers & Fluids*, 24:157–180, 2003.
- [40] Z. Teng, I. Ochoa, Z. Li, Y. Lin, J.F. Rodriguez, J.A. Bea, and M. Doblare. Nonlinear mechanical property of tracheal cartilage: A theoretical and experimental study. *Journal of Biomechanics*, 41:1995–2002, 2008.
- [41] J. Xi and P.W. Longest. Numerical predictions of submicrometer aerosol deposition in the nasal cavity using a novel drift flux approach. *International Journal of Heat and Mass Transfer*, 51:5562–5577, 2008.
- [42] C. Xu, M.J. Brennick, L. Dougherty, and D.M. Wootton. Modeling upper airway collapse by a finite element model with regional tissue properties. *Medical Engineering & Physics*, 31:1343–1348, 2009.
- [43] R. Zoumalan, J. Maddalozzo, and L.D. Holinger. Etiology of stridor in infants. *Ann Otol Rhinol Laryngol.*, 116:329–334, 2007.

- 
- [44] J.W. Zwartenkot. Fast fourier spectral analysis of inspiratory stridor in children. Technical report, Department of Otorhinolaryngology Erasmus Medical Centre - Sophia Childrens Hospital.
- [45] J.W. Zwartenkot, H.L.J. Hoeve, and J. Borgstein. Inter-observer reliability of localization of recorded stridor sounds in children. *International Journal of Pediatric Otorhinolaryngology*, 74:1184–1188, 2010.

# Appendix A

## Model geometries

### A.1 Reed

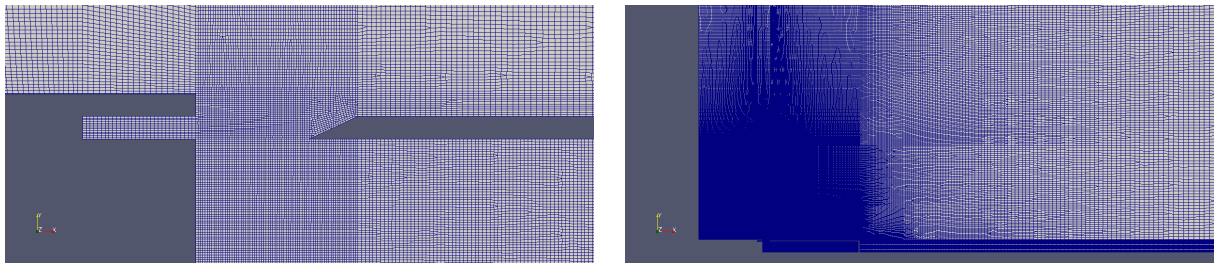


**Figure A.1:** Reed mesh, zoomed (left) and global (right)

## A.2 Diaphragm

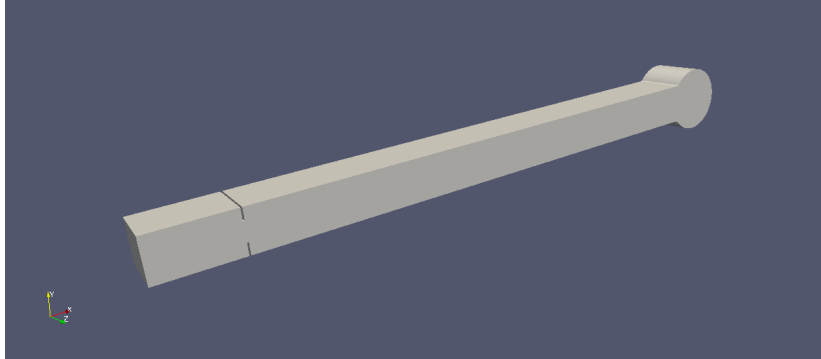


**Figure A.2:** Diaphragm computational model

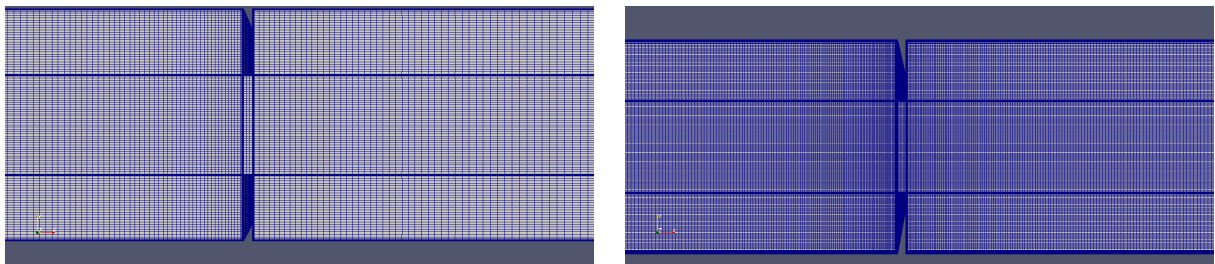


**Figure A.3:** Mesh diaphragm, course(left) and fine (right)

## A.3 SUAM

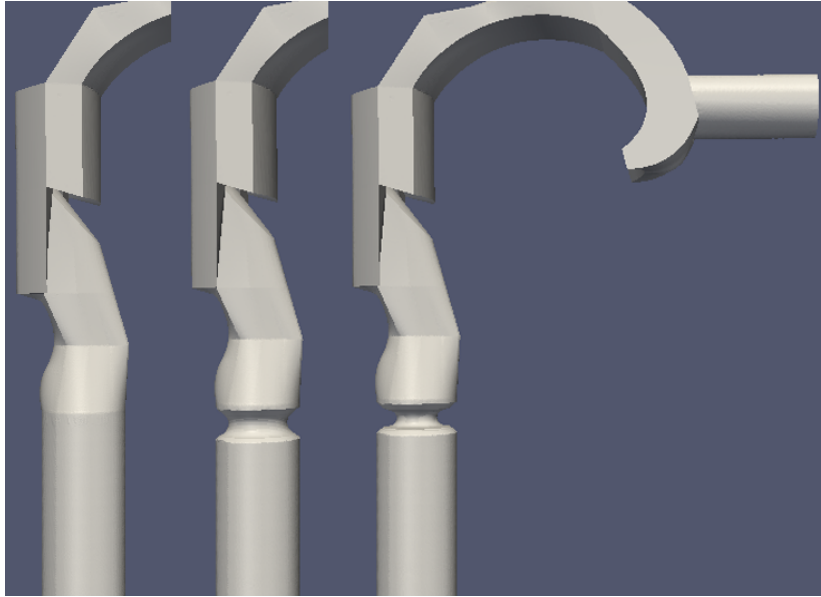


Figure A.4: SUAM constrictions, from left to right: 0%, 50% and 75% of tracheal area

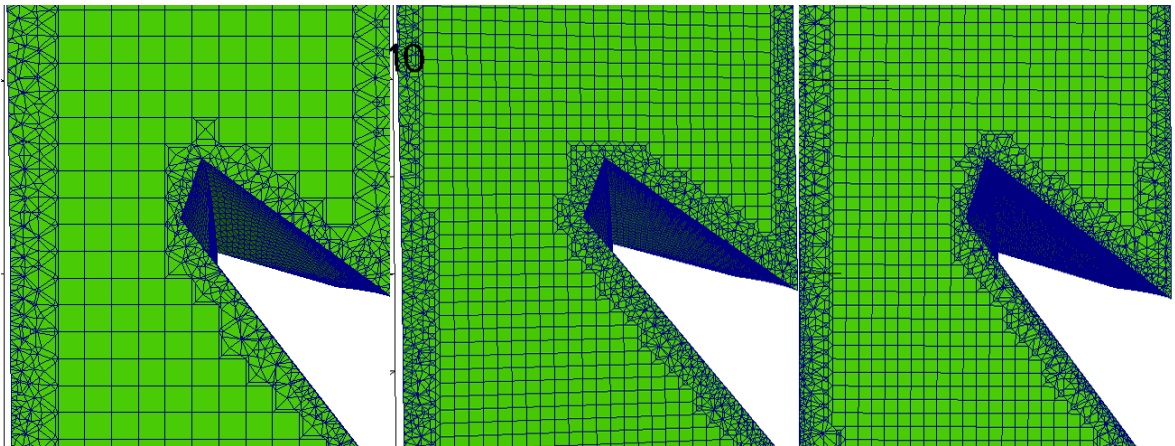


Figure A.5: Mesh SUAM, course(left) fine(middle) and extra-fine(right)

A.4 RUAM

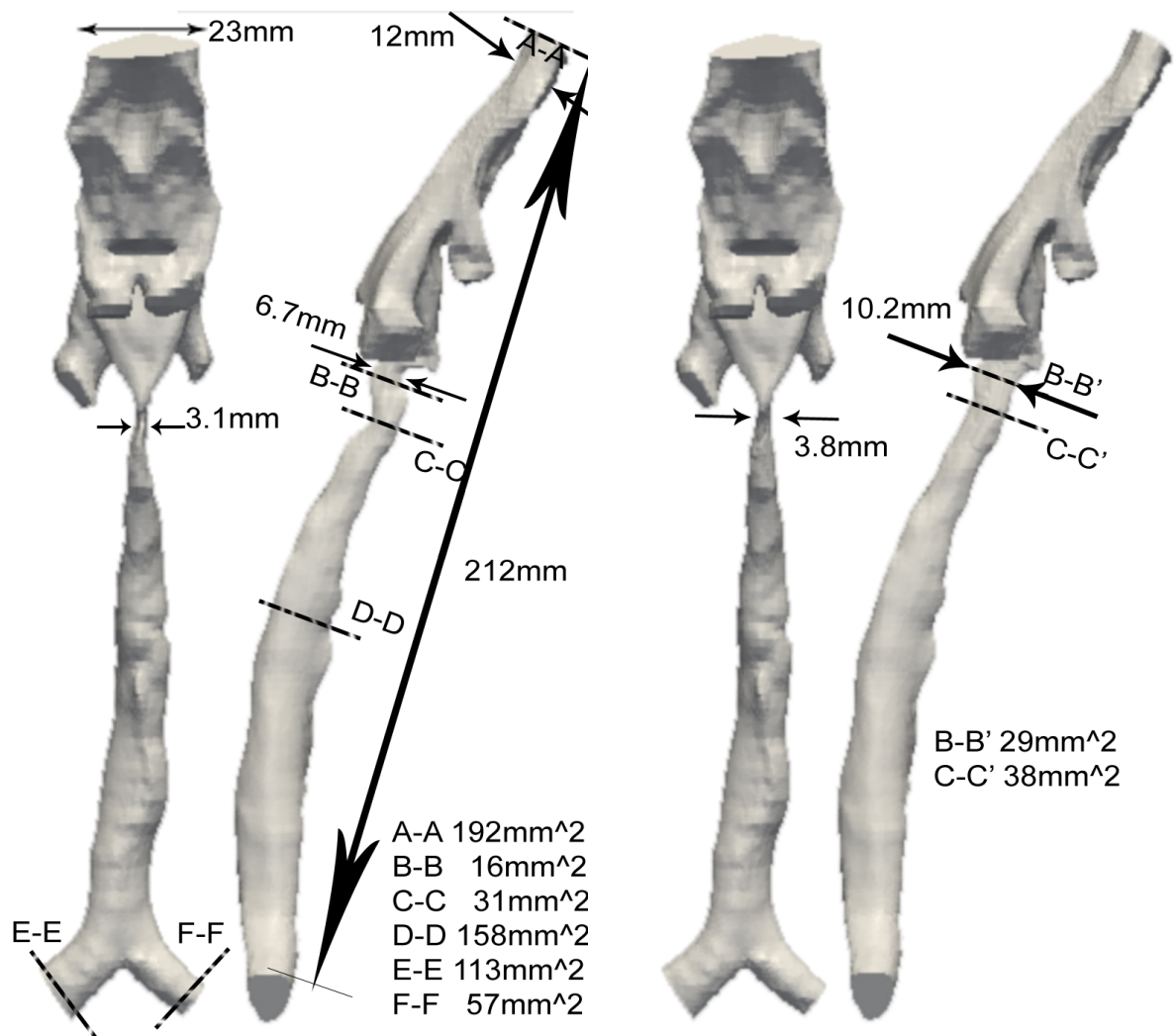
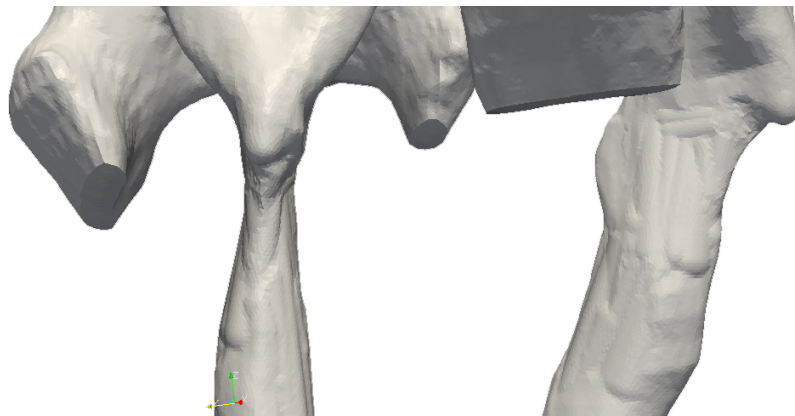


Figure A.6: Mesh RUAM, original(left)and edited(right)



**Figure A.7:** RUAM original, zoom on stenosis



**Figure A.8:** RUAM edited, zoom on resolved stenosis

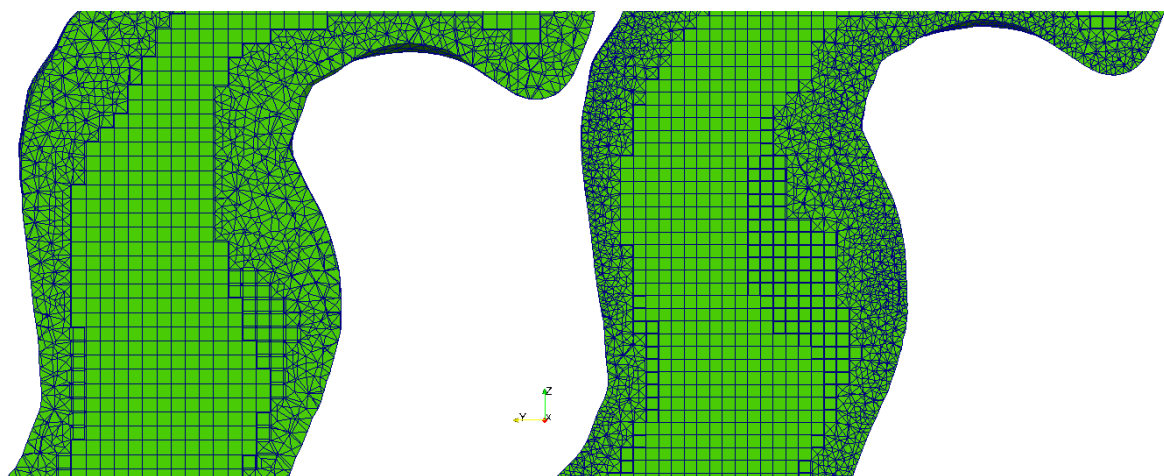


**Figure A.9:** Mesh RUAM, coarse(left) and fine(right)

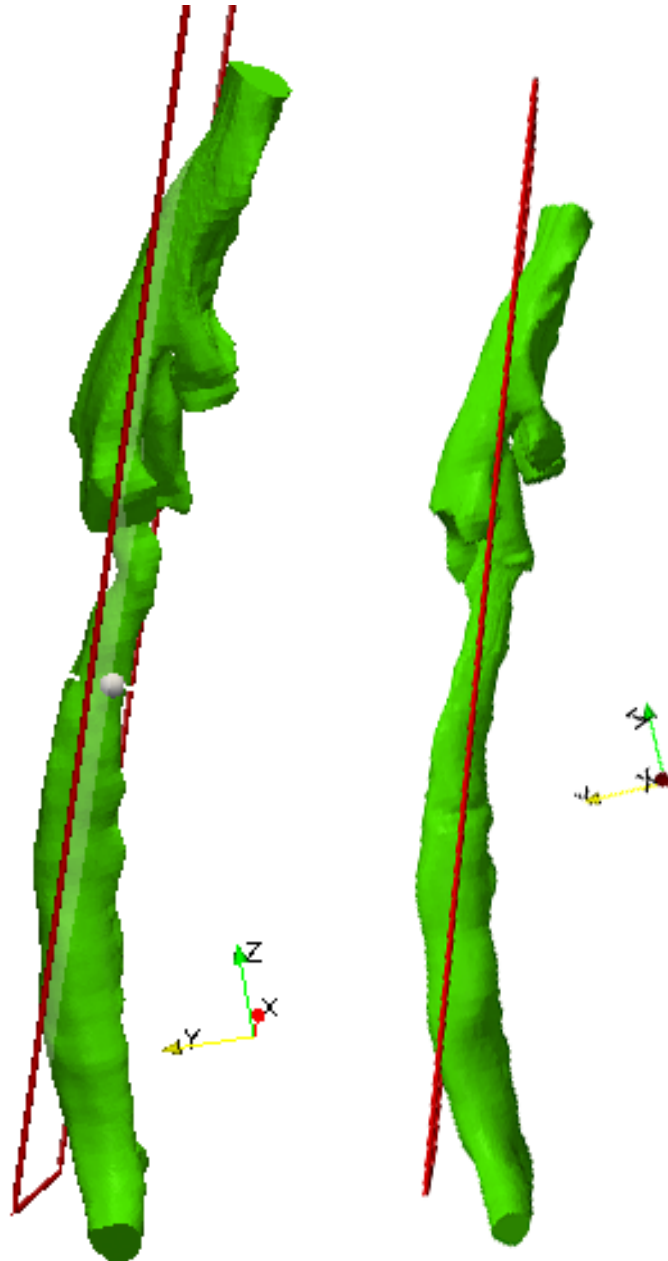


Figure A.10: Cutplane used for front view, original(left) and edited(right)